Dissertation

GEM – A Novel Gaseous Particle Detector

ausgeführt zum Zwecke der Erlangung des akademischen Grades eines Doktors der technischen Naturwissenschaften, unter der Leitung von

Univ. Doz. Univ. Prof. Dr. Dipl-Ing. Christian W. Fabjan
Atominstitut (E141)

eingereicht an der Fakultät für Technische Physik
der Technischen Universtiät Wien

von

Dipl. Ing. Meinschad Thomas
Matrikelnummer: 9625695
Konrad Meindl Strasse 2; 4600 Wels; Oberösterreich

Diese Arbeit wurde unterstützt vom Österreichischen Bundesministerium für Bildung, Wissenschaft und Kultur.

Genf, am 23.05.05

Begutachter

Technische Universität Wien, Atominstitut (E 141)

Univ. Doz. Univ. Prof. Dr. Dipl.-Ing Christian W. Fabjan

Technische Universität Wien, Institut für Festkörperphysik (E 138)

Ao. Univ. Prof. Dipl.-Ing. Dr.techn. Michael Mantler

Zusammenfassung

Die vorliegende Arbeit beschäftigt sich mit der Konstruktion von Gasdetektor-Prototypen, die sogenannte GEM-Elektroden (Gas Elektron Vervielfacher) verwenden, um die von ionisierenden Teilchen im Gas produzierte Ladung zu verstärken und detektierbar zu machen. Eine GEM-Elektrode besteht aus einer zweifach mit Kupfer beschichteten Kaptonfolie, in die kleine Löcher (typischerweise 50-100mm^{-2} mit einem Durchmesser von 50μm) geätzt werden. Diese Löcher wirken bei Anlegen einer Potentialdifferenz (~400V) als voneinander unabhängige Proportionalzähler. Mit Hilfe dieses neuen Verstärkers können Gasverstärkungsfaktoren in der Größenordnung von 10^6 erreicht werden, wenn man mehrere GEM-Folien in einer Kaskade zusammenfasst.

Im speziellen wird in dieser Arbeit erforscht, ob die GEM-Technologie auf RICH (Ring Imaging Cherenkov) Detektoren angewandt werden kann. In derartigen Teilchendetektoren werden Photokathoden verwendet, um die von geladenen hochenergetischen Teilchen erzeugten Cherenkov Lichtringe abzubilden. Damit können die Teilchen identifiziert und unterschieden werden.

Um die einzelnen UV-Photonen effizient nachweisen zu können gibt es mehrere Möglichkeiten. Die kostenintensivste ist die, Photonen mit einer Matrix aus einzelnen Photokathoden (PMTs oder HPDs) zu messen. Photosensitive Gase (TAE, TMAE) mit hoher Quanteneffizienz sind billiger aber umständlich in der Verwendung. Derartige Gase beschränken außerdem aufgrund der geringeren Driftgeschwindigkeit die Hochratenkapazität der dementsprechenden Photodetektoren.

Aufgrunddessen wurde ein photosensitives Material entwickelt, das es erlaubt, großflächige Photokathoden zu bauen – Cäsiumiodid (CsI). Bedampft man die segmentierte Kathode einer Vieldrahtkammer mit CsI, dann hat man eine großflächige Photokathode zur Verfügung mit der Cherenkov Photonen nachgewiesen und eindeutig unterscheiden werden können (multi-hit capability).

In den hier entwickelten Detektor-Prototypen wird CsI als Photonkonverter verwendet. Eine mit Gold überzogene GEM-Folie wird mit einer 300nm dicken CsI-Schicht bedampft. Dieser CsI-GEM ist das erste ladungsverstärkende Element in einer GEM-Kaskade von drei oder vier GEMs. Auf diese Weise wird eine effiziente und schnelle Photon-Detektierung mit einer ausgezeichneten Ortsauflösung erreicht. Wird der GEM-Gasdetektor an ein neuartiges Ausleseboard, das unter dem Name HEXABOARD bekannt ist, gekoppelt, dann ist eine eindeutige Rekonstruktion von Viel-Photonentreffer möglich - eine notwendige Eigenschaft eines Detektors für RICH-Anwendungen. Dieses Ausleseboard besteht aus einer Matrix aus hexagonalen Feldern, die abwechselnd mit den Auslesekanälen dreier Projektionen verbunden sind. Durch die Hinzunahme der dritten Projektion wird die eindeutige Rekonstruktion der Photonentreffer ermöglicht.

Jeder dieser Auslesekanäle ist an einen ladungssensitven Vorverstärker (HARP-Typ) gekoppelt. Die einzelnen aufgenommenen analogen Signale werden dann von der ALTRO-Elektronik digitalisiert (10bit ADC, 25MHz sampling rate) und weiterverarbeitet. Die ALTRO-Elektronik basiert auf dem ALTRO-chip, der für das ALICE-Experiment entwickelt worden ist.

Mit Hilfe von Lochmasken werden Vielphotonenevents simuliert. Diese Studien werden in dieser Arbeit präsentiert.

Die hier präsentierte ausgezeichnete Einzel-Photon Ortsauflösung und die Viel-Photon Auflösung zusammen mit der starken Unterdrückung des Photon- und Ionen-Feedbacks machen die GEM-Technologie interessant für RICH-Anwendungen.

Abstract

The work carried out within the framework of this PHD deals with the construction of gaseous prototype detectors using Gas Electron Multiplier electrodes for the amplification of charges released by ionizing particles.

The Gas Electron Multiplier (GEM) is a thin metal-clad polymer foil, etched with a high density of narrow holes, typically 50-100mm^{-2}*. On the application of a potential difference between the conductive top and bottom sides each hole acts as independent proportional counter. This new fast device permits to reach large amplification factors at high rates with a strong photon and ion-mediated feedback suppression due to the avalanche confinement in the GEM-holes.*

Here, in particular studies have been performed, which should prove, that the GEM-technology is applicable for an efficient measurement of single Cherenkov photons. These UV-photons can be detected in different ways. An elegant solution to develop large area RICH-detectors is to evaporate a pad-segmented readout-cathode of a multi-wire proportional chamber with a thin layer of CsI (typically 300nm). This approach has advantages compared to other possibilities of detecting Cherenkov photons (e.g.: photosensitive gases, arrays of PMTs or HPDs).

The subject of this thesis was the investigation of GEM-detectors with respect to RICH applications. This work contains the construction process of photon detectors based on the novel GEM-technology by using CsI as a photon converter. These detectors permit to efficiently record and localize single photoelectrons.

The first Au-plated GEM, in a cascade of three or four, is coated with a photosensitive layer, to provide efficient and fast single photon detection, with excellent position resolution. General performances of a CsI-coated multi-GEM detector are described as well as the novel readout method, which is achieved by the so called HEXABOARD. This board consists of a matrix of interconnected hexagonal pads that permit an ambiguity-free reconstruction of multi-photon events, which is an essential requirement for RICH applications.

Each single channel is connected to charge sensitive preamplifier (HARP-type) and afterwards to the ALTRO FEE, which is based on the ALTRO chip developed for the ALICE experiment. The recorded analog signals are digitized by 10 bit ADC with a 25MHz sampling rate.

This thesis is structured in the following way: Chapter 1 provides an introduction to experiments at the LHC with the focus on gaseous detectors, which are going to be used and summarizes different novel gaseous detector technologies. Chapter 2 outlines the physics of gaseous detectors. In chapter 3 the GEM-technology and their functionality are summarized. Chapter 4 presents the results of a first prototype GEM photon detector coupled to a single strip readout board to measure the spatial resolution of single photons. Chapter 5 presents the performance studies of the photon detector equipped with the HEXABOARD, followed by the summary and the conclusions (Chapter 6).

Acknowledgements

Regarding to my work here at CERN I am indebted to Christian W. Fabjan, who provided me the opportunity to come to this research center by supporting my application. Here at CERN, he finally supervised my PHD thesis for the Vienna University of Technology. Furthermore he initialized the contacts to the ALICE electronics group under the leadership of L. Musa, whom I want to acknowledge for the procurement of the readout electronics mainly used in my measurements.
At this point I want thank Fabio Sauli for accepting me in his Gas Detector Group. The interesting work in his group (Leszek and me!) and the various discussions enriched me a lot and increased my knowledge in fields of gaseous detectors. Special thanks I want to say to Leszek Ropelewski, who taught me how to work with gaseous detectors and how to make them operational and all the soft skill concerning detectors, which are not published in any papers.

I am also especially grateful to our technician Miranda van Stenis who supported me, when my "technical" skills came to an end. Without her most of my commissioned detectors would not produce reasonable results. Thanks also to Claude David, who took care of the CsI evaporation on my GEMs, which I used in my studies.

Finally here seems to be the place to express my gratitude in more private manners. First of all I would like to thank my parents, my younger siblings and my girlfriend who supported my decision to study physics and finally to make my PHD abroad.

I would also like to thank the large Austrian community at CERN for the warm welcome and nice company in the sad hours of "physical" doubts, whether I have done the right thing in preferring Geneva, the centre of finance and excellence to Vienna, the center of amusement and humor.

Last but not least I would also like to say thank you to some boys, which I met here, who joined me sometimes in my midday-running sessions on the red or blue course devouring kilometers. Sometimes, when my physical adequacy was accepted they allowed me to join them in their stupid hunts for more perilous steep slopes in the French and Austrian Alpes. Such a devoted craziness I have never seen before. In order to honor them in the right way I will mention their names and finally enjoy the pondering silence of friendship: H. Hudi Hödlmoser, T. Hansi Steiner, B. "Auchi" Auchmann and P. Udo Urschütz.

Contents

Chapter 1

The Necessity for New Gaseous Detector Devices

1.1 Introduction

The basic composition of matter has been understood progressively during the last decades. The theory of the fundamental particles and their interactions, the Standard Model, answers several of the questions of the structure of matter with its six types of quarks, six leptons and four forces – electromagnetism, the weak and the strong force. Gravity, the weakest of the four, is not described within the Standard Model.

There are three types of particles described in the Standard Model: spin-½ fermions (matter particles), spin-1 gauge bosons (which mediate interactions between matter particles), and a spin-0 Higgs boson (which is a consequence of spontaneous symmetry breaking) [1]. The Higgs mechanism is mediated by this heavy scalar particle. This theoretical concept represents a possibility for introducing the particle masses into the Standard Model. Although the Standard Model of elementary particle physics is well established, e.g.: by the experiments at the LEP (Large Electron-Positron collider), it is still incomplete because of this unknown mass-generation mechanism.

Also other extensions of the Standard Model, such as Super-Symmetry (SUSY), require the existence of other scalar and fermionic particles. These phenomena will be studied at the Large Hadron Collider.

1.2 The Large Hadron Collider

In 2007 it is foreseen that the Large Hadron Collider (LHC) will be operational as a new instrument in experimental particle physics. Hosted in the existing 27km long circular LEP tunnel it will accumulate and collide two proton beams with a centre-of-mass energy $\sqrt{s}$ of 14TeV. The machine will provide bunched p-p collisions in four main intersection points (*Fig. 1.1*). At a design luminosity of 10^{34}cm^{-2} s^{-1} beam crossing points will provide experiments with collision rates at the 10^9Hz level, producing more than 10^{11} particles per second. Due to the substantial rate of p-p collisions the level of the background is so high that it becomes a major design criterion for the detectors.

The bunch spacing will be 25ns. At the interaction points the transverse bunch radius will be 15μm and the bunch length will be 30cm. This means that the position of the vertex will have a rather large spread along the beam direction; the effective distribution of the vertex position is expected to be 5.5cm (r.m.s) along the beam direction.

The LHC will be filled with protons delivered from the SPS (Super Proton Synchrotron) and its pre-accelerators at 450GeV *(Fig. 1.1)*.

The accelerator will also provide heavy ions collisions (lead on lead) with a centre-of-mass energy of 1000TeV.

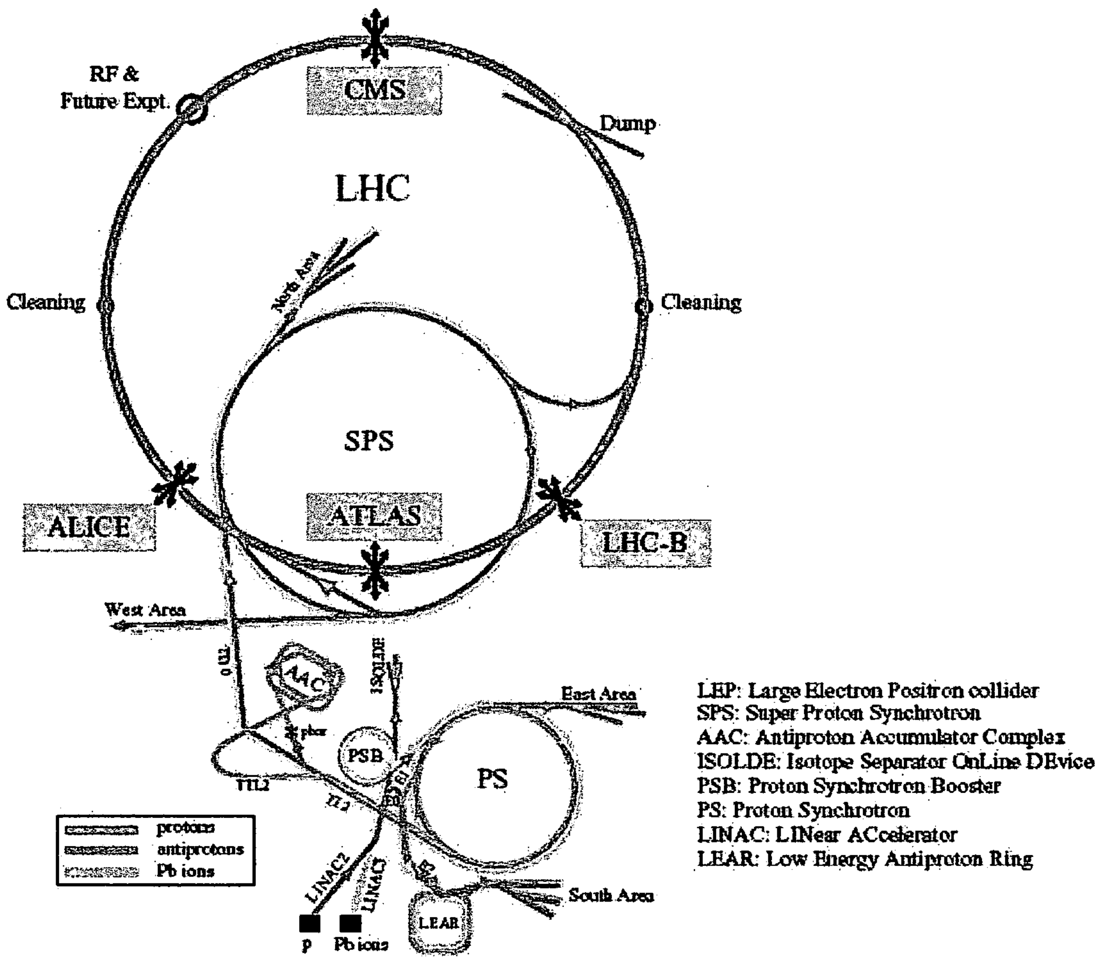

Fig. 1.1: Schematic view of the whole CERN accelerator complex.

In order to deliver the maximum centre-of-mass energy within the confines of the LEP tunnel the machine employs a two-in-one magnet structure. Two superconducting magnet channels will accelerate protons to 7-on-7TeV, after which the beams will counter-rotate for several hours, colliding at the experiments until the beam degradation is such that the machine has to be emptied and refilled. Hundreds of dipole magnets with a magnetic field of 8.4T must operate in superfluid helium at temperatures below 2K.

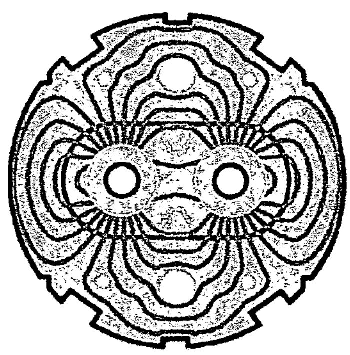

Fig. 1.2: Illustration of the cross section of the magnetic channels for LHC.

The magnetic channels of the two proton beams are housed in the same yoke and cryostat. *Fig. 1.2* shows an illustration of the cross section of the magnet for these two channels.

1.2.1 Physics at the LHC and Detector Requirements

One of the main motivations for the LHC is to clarify the nature of electroweak symmetry breaking for which the Higgs mechanism is presumed to be responsible. Considerable attention has been paid during the design process to the sensitivities of the Higgs signatures. The LHC is designed to explore all the range of possible Higgs masses and more, hence the planned experiments either must find the Higgs boson or contradict the Standard Model. The LHC is well suited for a search of the Standard Model Higgs boson or a family of Higgs bosons when considering the Minimal Supersymmetric extension of the Standard Model (MSSM).

At the LHC heavy fermions (top and bottom quarks) will be produced in large quantities. Beside the Higgs search also B physics as well as the study of top-quark production and decay will be interesting issues for the LHC physics program. All these examples are used as benchmark processes for the detector design. In this section these benchmark processes will be discussed. *Fig. 1.3* shows several important cross sections and interaction rates as a function of the centre-of-mass energy $\sqrt{s}$.

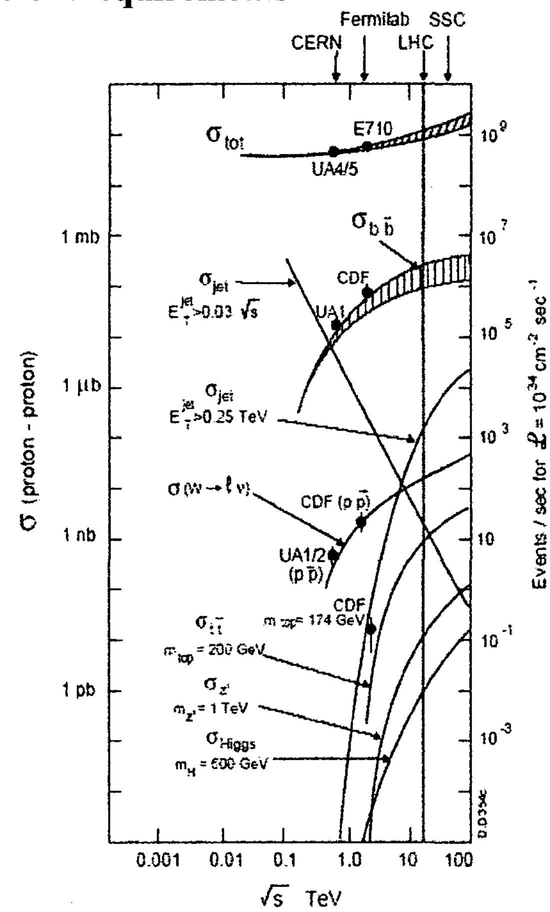

Fig. 1.3: The cross section of some characteristic processes at LHC [2][3].

The total proton-proton cross section is estimated to be between 90 and 130 mb. Therefore on average there will be 20 interactions in the center of the detectors per bunch crossing at full luminosity. Small-angle elastic and inelastic scattering will be the most numerous and therefore dominate the 20 underlying events per bunch crossing. Only a limited number of decay channels of the Higgs boson production are accessible to the experimental observation, because either the decay channels have small branching ratios, or the decays are obscured by a large background of events that carry the signature of the Higgs boson. *Fig. 1.4* illustrates the relevant Higgs production mechanisms. All of them make use of the Higgs' preference to couple to heavy particles [3]. The current lower limit on the mass of the Higgs boson, from LEP experiments, is 114.2 GeV/c^2 [4].

- Below the WW and ZZ threshold ($m_{Higgs}<2m_Z$) the largest Higgs decay branching ration will be $H \rightarrow b\bar{b}$. Since this decay channel is overwhelmed by QCD background, the reconstruction and tagging of b-jets with high efficiency is a crucial element in the detector performance. The most prominent detection channel is WH→γγ. This signature suffers from very large backgrounds from the irreducible prompt γγ continuum and the jet-jet and γ-jet production. The first channel places severe demands on the performance of the electromagnetic calorimeter and powerful particle identification capability will be needed to reject a large jet background.

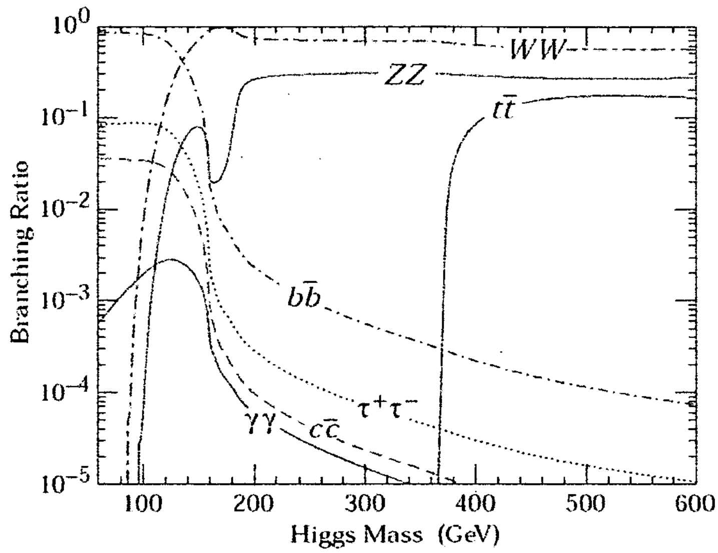

Fig. 1.4: Branching ratios of the Higgs particle [5].

- In the mass region between 120 GeV/c^2<m$_{Higgs}$<180 GeV/c^2 the decay H→ZZ$^{(*)}$→4l$^{\pm}$ provides a very clean signature for the Higgs boson. For a Higgs mass of a 150 GeV/c^2 one expects 550 events per year. The background processes are ZZ$^{(*)}$,Zγ$^{(*)}$→4l continuum, $t\bar{t}$→4l and $Zb\bar{b}$→4l. The geometrical and kinematical acceptance for leptons is important in this decay channel and the significance will depend on the 4 lepton mass resolution. Hence good energy/momentum resolution is required.

- In the mass range of 180 GeV/c^2<m$_{Higgs}$<800 GeV/c^2 the H→ZZ→4l decay mode is considered to be the most reliable discovery channel since the expected signal rates are large and the background small.

- For heavy Higgs boson masses (m$_{Higgs}$>800 GeV) the Higgs width increases rapidly and the signal will be rate limited. In this mass range, the H→ZZ→l$^+$l$^-$νν channel is six times more frequent than the H→4l channel. It can be detected with the measurements of two high-p$_T$ and a high missing E$_T$ due to missing neutrinos.

The Higgs search is the most popular benchmark process for the detector design, but there are many other examples. For the MSSM Higgs bosons H$^{\pm}$ and A, efficient vertex detection for τ leptons and b-quarks as well as high resolution calorimetry for jets and missing transverse energy are essential. Also the search for stable supersymmetric particles sets stringent requirements for the hermeticity and missing E_T capability of the detectors. New heavy gauge bosons W' and Z' could be accessible for masses up to 5-6 TeV/c^2. Therefore high resolution lepton measurement and charge identification are needed even in a p_T range up to a few TeV/c.

An important chapter of the LHC will be the study of heavy quark systems since also at lower intensity the LHC will be a high rate beauty and top factory. Another interesting field will be the precise measurement of the CP-violation.

1.2.2 Experiments at the LHC

In order to exploit the full discovery potential of LHC, two general-purpose proton-proton experiments (ATLAS and CMS) and three specialized experiments (ALICE, LHCb and TOTEM - partially housed inside CMS) will be installed at four interaction points. Both general-purpose experiments will search for the Higgs particle, which has not yet been convincingly observed. Moreover, they study unsolved aspects of the standard model. As mentioned above the LHC will also produce lead-lead collisions which will be investigated by ALICE. LHCb performs studies on CP violation and beauty physics in general and TOTEM will study physics in the very forward direction.

The experimental set-ups will be only described briefly. Detailed descriptions of the experimental set-ups of these detectors and their design considerations can be found in the respective detector technical proposals [6][7] [8][9].

ATLAS, ALICE and CMS are in construction in their respective surface assembly halls, and will be gradually transferred and re-assembled in the underground caverns. They have an onion-like structure determining the event topology, the nature and the energy of the emerging particles. In these experiments the momentum of charged particle tracks is inferred from the curvature in strong magnetic fields. The particle identification is performed in a succession of electromagnetic and hadronic calorimeters followed by muon detectors. The main difference between ATLAS and CMS lies in their magnet configurations for muon spectroscopy.

- **ATLAS**

  The ATLAS (A Toroidal LHC ApparatuS) detector can be characterized by two different magnetic field systems, an inner superconducting solenoid around the inner detector cavity with a 2 T field (2.4 m diameter and 5.3 m length) and an outer superconducting toroid magnet system. 8 coils at radial distances from the axis between 4.7 m and 9.7 m plus two end-cap toroids are arranged outside the calorimetry. This toroid together with a large number of large-area tracking detectors forms a magnetic spectrometer for muons for the decay channel $H \rightarrow ZZ^* \rightarrow 4\mu$. The momentum resolution $\Delta p_T/p_T$ is expected to be 10^{-2} at a transversal momentum p_T of 100 GeV/c. The muon spectrometer consists of several different types of chambers used for tracking and triggering. Muon Drift Chambers (MDT) are used for the bulk of tracking, complemented by Cathode Strip Chambers (CSC) in the end-cap regions, where high rates can be found. Precisions of the order of 50 μm demanded. The CSCs of ATLAS are multi-wire proportional chambers *(see Chapter 1.3.1)* with cathode strip readout with a symmetric cell in which the anode-cathode spacing is equal to the anode wire pitch. The transversal coordinate is obtained from strips parallel to the anode wires, which form the second cathode of the chamber.

The triggering function is also quite important to reduce the data flow in the experiment. Resistive Plate Chambers (RPC) in the barrel and Thin Gap Chambers (TGC) in the end-cap have a response fast enough to fulfill the triggering task. RPCs are gaseous parallel plate chambers with a typical space-time resolution of 1 cm x 1 ns. Each chamber is made of two rectangular detector layers each one read out by two orthogonal series of pick-up strips. The TGCs have a structure similar to the multi-wire proportional chambers, but are faster and can reach higher gains.

The ATLAS inner detector consists of high resolution CCD pixels (1.4 m^2) and silicon strip counters – (SCT – Semi Conductor Tracker) (41 m^2) with resolutions in r and φ of 10 to 20 μm complemented by TRD track detectors. The transition radiation detectors consist of proportional drift tubes with a diameter of 4 mm operated in a $Xe/CF_4/CO_2$ gas mixture. It is optimized for the detection of X-rays created as transition radiation in stacks of thin radiators between the tubes. The single wire resolution will be 170 μm.

Electromagnetic calorimetry is performed in a lead-LAr detector with accordion shaped Kapton electrodes and lead absorber plates aiming for an energy resolution $\Delta E/E=10\%/\sqrt{E}\oplus 1\%$ [GeV], while the hadronic calorimetry is done in a tile calorimeter with plastic scintillator plates embedded in iron absorbers and read out by wavelength-shifting fibers. The end cap hadronic calorimeters are out of copper plates immersed in LAr ionization chambers.

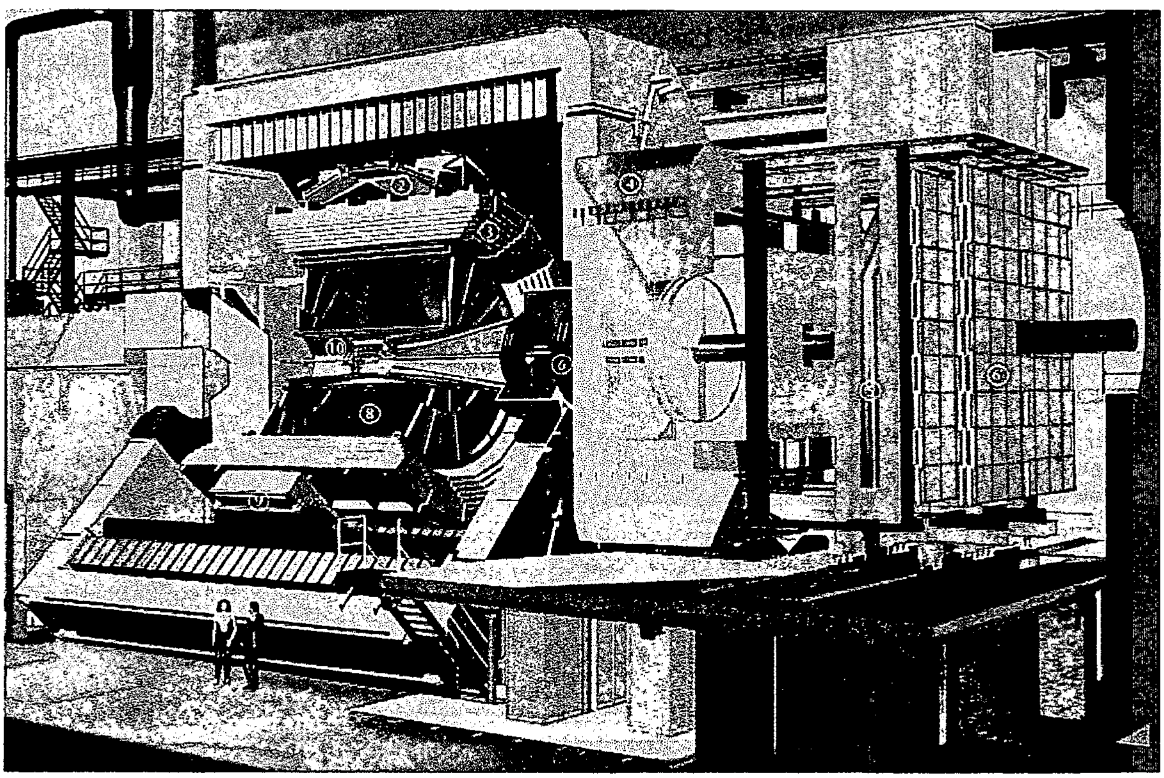

Fig. 1.5: Three dimensional view of the ALICE experiment; (1) L3 Magnet, (2) HMPID, (3) TOF, (4) Dipole Magnet, (5) Muon Filter, (6) Trigger Chambers, (7) Absorber, (8) TPC, (9) PHOS, (10) ITS [7].

- **ALICE**

The existing L3 detector will be converted into the ALICE (A Large Ion Collider Experiment) experiment to investigate Pb-Pb collisions. This heavy ion detector will be used to study physics of nucleus-nucleus interactions at LHC energies. At these energies a new phase of matter will be produced, the quark-gluon plasma. By studying the nature of the produced particles the quark-gluon plasma can be characterized. The ALICE detector has been designed to handle extremely large particle multiplicities produced in Pb-Pb collisions (dN/dy ~ 8000). It makes use of the large warm magnet recovered from L3 complemented by a dipole to improve the reconstruction of muon pairs. The inner tracking system (ITS) contains silicon drift chambers and silicon pixel detectors for vertex reconstruction. A cylindrical Time Projection Chamber (TPC) has been chosen as a main tracking device. Diameter and length of the field cage is 5 m. In this high multiplicity environment a good momentum resolution (~10% at 100 GeV/c) and a good two-track separation is necessary. Particle identification is possible by measuring the energy loss with precision of better than 10 %. The drifting electrons are detected by a MWPC.

As can be seen in *Fig. 1.5* a variety of other detectors adds up to the particle identification power of the ALICE experiment: Cherenkov detectors (using CsI photocathodes coupled to a MWPC), a TRD (large area drift chamber with a radiator in front), a Time of Flight detector (TOF) using multi-gap RPCs and $PbWO_4$ crystals for photon energy measurements.

- **CMS**

The CMS (Compact Muon Solenoid) spectrometer consists of a single superconducting solenoid (14 m long and 3 m inner radius), generating a uniform magnetic field of 4 T. Each muon traverses four stations comprising twelve layers of aluminum drift tubes outside the coil in the barrel region and Cathode Strip Chambers (CSC) in the end-cap region due to the higher particle flux complemented by RPCs. The achieved momentum resolution is about 1% at 100 GeV/c and 5% at 1 TeV/c.

The high resolution electromagnetic calorimetry is done by dense (ρ=8.3 g cm^{-3}) and transparent $PbWO_4$ crystals. Scintillation light produced in the crystals is collected by avalanche photodiodes in the barrel region and vacuum phototriodes in the end-cap region. The electromagnetic calorimeter is surrounded by a sampling hadron calorimeter made of brass and scintillators. Their light is collected by wavelength shifting fibres and is then channeled to be read out by Hybrid Photodiodes. The high-quality tracking inside the detector is achieved by ten layers of silicon microstrip detectors which provide the needed granularity and precision. As in ATLAS, close to the interaction region silicon pixel detectors are installed.

- **LHCb**

The LHCb (Large Hadron Collider beauty) experiment is dedicated to B physics experiments at the LHC and will be built in the DELPHI pit. It is sensitive to the forward production of $b\bar{b}$ pairs in the rapidity range $1.6 < |\eta| < 5.3$. The single arm forward spectrometer with an opening angle of 400 mrad detects 10-20% of the $b\bar{b}$ decays. The large Lorentz boost keeps the decaying particles in a cone and due to the longer decay length of the accepted B mesons precise decay-time measurements are allowed. This experiment is able of measuring the asymmetries in the decays of B^0 & $\overline{B}^0$ and to do sensitive tests of the CP-violation in B decays.

Further advantage of this forward geometry is the lower p_T threshold for the trigger and the accessible geometry. Used as a vertex locator 21 layers of silicon microstrip detectors are place perpendicular to the beam. The rest of the tracking detector consists of a silicon microstrip trigger tracker and straw tubes in the outer parts. Two Ring imaging Cherenkov counters with C_4F_{10}, CF_4 and aerogel radiators gives this experiment an excellent hadron (π/K/p) separation capability in the momentum range 2 -100 GeV/c. The Cherenkov photons are detected by HPDs.

A special constructed dipole magnet provides an integral field of 4 T m. The calorimeter consists of a pre-shower detector followed by a "Shashlik" lead-scintillator sampling electromagnetic calorimeter. The hadron calorimeter is based on a scintillating-tile design similar to that designed for ATLAS. Multi-wire proportional chambers are used as muon detectors except for the innermost region, where triple-GEM detectors are used. *Fig. 1.6* illustrates the components of the LHCb detector.

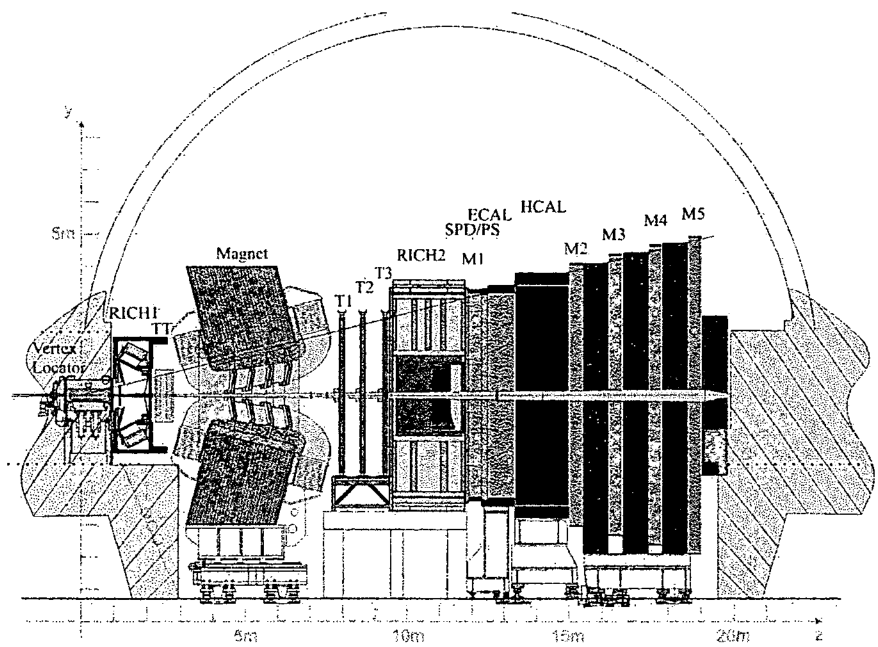

Fig. 1.6: Side view of the single arm forward detector of LHCb [8].

- **TOTEM**

The TOTEM (TOTal and Elastic Measurement) experiment is a forward physics experiment and will measure the total pp cross section. Moreover, it will study the elastic scattering and diffractive dissociation at the LHC. This experiment will add charged particle tracking and trigger capabilities to the CMS experiment over a rapidity interval $3 < |\eta| < 6.8$. The present T2 design is based on the utilization of the GEM technology.

1.3 State of the art of gas detectors

Experiment	
ALICE	TPC (tracker), TRD, HMPID (pad chamber), TOF (MRPC) Muon tracking (pad chamber); Muon trigger (RPC)
ATLAS	TRD (straw tubes), MDT, Muon trigger (RPC, thin gap chambers)
CMS	Muon detector (drift tubes, CSC), RPC for muon trigger
LHCb	Tracker (straw tubes), Muon detector (MWPC, GEM)
TOTEM	Tracker and trigger (CSC, GEM)

Table 1.1: Overview of the gaseous detectors in LHC-experiments

As can be seen above (*Table 1.1*) gaseous and silicon detectors are required to construct up-to-date high energy physics experiments. Silicon detectors have excellent performance, but high cost. Due to the better spatial resolution of a few micrometers, the radiation hardness and the high rate capability semiconductor detectors perform better close to the interaction region. However, at large radius where large areas have to be covered, e.g.: the muon chambers, it is more than unrealistic to use something else as gaseous detectors. In the intermediate region silicon and so called Micro-Pattern Gas Detectors (MPGD) fulfill all the necessary requirements concerning precision, rate capability and radiation hardness [10][11][12].

In the following part, exemplarily the working principles of two standard gas detectors are outlined as they are used in high energy physics and in other fields of science, as well as their problems in environments with high particle fluxes of high-luminosity colliders. The need for low-cost high performance gas devices led to the development of 2nd generation Micro-pattern gas detectors.

1.3.1 Multi-Wire Proportional Chamber

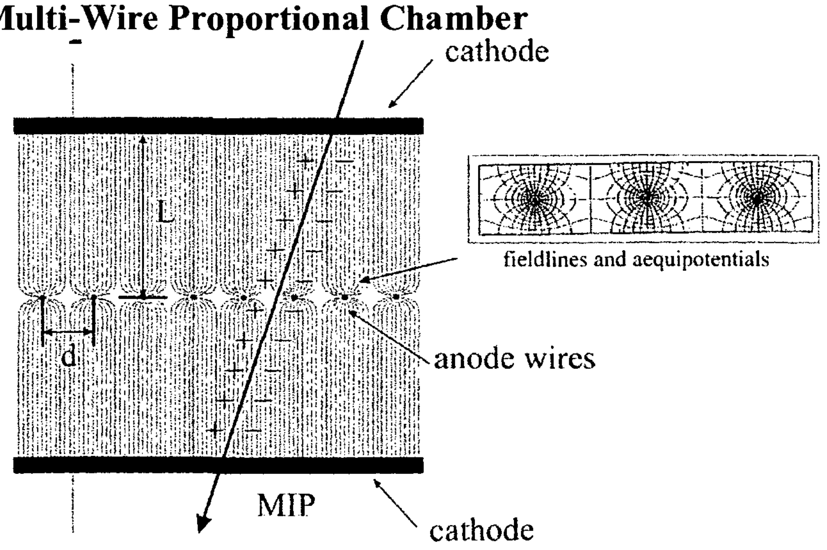

Fig. 1.7: Multi-wire proportional counter and the field map around the wires. The electrons are collected and multiplied by the anode wires, the ions drift to the cathode-plates. Spatial resolution is obtained by the wire position.

In 1968 the multi-wire proportional chamber (MWPC) was introduced by G. Charpak [13]. This gaseous detector has the capability to detect and localize ionizing radiation. A set of thin parallel spaced anode-wires, at typical distance of 2 mm, is set between two cathode-plates (see *Fig. 1.7)*.

Ions released by ionizing particles drift to the cathodes, while the electrons are collected on the wires. The strong electrical field close to the wires (~ 10 μm) leads to charge multiplication. Spatial resolution is given by the address of the fired wire. The wire layers can be assembled in different orientations, in order to obtain two-dimensional resolution. Under the assumption that the distance between two wires is d, the spatial resolution σ_x can be computed to $d/\sqrt{12}$ (σ_x is typically 300 μm at d=1). Hence the upper limit for the resolution is given by the wire spacing, which cannot be reduced arbitrarily due to the electrostatic repulsion of the wires. Therefore limitations in granularity, respectively the spatial resolution are reached.

An improvement was achieved by segmenting the cathode into strips or pads and connecting each pad to single charge sensitive preamplifiers. The ion avalanche drifts to the cathode and induces signals. By charge interpolation *(see Chapter 4.3.1)* the origin of the avalanche is determined. In this way spatial resolutions lower than 100 μm are measurable.

At larger multiplication factors, the slow moving ions modify the electrical field due to positive build-up of space charge. As a consequence the detector gain starts to decrease at higher radiation flux *(see Fig. 1.9)*.

Confronted with the increasing demands in particle physics and other fields of science the MWPC has been continuously improved over the years and a number of generations of MWPC have been developed, such as the drift chamber, the time projection chamber, time expansion and ring imaging chambers. Multi-wire devices of various designs remain a major component in high energy physics *(see 1.2.2)*.

1.3.2 Microstrip Gas Counter

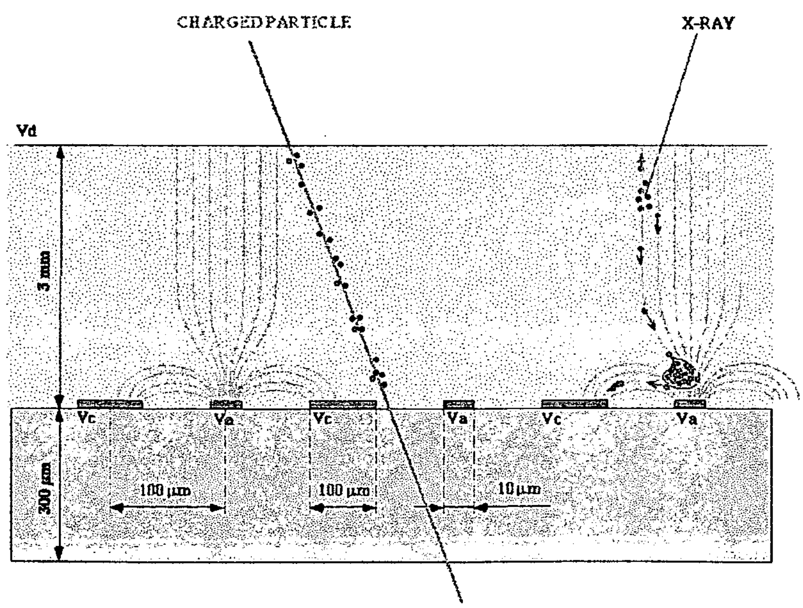

Fig. 1.8: MSGC. Electrons are collected and multiplied by the anode strips, the ions drift to the cathodes; by the narrow spacing short collection times and high spatial resolution is obtained [15].

Introduced in 1988 by A. Oed [14] the Micro-Strip Gas Chamber (MSGC) performs considerably better than the detectors based on the gas wire technique. The wires are replaced by small metal strips engraved on a thin isolating substrate *(see Fig. 1.8)*. These strips are alternatively anode and cathode strips. The photolithography technology used for manufacturing allows a reduction of the electrode spacing by one order of magnitude, correspondingly improving the multi-hit capability.

The distance between them is typical 100 µm and the width of the anode-strips is about 10 µm. On the application of suitable potentials, negative with respect to the anode, electrons, which are released in the drift region move toward the anode strip. In the high electrical field of the anode the electrons start to multiply and detectable signals are generated.

The strips are made of gold or chromium on a insulator substrate (e.g.: glass with diamond coating). The small anode-cathode spacing results in a short ion collection time and therefore a reduction of the space-charge build-up. The spatial resolution of a MSGC is typically from 30 to 40 µm and typical gains of 10^4 are reachable.

The high rate capability due to the fast collection times of these devices allows an application in environments with high particle fluxes. A high rate operation requires a reduced resistivity substrate (in the range from 10^9 to 10^{12} Ωcm) [16]. The excellent localization, high rate capability and good granularity make them useful for charged particle tracking at high luminosity colliders, among other applications.

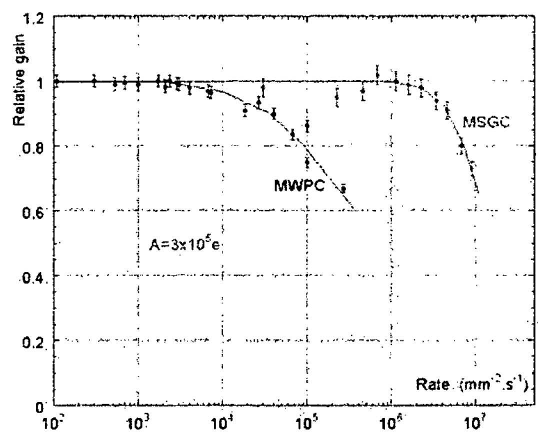

Fig. 1.9: Dependence of the relative gain on the rate. At rates higher than 10 kHz/mm^{-2} the relative gain of a MWPC decreases due to space charge accumulation [15].

1.3.3 The Problems

Traditional gas devices (based on the wire technology as MWPCs) suffer from the basic problem that they cannot provide a rate capability of more than 10 kHz/mm^2. *Fig. 1.9* shows the gain limitation at increasing rates due to space charge accumulation. With a MSGC, depending on the resistivity of the used substrate the detectors can operate under higher particles fluxes at a stable gain. One of their drawbacks, however, are the discharges resulting in irreversible damage to the anodes and cathodes in the presence of high flux of highly ionizing particle.

All micro-pattern detectors suffer from the appearance of discharges during their operation. When the total charge in the avalanche exceeds the Raether limit *(see Chapter 2.4)*, which is between 10^7 and 10^8 electron-ion pairs, the electrical field in front and behind the avalanche is increased locally. This enhancement induces the fast growth of a filament-like streamer. In the high electrical fields and with the small gaps typical of micro-pattern devices, this leads to a discharge. Due to the statistical behavior of the ionization process, also abnormal large energy losses can trigger the harmful discharges.

The probability and the energy released by a discharge increase with the voltage difference between anode and cathode. In order to protect the micro-pattern structure, the detector must be operated at moderate cathode-strip voltages, which leads to a worse detection efficiency due to less charge multiplication.

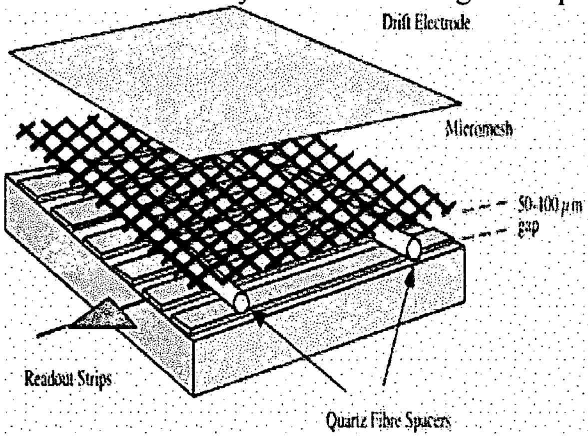

Fig. 1.10: In a MicroMegas device the metallic micromesh separates the drift region from the high field amplification region (~100kV/cm) [21].

The other weakness revealed after detailed long-term studies, the aging effect. Aging means the slow but continuous deterioration of the detector under sustained irradiation. Basically chemical reactions of the ionized gas with the detector material lead to this permanent damage of the detector (e.g. anode and cathode of a MSGC are covered by a thin polymer film).

Due to these problems a variety of new generation of MPGD emerged based mainly on the working principles of the MSGC.

They combine rate capability of higher than 10^5 Hz/mm^2 at high gains around 10^5 with a good time resolution down to 3 ns and good non-aging properties.

The family of micro-pattern gas detectors contains for example the Compteur à Trous (CAT) [17], which makes use of the avalanche production in narrow holes. *Fig. 1.10* shows the MicroMegas gaseous detector [18], which exploits high gain properties of narrow-gap parallel plate multiplication. The Microdot (*Fig. 1.11*) device is a matrix of individual circular counters laid on a substrate [19].

In [12] [20] [21] detailed discussions on this topic can be found. All these detectors lack the fragility of the thin anodes; they reach gains by avalanche multiplication, produced with controlled and reliable photolithographic methods. They are more reliable and free of size limitations.

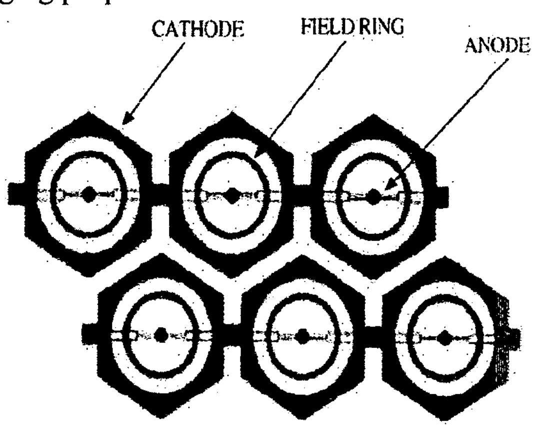

Fig. 1.11: The MicroDot is a gaseous pixel device containing a dense pattern of individual proportional counters made of anode dots surrounded by ring cathodes [21].

1.4 The Gas Electron Multiplier Approach

Among these new devices the Gas Electron Multiplier (GEM), introduced by Sauli [22] in 1996, poses a promising candidate for a fast, high performance, non-aging detector technology, which is applicable in high luminosity collider experiments [23] [24] [25].

Due to the fact that the focus of this thesis lays on the Gas Electron Multiplier, the GEM technology will be discussed in the following chapters. At this point the differences to the other gaseous devices introduced in *Chapter 1.3.3* shall be outlined.

- Generally all the MPGDs are sturdy enough to withstand discharges without damage. This may not the case for the readout electronics. The required gain can be shared between two or more GEM-foils by cascading them *(see Chapter 2.3)*. In this way the required high gains are accessible, whereas each GEM-foil operates at a voltage below the discharge limit. The discharge probability is lower than in single amplification devices introduced above [26].

- The proportional charge amplification in the GEM-holes and the charge detection (readout) on the anode are separated. Therefore the propagation of accidental discharges to the sensitive readout electronics is avoided and the electronics is protected.

- Signals are fast due to the decoupling of ions and electrons in the amplification region (9.7ns rms in $ArCO_2$ (70/30) [27]). Hence only electrons contribute to signal induced on the readout board. GEM signals lack the ion tail.

- Depending on the application the shape of the GEM-foil and the readout pattern are adaptable. In that *(see Chapter 4 & 5)*. For this reason a wide freedom in the detector design is possible.

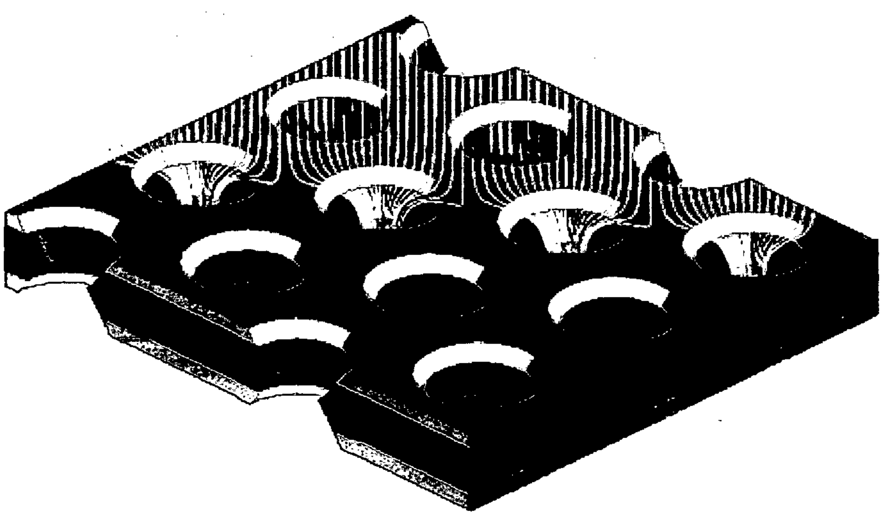

Fig. 1.12: Three dimensional image of a GEM-foil. On the application of a voltage difference across top and bottom side of the GEM electrons released by ionization in the electrical field above the GEM are guided into the GEM-holes, where they are multiplied [28].

Chapter 2

Physics of a Gaseous Detector

This chapter gives a short summary on the most relevant physical processes in gaseous detectors. In order to understand their properties and their behavior a basic knowledge of the physical phenomena is necessary and essential.

Particle detectors are devices to detect atomic particles, i.e.: ions, photons, atomic nucleii or elementary particles. The sensitivity of gaseous detector is mainly based on electromagnetic interactions. When ionizing particles traverse a gaseous or condensed medium, they interact with it by ionizing the medium along their tracks through the detector material.

Depending on the particle, which is going to be measured, also the strong or the weak interaction can be exploited, producing secondary charged particles, which can be detected by a gaseous detector.

For the detection of photons physical processes like photoelectric absorption, Compton scattering or pair production convert the photon energy into detectable charged particles. For the detection of neutrons, depending on the energy, different nuclear reactions are available to make the detector sensitive for the neutral particles (e.g.: the $B^{10}(n,\alpha)Li^{7}$ reaction for low energy neutrons).

Neutrinos can only be detected by their weak interaction with nucleii or the leptons, because the conservation of the lepton number, leads to the emission of a charged particle or a neutral lepton.

2.1 Interaction of Charged Particles

The Coulomb interactions between the electric field of the detector medium and the particle result in an energy loss. The major contribution to the energy loss comes from the excitation and ionization of the medium. For example, a π meson leaves a track of ionization along its trajectory.

$$\pi A \rightarrow \pi A^{+}e^{-}$$

The pion can also liberate electrons by the production of intermediate excited states A^{*}. If the excitation energy of A^{*} is higher than the ionization energy of a 2nd species, B present in the gas, A^{*} de-excites with an interaction with an atom of the species B:

$$\pi A \rightarrow \pi A^{*} \rightarrow A^{*}B \rightarrow AB^{+}e^{-}$$

The electrons emitted in these exemplary reactions are called primary electrons. If their energy is high enough, they loose their energy *(see Chapter 1.1.2)* by further ionizing the gas.

Energy loss due to other physical processes as Bremsstrahlung, Cherenkov light and transition radiation production is negligible in gaseous detectors.

2.1.1 Energy Loss, Bethe-Bloch Formula

The electromagnetic energy loss of a heavy ($m>m_e$) charged particle traversing a medium (even thin materials) is a statistical process, a result of many discrete interactions. On penetrating the material the particle scatters inelastic upon molecules, atomic shell electrons and nucleii. If the energy deposit is larger than the binding energy of the atom ionization takes place. Otherwise the collision leads to an excitation of the atoms in the material. The average differential energy loss of heavy particles per unit length due to ionization is described by the Bethe-Bloch equation [29][30]. In the framework of relativistic quantum mechanics it can be written as follows:

$$-\frac{dE}{dx} = Kz^2 \frac{Z}{A} \frac{1}{\beta^2} \left[\frac{1}{2} \ln \frac{2m_e c^2 \beta^2 \gamma^2 T_{max}}{I^2} - \beta^2 - \frac{\delta}{2} \right] \quad \textbf{(Equ. 2.1)}$$

In *Equ. 2.1* N_A is Avogadro's number [mol^{-1}], A [$g\ mol^{-1}$] and Z denote the atomic mass and the atomic number, $K=4\pi N_A r_e^2 m_e c^2$ [$MeV\ cm^2\ mol^{-1}$] with r_e the Bohr radius of the electron, $m_e c^2$ is the rest energy of the electron, c the velocity of light, I the mean excitation energy of the absorber, z the charge of incident particle and δ the density effect correction. The parameter β is the velocity of the charged particle in units of c and $T_{max}=2m_e c^2\beta^2\gamma^2$, the maximum kinetic energy, which can be transferred to a free electron in a single collision. The units are chosen so that, dx is measured in mass per unit area e.g.: $g\ cm^{-2}$.

Fig. 2.1 shows typical average energy loss spectra in different absorbers (e.g.: gaseous helium) for three particles. A good approximation for I is given by $I=Z^{0.9}.16$ eV [29]. *Equ. 2.1* is suitable up to energies of a few GeV with an error of a few percent. At lower energies corrections (shell correction) for tightly bound electrons must made *(Fig. 2.2)*. At higher energies radiative effects begin to be important. The differential energy loss (or stopping power) depends only on $v/c=\beta$ and not on the mass of the incident particle. After a decrease dominated by the β^{-2} term, the energy loss reaches a minimum. As visible in *Fig. 2.1*, dE/dx has a minimum for $\beta\gamma$~3. For Z/A=0.5 the energy loss of minimum ionizing particles is roughly given by 1.4 $MeV\ g^{-1}cm^2$. The stopping power continues with a logarithmic (relativistic) rise, until the Fermi Plateau is reached.

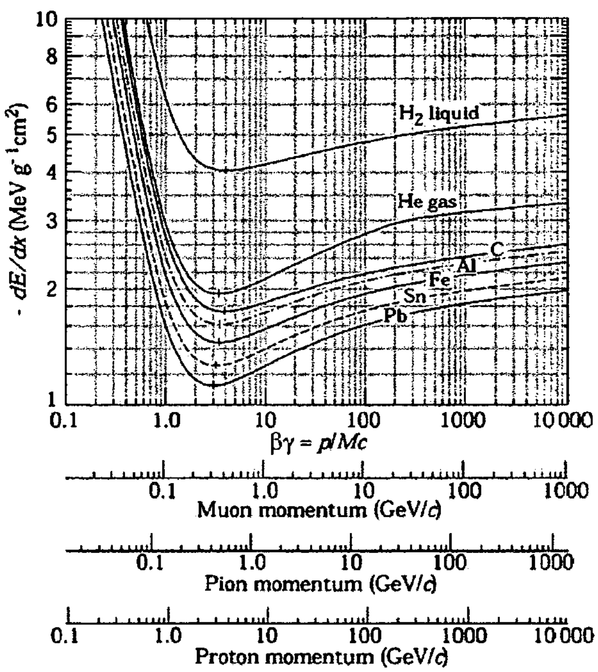

Fig. 2.1: Average energy loss in different absorber materials as a function of $\beta\gamma$ [30].

Most relativistic particles (e.g. cosmic ray muons) have a differential energy loss close to the minimum. These particles are called MIPs (Minimum Ionizing Particles). According to the relation $\beta\gamma=p/mc$ simultaneous measurements of the differential energy loss and the momentum p allows particle identification.

2.1.2 Primary and Total Ionization

A photon *(see Chapter 2.2)* or fast charged particles interact electromagnetically with the absorber material. In the case of the photon this happens is one single event, which leads to the production of one primary electron. The charged particle undergoes a discrete number of ionizing collisions, which liberate primary electron-ion pairs in the medium. If the ejected primary electrons n_p have enough energy (larger than the ionization potential of the absorber) they can further ionize the gas atoms and produce secondary electrons n_s (until their available energy is below the ionization energy). The sum of these two contributions equals the total number of electron-ion pairs n_{TOT} *(Equ. 2.2)*.

$$n_{TOT} = n_p + n_s \qquad \textbf{(Equ. 2.2)}$$

Gas	Z	A	density [g/cm^3]	I_0 [eV]	W_i [eV]	dE/dx [keV/cm]	n_p [i.p./cm]	n_{TOT} [i.p./cm]
H_2	2	2	8.38×10^{-5}	15.4	37	0.34	5.2	9.2
He	2	4	1.66×10^{-4}	24.6	41	0.32	5.9	7.8
O_2	16	32	1.33×10^{-3}	12.2	31	2.26	22	73
Ne	10	20.2	8.39×10^{-4}	21.6	36	1.41	12	39
Ar	18	39.9	1.66×10^{-3}	15.8	26	2.44	29.4	94
Xe	54	131.3	5.49×10^{-3}	12.1	22	6.67	44	307
CO_2	22	44	1.86×10^{-3}	13.7	33	3.01	(34)	91
CH_4	10	16	6.70×10^{-4}	13.1	28	1.48	16	53

Table 2.1: Properties of several gases. Energy loss and the number of ion pairs per unit length are given at atmospheric pressure for minimum ionizing particles. Z, A are the atomic number and the mass number, I_0 the ionization energy, W_i the average ionization energy, dE/dx the average energy loss (i.p. = ion pairs). n_p and n_{TOT} are the number ion-electron pair created primarily and totally [29].

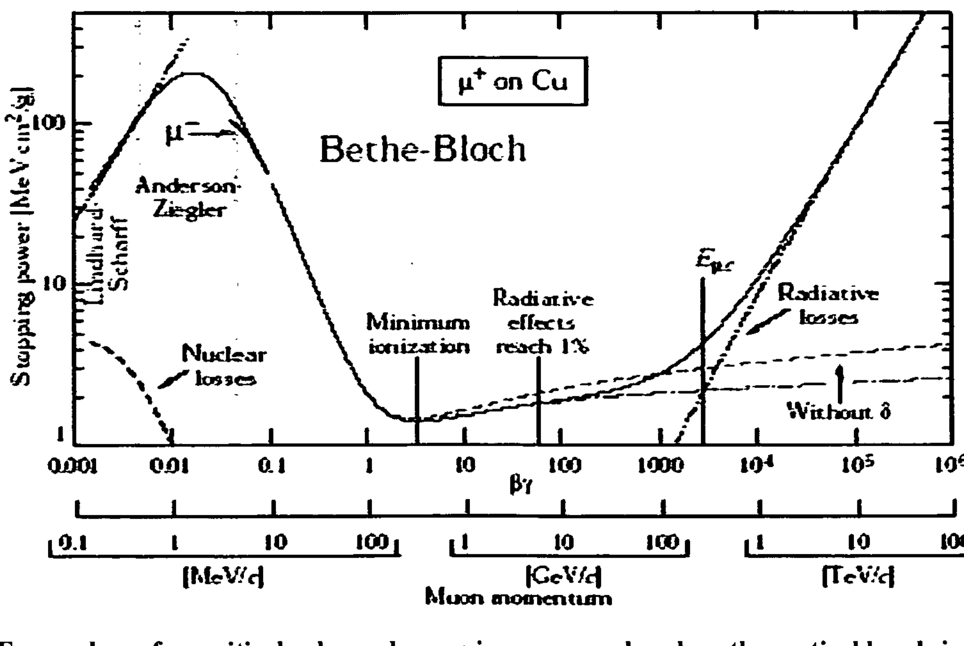

Fig. 2.2: Energy loss of a positively charged muon in a copper absorber, the vertical bands indicate the boundaries for the corrections at lower energies [30].

The number of primary electrons is usually measured. The values in *Table 2.1* are deduced from inefficiency measurements in adequate gaseous detectors.

$$P(k,n_p) = \frac{n_p^{\,k}}{k!} e^{-n_p} \quad \textbf{(Equ. 2.3)}$$

Assuming that the ion pair production in a thin gas layer is caused by a small number of independent interactions the probability to produce k primary electrons by n_p ionizations is given by the Poisson distribution *(Equ. 2.3)*. The average value is n_p. *Equ. 2.4* provides the possibility of deducing the number of primary electrons by measuring the inefficiency 1-ε of a perfect detector, which is capable of detecting every ion pair produced in the sensitive gas volume. In practice the efficiency ε is reduced by the imperfections of real detectors.

$$P(0,n_p) = e^{-n_p} = 1 - \varepsilon \quad \textbf{(Equ. 2.4)}$$

The number of primaries n_p is approximately linearly dependent on the average atomic number [29]. The total number of produced electrons is proportional to the energy deposited in the absorber and can be calculated by *Equ. 2.5*. The parameter W_i is the effective average energy to produce one electron-ion pair and ΔE the total energy loss in the gas. *Equ. 2.6* is applied in the case of a gas mixture. c_n denotes the weight fraction of the n^{th} gas component of the absorber. ΔE_n and $(W_i)_n$ are the corresponding parameters.

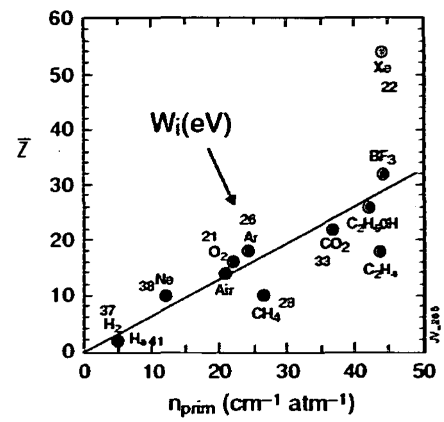

Fig. 2.3: Dependence of the number of primaries on the average atomic number [31.

For example, according to *Table 2.1,* in the gas mixture $ArCO_2$ (70:30) 93 total (31 primary) ion pairs are produced in a 1 cm thick gas volume. Measuring the total ionization gives the charge distribution, respectively the energy spectrum. The shape of this spectrum depends on the statistics of the ionization process. The production of the primary electrons is Poisson distributed. The distribution of the total number of electron-ion pairs n_{TOT} is Landau distributed *(see Chapter 2.1.3)*.

$$n_{TOT} = \frac{\Delta E}{W_i} \quad \textbf{(Equ. 2.5)} \qquad n_{TOT} = \sum_n c_n \frac{\Delta E_n}{(W_i)_n} \quad \textbf{(Equ. 2.6)}$$

2.1.3 Statistics of the Ionization Process

A closer look at the interaction mechanism shows, that the individual collisions can be grouped in two classes: close collisions with large energy transfer (ionizations) and distant collisions with a smaller energy transfer (ionizations and atomic excitations).

Primary electrons that have a high enough kinetic energy (few keV) to further ionize the gas atoms are called δ-electrons.

Equ. 2.1 describes only the average energy loss. For thin absorbers the energy loss distribution has large fluctuations around the average value.

The energy distribution in a thin media is strongly asymmetric and can be written as

$$F(\lambda) = \frac{1}{\sqrt{2\pi}} e^{-\frac{1}{2}(\lambda + e^{-\lambda})} \quad \textbf{(Equ. 2.7)}.$$

$$\lambda = \frac{\Delta E - \Delta E_{mp}}{\xi} \quad \textbf{(Equ. 2.8)}, \qquad \text{with}$$

$$\xi = \frac{2\pi z^2 e^4}{m_e c} N_A \frac{Z}{A} \frac{1}{\beta^2} \rho x$$

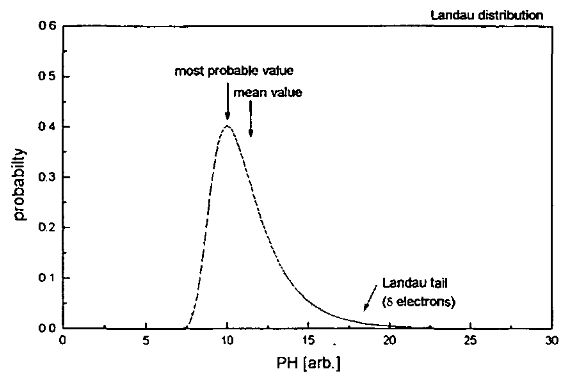

Fig. 2.4: The asymmetric Landau distribution; the mean value is bigger than the most probable value.

λ in *Equ. 2.7 & 2.8* represents the normalized deviation from the most probable energy loss ΔE_{mp}, ξ the average energy loss of the Bethe-Bloch formula, x the thickness of the absorber in cm and ΔE the actual energy loss in a layer of a thickness x.

Fig. 2.4 shows the characteristic shape of the Landau distribution. One has to distinguish the mean and the most probable energy loss. The events in the long tail are caused by the large energy transfer collisions (δ-electrons). The energy resolution of such a device is poor. The resolution can be improved, if thickness of the detector exceeds the absorption length of the particle, because then, according to the central limit theorem, the Gaussian statistics dominate.

2.2 Interaction of photons

The attenuation of a photon beam traversing a medium of a thickness D can be written as

$$\frac{I}{I_0} = e^{-\mu D} \quad \textbf{(Equ. 2.9)}.$$

I_0 denotes the initial intensity of the beam. D [g/cm^2] =d [cm] ρ [g/cm^3] is the reduced thickness and μ the mass absorption coefficient in cm^2 g^{-1}. The probability of interaction can be expressed in terms of the cross section σ.

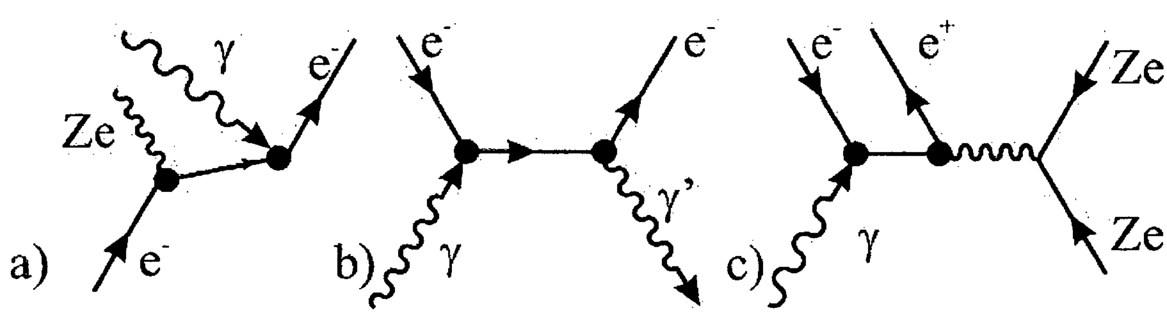

Fig. 2.5: Feynman diagrams of the photoelectric effect (a), the Compton scattering (b) and the pair production (c).

The total cross section σ_{TOT} *(Equ. 2.10)* is given by the sum of all contributions σ_i. The main contributions are explained below *Fig. 2.6*. The mass absorption coefficient is related with cross section by *Equ. 2.11*. A is the atomic mass number and N_A Avogadro's constant.

$$\sigma = \tau + \sigma_{coh} + \sigma_{incoh} + \kappa = \sum_i \sigma_i \qquad \textbf{(Equ. 2.10)}$$

$$\mu = \frac{N_A}{A}\sigma = \frac{N_A}{A}\sum \sigma_i \qquad \textbf{(Equ. 2.11)}$$

As illustrated in *Fig. 2.6*, depending on the photon energy E_γ, photons interact with matter in three different ways. At lower energies the photoelectric conversion is the dominant process. At energies below 0.5 MeV Compton scattering begins to take over and at higher energies pair production is more probable. *Fig. 2.5* illustrates the Feynman diagrams for these three physical processes.

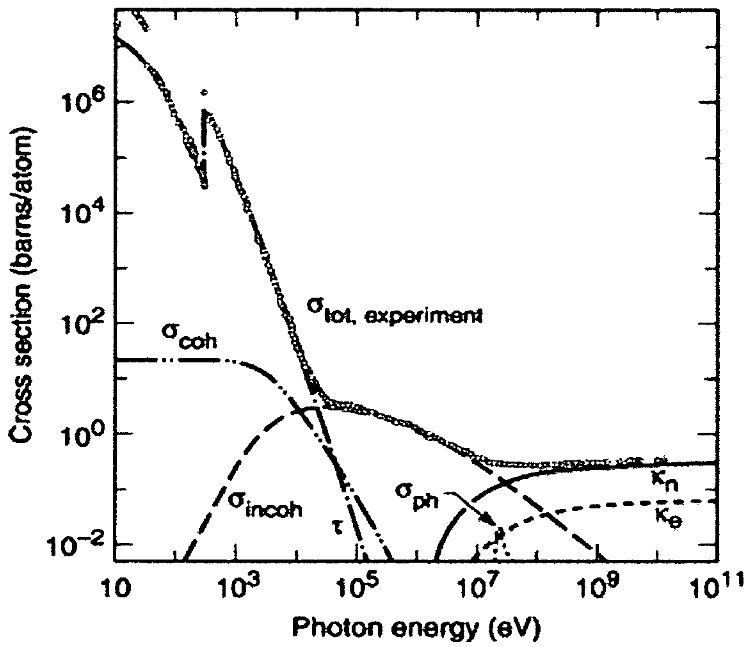

Fig. 2.6: Total photon cross section in carbon as a function of the energy; showing the contributions of the three different processes: τ the atomic photo-effect (electron ejection, photon absorption), σ_{coh} the coherent scattering (Rayleigh scattering – atom neither ionized nor excited) and σ_{incoh} the incoherent scattering (Compton scattering of an electron), κ_n and κ_e the pair production in the nuclear and in the electron field. σ_{ph} is the photo nuclear absorption coefficient (nuclear absorption of a photon, usually followed by the emission of a neutron) [30].

- **Photoelectric effect (E_γ< 0.5 MeV):** $\gamma + Ze^- \rightarrow \gamma + (Z-1)\,e^-$

  If the energy of the incident photon E_γ exceeds the binding energy E_i of the electrons in the shell i, the photon is absorbed completely. Energy and momentum are transferred to the interaction partner and ionization and excitation of the atom take place. As illustrated in *Fig. 2.6* the photoelectric absorption has a maximum at the energy of the absorption edges. In the case of ionization the ejected photoelectron has the kinetic energy $E_{kin} = E_\gamma - E_i$. The excited atom can return to its ground state by emitting a fluorescence photon filling the vacancy with an electron form a higher shell or by transferring the energy to electrons within the atom (radiationless Auger-process).

The conservation of the momentum leads to a recoil of the nucleus. Therefore only electrons close to the nucleus contribute to the photoelectric absorption cross section τ. The total photoelectric cross section in the non-relativistic range far away from the absorption edges is proportional to $Z^5/E_\gamma^{3.5}$ [cm^2/atom]. Details to the photoelectric cross section can be found in [32]. Depending on its energy the primary photoelectron is emitted in a preferential direction. Up to 30 keV, the direction of emission is nearly orthogonal to the incoming photon direction, which limits the spatial resolution of such a detector [29].

- **Compton scattering ($E_\gamma \sim$ 1 MeV):** $\gamma + e^- \rightarrow \gamma' + e^{-'}$

$$E = \frac{E_0}{1+\varepsilon(1-\cos\theta)} \quad \textbf{(Equ. 2.12)},$$

with $\varepsilon = \frac{E_0}{m_e c^2}$

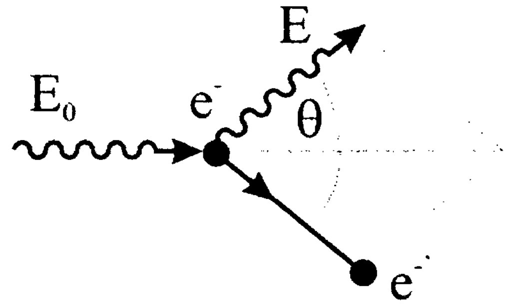

Fig. 2.7: Kinematics of the scattering process.

Above the highest atomic energy level Compton scattering begins to be the dominant process. The binding energy of the electron is negligible compared to the photon energy.

Only a fraction of the incident photon energy E_0 is transferred on a quasi-free electron. The energy of the scattered electron is E_0-E. The energy of the scattered photon is described by *Equ. 2.12* [33] [34]. θ is the scattering angle of the photon and $m_e c^2$ the rest mass of the electron. The collision kinematics is shown in *Fig. 2.7*. In the framework of quantum mechanics the differential cross section (Klein-Nishina formula) and the angular distribution of this effect is provided [38]. For low energies (<10 keV, $\alpha = \varepsilon \sim 0.1$) the angular distribution of the Compton photon is symmetric around 90°. At higher energies the forward scattering prevails *(Fig. 2.8)*.

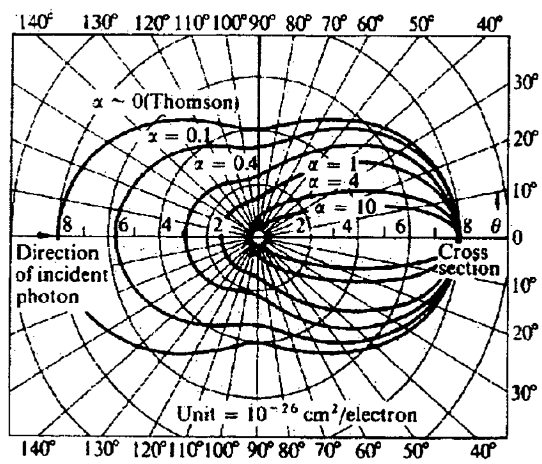

Fig. 2.8: Polar plot of the differential Compton cross section as a function of the photon scattering angle for several photon energies [35].

Pair production (E_γ >1.022 MeV): $\gamma + Ze \rightarrow e^-e^+ + Ze$
The pair production process is energetically possible, when the photon energy exceeds twice the rest mass energy plus the recoil energy, which is transferred to the nucleus. Due to the $m_{nucleus} >> m_e$ this threshold energy is about $2m_ec^2$.

$$\sigma_{pair} \approx C_1 Z^2 (\ln 2\varepsilon - C_2) \qquad \textbf{(Equ. 2.13)}$$

When the photon energy approaches about 10 MeV it becomes the dominant process *(Fig. 2.6)*. For large photon energies the cross section of pair production can be approximated by *Equ. 2.13*. C_1, C_2 are constants and ε is defined as in *Equ. 2.12*.

2.3 Charge Transport in Gases

An understanding of the motion of electrons and ions is essential as these factors influence many operation characteristics of gaseous detectors.

2.3.1 Filling Gas

Restrictions in the choice of counter gases are mostly set by the specific requirements of the detector (no aging, high rate capability, high gain ...). A small diffusion leads to a good spatial resolution. Fast gases are necessary to keep the dead time small at high rates. In order to run a detector efficiently, it is necessary that the electrons do not recombine with the gas molecules (attachment). Therefore, electronegative gases containing oxygen have to be avoided. Noble and hydrocarbon gases are characterized by low electron attachment coefficients. In noble gases the multiplication process starts at lower electrical fields, compared to complex molecules (e.g. CH_4). For the detection of MIPs gases are desirable having a high specific ionization, because this ensures a high number of primary electrons. Hence heavy rare gases as xenon and krypton seem to be the best choice, but they are expensive. Argon is a good compromise.

In the gas multiplication process electrons collide with neutral gas atoms liberating electrons in an ionization process or exciting the gas atoms. The excited atoms may return to their ground states by the emission of photons (from the visible to the ultraviolet range), which again interact with the gas and produce additional charges. In that way the proportionality between the primary electrons and the multiplied charge in the detector is disturbed. In order to avoid this charge increase small amounts of polyatomic gases can be added to the counting gas. Polyatomic gases allow radiatonless transitions due to the vibrational and rotational states. Without further ionization the photons are absorbed by a so-called quenching gas (e.g. CO_2, CH_4 ...). The quenching efficiency roughly increases with the number of atoms in the molecule. Suitable in this case is isobutan (C_4H_{10}). Organic compounds, however, tend to cause aging effects in the detector and are generally flammable, which requires special safety precautions. Therefore a suitable mixture of a counting gas and a quencher is essential for an effective and stable operation of the gaseous detector.

2.3.2 Diffusion

Charges produced by ionizing events loose their energy in multiple collisions with the gas atoms. In absence of an external electrical field they come quickly to a thermal equilibrium with the gas and eventually recombine. Their average energy E_T is $3/2kT = 40meV$ at normal conditions (STP) and their energy distribution is described by the Maxwell distribution *(Equ. 2.14)*. E is the energy; T is the temperature in degree Kelvin, k the Boltzmann factor and C a probability constant.

$$F(E) = C\sqrt{E}e^{-\frac{E}{kT}} \quad \textbf{(Equ. 2.14)}$$

The average thermal velocity of the electrons is about 10^7 cm/s, whereas the speed of the positive ions is on the order of 10^4 cm/s. A localized charge distribution diffuses following a Gaussian law *(Equ. 2.15)*.

$$\frac{dN}{N} = \frac{1}{\sqrt{4\pi Dt}} e^{\left(-\frac{x^2}{4Dt}\right)} dx \quad \textbf{(Equ. 2.15)}$$

Where dN/N is the fraction of charges found in the dx at a distance x from the origin after a time t; D denotes the gas dependent diffusion coefficient. *Equ. 2.16* denotes the standard deviation of the distribution for the linear and the volume diffusion.

$$\sigma_x = \sqrt{2Dt} \qquad \sigma_v = \sqrt{3}\sigma_x = \sqrt{6Dt}$$

(Equ. 2.16).

The spread of the charge cloud increases proportional with √t. For example, the radial spread of ions in air after one second is about 1 mm [29]. The average mean free path in the diffusion process is

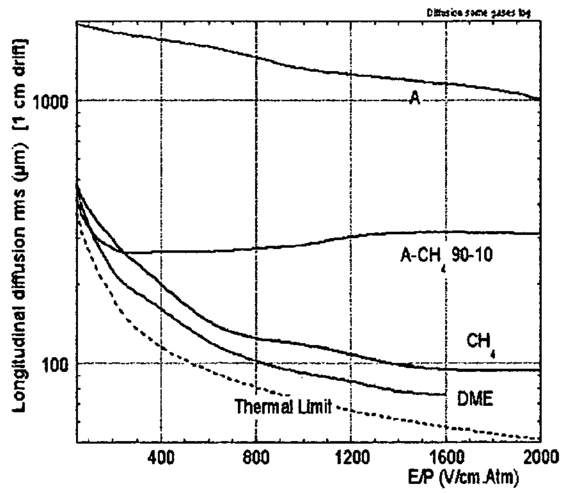

Fig. 2.9: Longitudinal diffusion of electrons in gases as a function of the reduced electrical field E/P. P is the gas pressure [39].

$$\lambda = \frac{1}{N\sigma(E)} \quad \textbf{(Equ. 2.17),}$$

with σ(E) the energy dependent collision cross section and $N=\rho N_A/A$ the number of molecules per unit volume It should be mentioned, that the diffusion constant D is influenced by an outer electrical field $\bar{E}$ and depends on its relative orientation, so that $D_\perp \neq D_\parallel$. *Fig. 2.9* shows the longitudinal ($\parallel \bar{E}$) diffusion of electrons for different gases.

2.3.3 Drift

2.3.3.1 Mobility of Ions

On the application of an electrical field across the gas volume, a net movement of the ions along the field direction is observed. The average velocity of this slow motion (compared to the instant velocity u^+) is called the drift velocity w^+, which is a linear function of the reduced electrical field E/P.

It is therefore convenient to define a quantity μ^+, called mobility *(Equ. 2.18)*.

$$\mu^+ = \frac{u^+}{E} \qquad \textbf{(Equ. 2.18)}$$

Gas	Mass number	u^+ [10^5 cm/s]	D^+ [cm^2/s]	μ^+ [cm^2/Vs]	λ [10^{-5} cm]
H_2	2.02	1.8	0.34	13.0	1.8
He	4.00	1.3	0.26	10.2	2.8
Ar	39.95	0.41	0.04	1.7	1.0
O_2	32.00	0.46	0.06	2.2	1.0
H_2O	18.02	0.61	0.02	0.7	1.0

Table 2.2: Thermal velocity u^+, diffusion coefficient D^+, mobility μ^+ and mean free path λ of ions in their gas at normal conditions [45].

The fact, that the average energy of the ions remains almost unmodified during the drift to the cathode, leads to the constant mobility. The famous Einstein relation *(Equ. 2.19)* correlates the diffusion constant D^+ with the ion mobility μ^+, if a thermal equilibrium is reached.

$$\frac{D^+}{|\mu^+|} = \frac{kT}{e} \qquad \textbf{(Equ. 2.19)}$$

Typical values for the parameters in *Equ. 2.18 & 2.19* can be found in [29] and *Table 2.2*. Ions moving in a time t over a length L diffuse with a probability distribution expressed by *Equ. 2.15*. Its standard deviation is given by Equ. 2.20. Therefore the r.m.s linear diffusion is independent of the nature of the ions and the gas.

$$\sigma_x = \sqrt{2Dt} = \sqrt{\frac{2kTw^+t}{eE}} = \sqrt{\frac{2kTL}{eE}} \qquad \textbf{(Equ. 2.20).}$$

2.3.3.2 Electrons

The motion of charged particles in the presence of an electrical field can be understood in terms of an equation of motion (Langevin equation) under the assumption that the electron-gas interaction can be described on a macroscopic scale as a frictional force [36]:

$$m\dot{\bar{v}} = e\bar{E} + e(\bar{v}x\bar{B}) - K\bar{v} \qquad \textbf{(Equ. 2.21),}$$

where m and e are the mass and the charge of the particle and $\bar{v}$ its velocity. K describes the frictional force proportional to $\bar{v}$, caused by the collisions of the particle with the gas molecules. τ=m/K has the characteristic of a time.

With B=0 and for t>>τ, the solution of *Equ. 2.21* is a constant. Hence the derivative in respect of the time is zero and the average drift velocity is given by the Townsend expression. *(Equ. 2.22)*. Therefore, in the framework of a simplified electron transport theory the mobility μ for electrons is introduced, and it denotes the proportionality of the electrical field and the drift velocity.

$$v = \mu E = \frac{eE}{m}\tau$$

$$\mu = \frac{e}{m}\tau \qquad \textbf{(Equ. 2.22).}$$

The proportional factor e$\bar{E}$/m in *Equ. 2.22* corresponds to the acceleration that an electron experiences in the electric field. Therefore τ is the average time between two collisions of the electron with the gas molecules and n the average number of encounters along a drift distance x *(Equ. 2. 23)*.

$$n = \frac{x}{v}\frac{1}{\tau} \qquad \textbf{(Equ. 2.23)}$$

In the electrical field the electrons gain energy and they loose it partly in the consequent collisions. If ε_E represents part of the equilibrium energy of the electron and $\Delta\varepsilon$ the average fraction of energy lost in a collision, the energy balance can be written as

$$n\Delta(\varepsilon)\varepsilon_E = e|\bar{E}|x \qquad \textbf{(Equ. 2.24).}$$

Rewriting this equation leads to:

$$\Delta(\varepsilon)\varepsilon_E = e|\bar{E}|v\tau \qquad \textbf{(Equ. 2.25).}$$

The total energy ε of the electron is the sum of the equilibrium energy received from the electrical field and the thermal energy. Both energies appear as kinetic energies. Hence the total energy ε is given as:

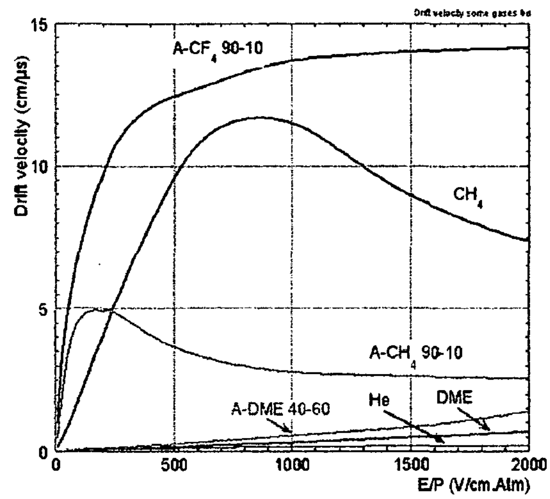

Fig. 2.10: Electron drift velocities of different gases as a function of the reduced electrical field [39].

$$\varepsilon = \frac{1}{2}mu^2 = \varepsilon_E + \frac{3}{2}kT \qquad \textbf{(Equ. 2.26).}$$

In this equation u represents the instantaneous velocity of the electron. Taking into account only ε_E, the average time τ between two collisions is related to the velocity u by the relation

$$\frac{1}{\tau} = N\sigma(\varepsilon)u = \frac{u}{\lambda} \qquad \textbf{(Equ. 2.27).}$$

In this way it is possible to combine *Equ. 2.25*, *Equ. 2.26* and *Equ. 2.27* [36]:

$$v^2 = \sqrt{\frac{\Delta\varepsilon}{2}\frac{eE}{m}\lambda} \qquad \textbf{(Equ. 2.28).}$$

If λ, respectively $\sigma(\varepsilon)$, and $\Delta\varepsilon$ are known the drift velocities can be computed. *Fig. 2.11* and *Fig. 2.12* illustrate the energy dependence of these two parameters, which determine the drift velocity.

Due to the fact that λ is indirect proportional to the pressure P, the drift velocity is generally expressed as function of the reduced electrical field E/P. *Fig. 2.10* shows an example for electron drift velocities for different interesting gases and gas mixtures. More detailed information related to this topic can be found in [37].

The electron-molecule scattering cross section σ and consequently the average time between two collisions is strongly dependent on the total energy ε. This effect is known as the Ramsauer effect.

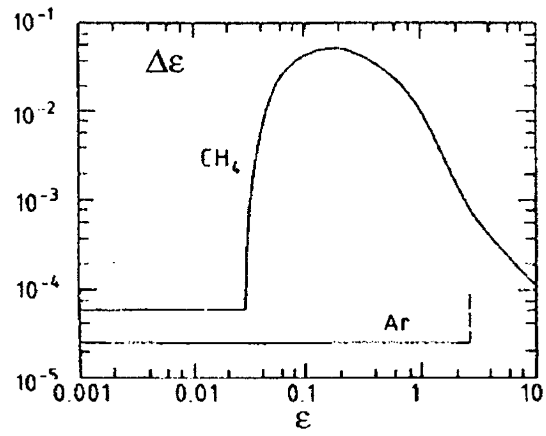

Fig. 2.11: Δε a function of electron energy for methane and argon [41][42].

The electron wavelength approaches the shell values of the molecules and complex quantum mechanical processes take place.

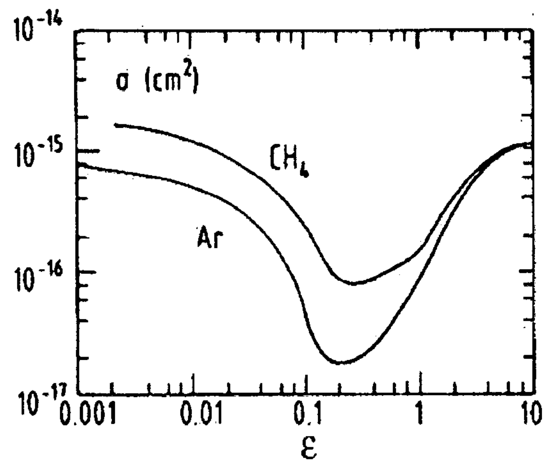

Fig. 2.12: The collision cross section σ as a function of the electron energy (right) [42].

As seen above the velocity of electrons is entirely determined by the cross sections and the external electrical field. In a more rigorous microscopic electron transport theory it can be shown that the drift velocity and the diffusion constant are given by *Equ. 2.29* [40].

$$\bar{v} = \frac{2}{3}\frac{e\bar{E}}{m}\left\langle\frac{\lambda(u)}{u}\right\rangle + \frac{1}{3}\frac{e\bar{E}}{m}\left\langle\frac{d\lambda(u)}{du}\right\rangle$$
$$D = \frac{1}{3}\left\langle\frac{\lambda(u)}{u}\right\rangle \qquad \textbf{(Equ. 2.29)}$$

The averages are to be done on the distribution f(u) of the electron random velocities. Under the assumption of a constant collision time ($d\lambda/du = \lambda/u$) one gets the naïve result

$$\bar{v} = \frac{e\bar{E}}{m}\left\langle\frac{\lambda}{u}\right\rangle \qquad \textbf{(Equ. 2.30),}$$

where one recognizes the product of an acceleration and time between the collisions *(Equ. 2.22)*. In order to deduce the thermal limit of the electron longitudinal diffusion σ_x, one has to replace w^+ with v. The longitudinal diffusion of gases (e.g. CO_2, CF_4, DME ...), which are close to the thermal limit are called "cold". Detectors filled with these gases have a good spatial resolution. Argon, for example, is on the contrary a "hot" gas. Values for the longitudinal diffusion, after on 1 cm of drift, dependent on the reduced electrical field are shown in *Fig. 2.9.* Plots of the properties of the gases ($ArCO_2$, CH_4) used in the measurements presented in this thesis can be found in the Appendix.

2.3.3.3 Electron capture

Additions of even small quantities of electronegative products (e.g air, water or oxygen) in the counter gas influence the drift properties of this gas mixture tremendously. The electron capture reduces the number of electrons n_{TOT}, while drifting over a range x.

$$\frac{n_{TOT}(x)}{n_{TOT}(0)} = e^{-\frac{x}{\xi}} \qquad \textbf{(Equ. 2.31)}, \text{ with } \xi = \frac{|\vec{v}|}{rP_a}$$

where $\vec{v}$ is the drift velocity, P_a the probability for electron attachment and ξ the mean free path for electron capture with the collision rate r=collisions with the molecules of the electronegative gas/time. Attachment coefficients for various gases can be found in the absence of an electrical field [29]. A 1% pollution of Argon with air will remove about 33% of the migrating electrons per cm of drift.

2.3.4 Drift and Diffusion in the Magnetic field

The drift velocity and the diffusion are also affected under the influence of a magnetic field $\vec{B}$. Between the collisions a circular motion due to the Lorentz force $\vec{F} = q(\vec{u}x\vec{B})$ is superimposed (u is the instantaneous electron velocity). Depending on the relative orientation of the electrical field and the magnetic field the gas transport parameters are influenced.

For $\vec{E} \| \vec{B}$ only the transverse diffusion is affected. *Equ. 2.32* shows the decrease.

$$D_T(B) = \frac{D_T(0)}{1+\omega^2\tau^2} \qquad \textbf{(Equ. 2.32)}$$

Here $D_T(0)$ is the transverse diffusion in the absence of a $\vec{B}$-field. ω denotes the cyclotron frequency $|\vec{\omega}| = e|\vec{B}|/m$ and τ the mean time between the collisions.

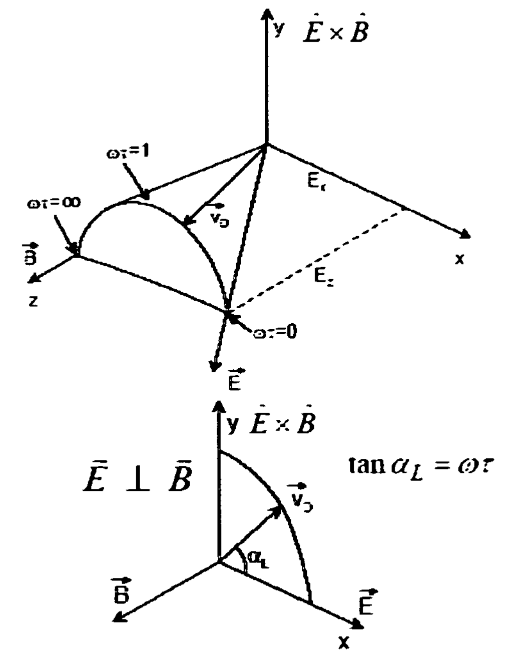

Fig. 2.13: In the case of ωτ=0 the electron follows electrical field lines [44].

Near the amplification structures (wires, GEM-holes ...) the drift velocity $\vec{v}$ is not parallel to the electrical field. The angle between the $\vec{E}$-field and the drift velocity is defined as the Lorentz angle α_L.

$$\tan\alpha_L = \omega\tau = v\frac{B}{E} \qquad \textbf{(Equ. 2.33)}$$

The Langevin equation *(Equ. 2.21)* describes the drift velocity in presence of a $\vec{B}$-field and a $\vec{E}$-field. In that way a general expression for the drift velocity can be derived.

$$\vec{v} = \mu\left|\vec{E}\right|\frac{1}{1+\omega^2\tau^2}\left(\hat{E} + \omega\tau\left(\hat{E}x\hat{B}\right) + \omega^2\tau^2\left(\hat{E}.\hat{B}\right)\hat{B}\right) \qquad \textbf{(Equ. 2.34)}$$

Only in the case of ωτ=0 *(see Fig. 2.13)* the electrons follow the electrical field lines. At larger values of ωτ (higher magnetic fields) the third term in *Equ. 2.34* becomes dominant and the electrons follow the magnetic field lines.

In the case $\vec{B}$ and $\vec{E}$ are not parallel, $\vec{v}$ acquires a 3rd component, orthogonal to both fields. This so called $\vec{E}x\vec{B}$ - effect disappears for ωτ=0 and ωτ → ∞. It is largest for ωτ=1 [43] (*Fig. 2.13*). Due to this effect the precision in determining the position of primary ionization is reduced.

2.4 Gas Amplification

Until now processes dealing with electrical field strengths up to some kV/cm have been discussed. After an electron-ion pair production these fields allow the transportation and collection of the liberated charges. The mean number of electron-ion pairs is proportional to the energy deposited in the gaseous counter. At some point all created pairs are collected and the increase of the drift field does not enhance the anode current (plateau in *Fig. 2.16)*. Detectors working in this region are called ionization chambers; they are generally used for the detection of gamma-rays or as monitoring instruments for large fluxes of radiation.

If the electrical field is further increased electrons that drift to the anode wire are multiplied due to the high electrical fields close due the wire *(Fig. 2.14)*.

$$E(r) = \frac{CV}{2\pi\varepsilon_0}\frac{1}{r} \qquad \textbf{(Equ. 2.35)}$$

$$V(r) = \frac{CV}{2\pi\varepsilon_0}\ln\left(\frac{r}{a}\right) \qquad \textbf{(Equ. 2.36)}$$

At a typical distance of a (tens of a μm) the electrical field *(Equ. 2.35)* is sufficiently high (above 10kV/cm) to gain enough energy in the collisions to further ionize.

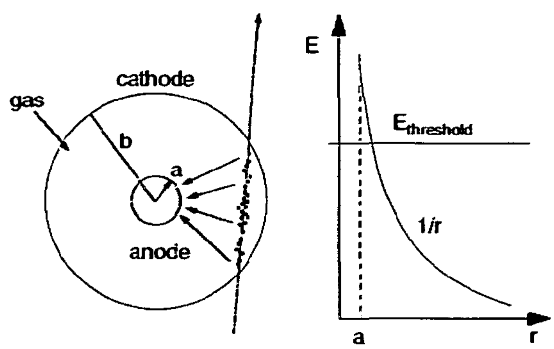

Fig. 2.14: Single wire proportional counter (SWPC) with a plot of the electrical field around the anode wire as a function of the distance from the wire [44].

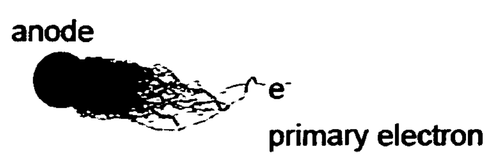

Fig. 2.15: Simulation of the avalanche production of a single electron close to the anode wire (right) [44].

This leads to a multiplication of the primary and secondary electrons in a charge avalanche. The shape of this avalanche is drop-like due to the different drift velocities of the electrons and ions. In *Equ. 2.35 & 2.36* C denotes the capacitance per unit length and V the applied voltage. A is the wire radius. *Fig. 2.16* shows the number of created ion pairs as a function of the applied voltage V of a single wire proportional counter. The typical areas of gas amplification are distinguishable.

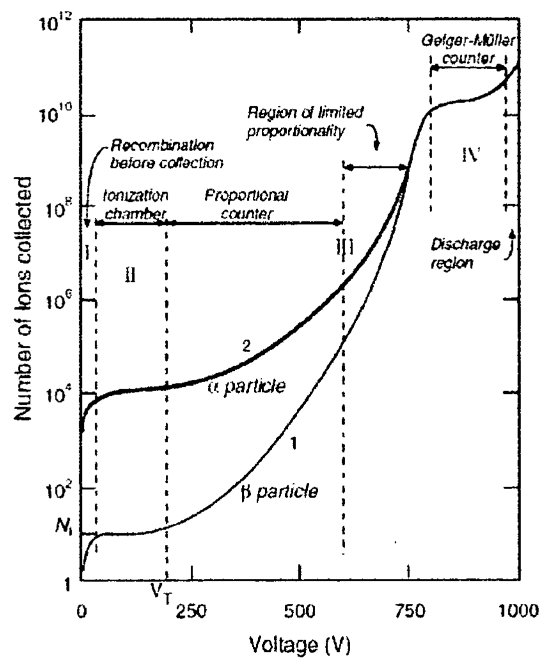

Fig. 2.16: Charge multiplication in dependence of the applied voltage in a SWPC [29].

Proportional Area

A GEM gas detector works in the proportional area. The multiplication is proportional to the ion pairs existing before amplification. If n electrons move along a path dx, dn new electrons have been created.

$$dn = n\alpha\left(\frac{E}{P}\right)dx \qquad \textbf{(Equ. 2.37)}$$

α is the first Townsend coefficient. Values of α/P are given in *Fig. 2.17* as a function of the electron energy. After a mean free path α^{-1} one electron – ion pair is going to be produced. Therefore after a path x-x_0 n electrons are created. In the case of a non-uniform field $\alpha=\alpha(x)$ and the gain M (multiplication factor) is given by:

$$M = \frac{n}{n_0} = e^{\int_{x_0}^{x}\alpha(x')dx'} \qquad \textbf{(Equ. 2.38).}$$

The knowledge of the dependence of the Townsend coefficient on the electrical field allows the computation of M for any geometry. Approximation models can be found in [40].

Geiger-Mueller Area

In this area the proportionality between the created ion pairs and the number of primary and secondary electrons is not valid any more. Ultra-violet photons produced in the multiplication processes induce avalanches that spread over the whole detector volume. The huge space charge within the detector leads to a deformation and reduction of the electrical field.

Discharge Area

A phenomenological limit for the multiplication before breakdown is given by the Raether condition *(Equ. 2.39)*.

$$\int \alpha(x)dx < 20 \qquad \textbf{(Equ. 2.39)}$$

This corresponds to a gain M of about 10^8. Due to the statistical distribution of the energy, and in this way of M, it is advisable to avoid gains higher than 10^6.

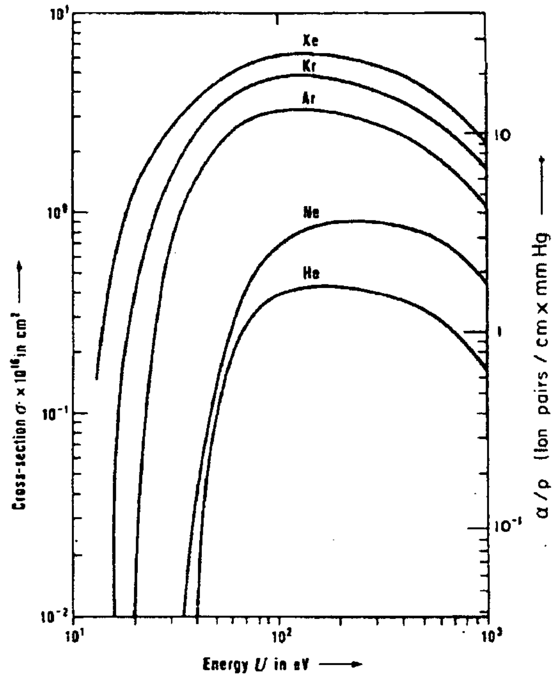

Fig. 2.17: Cross section and first Townsend coefficient for noble gases as a function of the electron energy (right) [41].

Chapter 3

A GEM Gaseous Detector

A standard GEM detector is a parallel plate detector, which contains one or more GEM-foils, a drift cathode and an anode (e.g. *printed circuit board* – PCB) for readout of the amplified charge avalanches in a confined gas tight box. *Fig. 3.1* shows the components of a *single*-GEM detector.

In this chapter the design of the constructed prototype GEM-detectors, the basic operation principles of the gas electron multiplier itself and other important aspects of operation will be discussed.

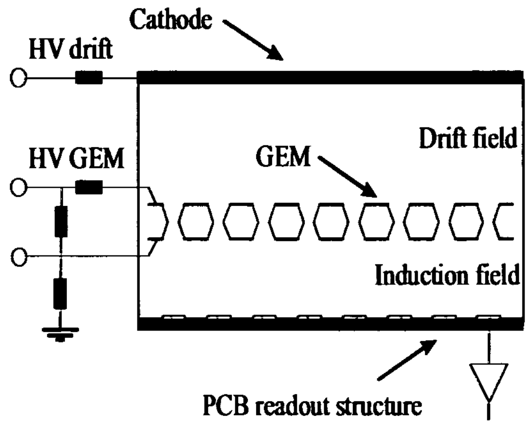

Fig. 3.1: Schematic view of a single-GEM detector.

3.1 Gas Electron Multiplier

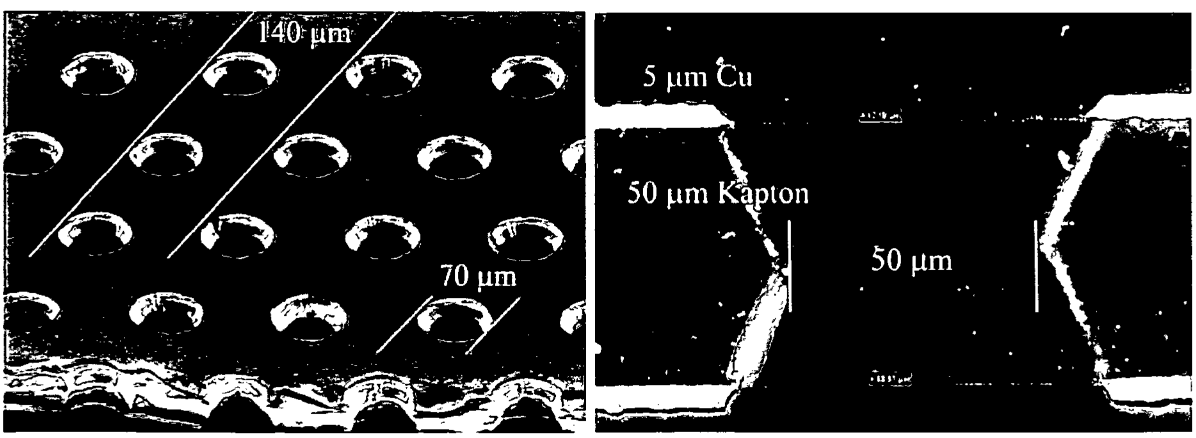

Fig. 3.2: Electron microscope photograph of the copper-clad surface of a GEM-foil (left); (right) cross section of a double conical-shaped GEM-hole; 5 µm of copper on top and bottom of the 50 µm Kapton foil, (hole pitch 140 µm / outer hole diameter 70 µm / inner hole diameter 50 µm) [50].

The *Gas Electron Multiplier* (GEM) was first introduced by F. Sauli (CERN/Geneva) in 1996 [22]. It is made of a thin insulating foil, metal-coated on each side and perforated by a high density of holes (typically ~ 50-100 p. mm^2), as visible in *Fig. 3.2 (left)*. GEMs are generally made of 50 μm thick Kapton foils, both sides evaporated with a 5 –15 μm copper layer. The holes are etched chemically in a photolithographic process]. The double conical-hole structure *(Fig. 3.2, right)* is achieved by etching simultaneously the two sides of the GEM. Improvements in the manufacturing process and an intensive research for an optimized performance led to the development of the so-called standard geometry: a GEM with double conical-shaped holes, a hole-pitch of 140 μm and an outer hole-diameter of 70 μm [47]. Depending on the production method other geometries are also possible. Conical shapes, where the diameter decreases constantly over the thickness of the GEM, and a cylindrical shape, where no change of the diameter of the GEM-hole is desired. More about the different gain behavior, voltage stability and transparencies can be found in [47][48].

A detailed description of the fabrication process can be found in [48]. The production technique of GEM foils was invented by the printed circuit workshop of CERN [49]. In fact, the production of a PCB is similar to the manufacturing procedure of gas electron multiplier.

3.2 Operating Principles of GEM-foils

On the application of a potential difference (typically 350 – 450V) between the two copper electrodes an electric dipole field is generated in the GEM holes. Incorporating the GEM foil into an external electrical field, the field lines are focused into the holes. *Fig. 3.3 (right)* presents the field map of a GEM-foil operated at a potential difference ΔV=500V, with drift and induction fields of 2 and 6kV/cm.

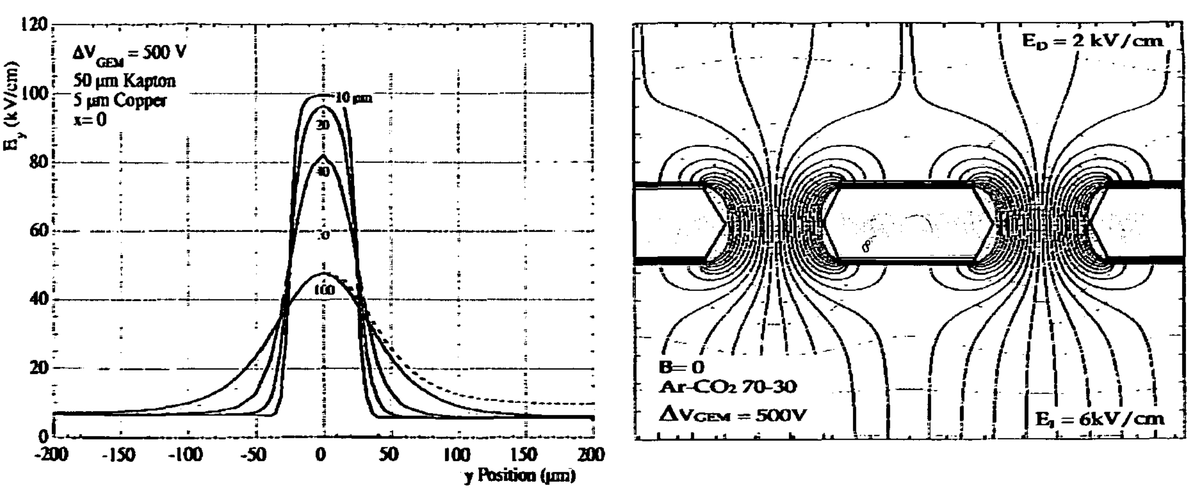

Fig. 3.3: Strength of the electrical field in the GEM-hole, the y position is perpendicular to the GEM-foil and the external fields are symmetric (left); simulated field map of a double-conical standard GEM with asymmetric external electrical fields (right) [47].

Electrons released in the upper drift region by ionization of radiation move along the field lines into the GEM-holes. Due the high electrical field *(Fig. 3.3, left)* the electrons acquire enough energy for further ionization and multiply in a gas avalanche *(Fig. 3.4)*. Each GEM-hole works as an individual proportional counter. A field dependent fraction of the electron charge is collected by the bottom of the GEM electrode, whereas the ions are collected on the top of the electrode. *Fig. 3.3* shows for several holes diameters the computed strength of the electrical field in the GEM-hole. The whole charge multiplication process is determined by three parameters: the charge collection into the holes, the amplification in the holes and the transfer of the amplified charge out of the holes.

$$G = \frac{number\, of\, electrons\, leaving\, gas\, amplification}{number\, of\, electrons\, reaching\, gas\, amplification} \qquad \textbf{(Equ. 3.1)}$$

The gain G of one GEM-stage is the factor by which the number of electrons is increased by gas multiplication inside the GEM-channels. Due to the fact, that not all of the amplified charge reaches the anode, one has to distinguish between real gain G and "effective" gain M, which can be calculated *(according to Fig. 3.4)* by the ratio of the charge arriving at the anode n_{anode} and the charge from the primary and secondary ionization n_{tot} in the drift field *(Equ. 3.2)*. If the dependence of the effective gain M on the GEM-voltage is known, the GEM detector is fully characterized.

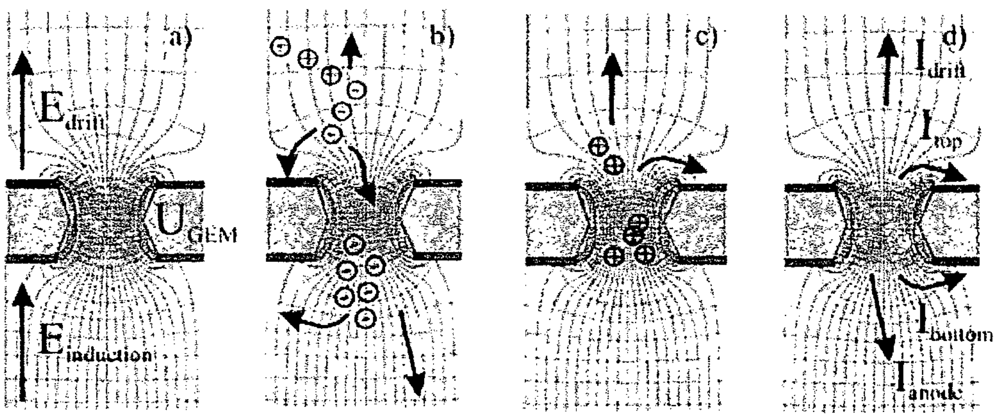

Fig. 3.4: Schematics and field lines of a standard GEM; notation of the electrical fields (a), movement of the primary electrons-ion pairs created in the drift field in the presence of a GEM-foil (b), movement of the ions after amplification (c), origin of the currents on a single GEM-foil (d).

The correlation between the real and the effective gain is given by *Equ. 3.2*. t_{el} is the electrical transparency of the GEM-foil and ε_{col} is the collection efficiency. The parameters in *Equ. 3.2* are defined in *Equ. 3.3 & Equ. 3.4*.

$$M = t_{el} G \varepsilon_{col} = \frac{I_{anode}}{I_{ionization}} = \frac{n_{anode}}{n_{tot}} \qquad \textbf{(Equ. 3.2).}$$

$$t_{el} = \frac{number\, of\, electrons\, reaching\, gas\, amplification}{number\, of\, entering\, the\, GEM - stage} \qquad \textbf{(Equ. 3.3)}$$

$$\varepsilon_{col} = \frac{number\, of\, electrons\, leaving\, the\, GEM - stage}{number\, of\, leaving\, gas\, amplification} \qquad \textbf{(Equ. 3.4)}$$

3.2.1 Drift field

The ratio of the charge reaching the amplification region to the total charge arriving at the GEM is defined as electrical transparency. As indicated in *Fig. 3.4* the drift field is applied between the cathode and the top of the first GEM. Depending on the strength of the drift field the field lines go through the holes or terminate on the copper layer. For a fixed GEM voltage and a suitable induction field, the t_{el} increases, when the drift field is enhanced. At a certain value a plateau is reached. At too high drift fields a certain fraction of field lines end on the copper surface, this means electrons following these lines are lost and the t_{el} decreases. A set of detailed measurements of transparency curves can be found in [47]. Whereas the optical transparency of a standard GEM foil is about 23%, the electrical transparency in vacuum comes close to unity. In the gas t_{el} is smaller due to the diffusion losses inside the holes and the statistical process of the gas amplification, which leads to a deflection of electrons from their ideal way through the holes in the vacuum.

3.2.2 GEM voltage

The transparency is obviously also dependent on the potential difference applied on the GEM. A higher GEM voltage leads to a higher real gain. The higher the GEM voltage, the more electrons are lead into the holes. At a constant drift field the point of a decreasing t_{el} *(as mentioned in 3.2.2)* is shifted to higher values. *Fig. 3.5 (left)* shows the electron (ion) transmission, which is an overlap of the electrical transparency and the gain. In the low field region it represents the electrical transparency of the GEM. Also visible the transparency plateau of I_A, until at about 100V the gas amplification of the GEM starts. In *Fig. 3.5 (right)* effective gain values for a single GEM-stage (SGEM) can be found. The multiplied charge after one GEM-stage can be further increased by an adjacent second and third GEM-stage (double and triple GEM, *see Fig. 3.6*). Therefore higher effective gains are reachable.

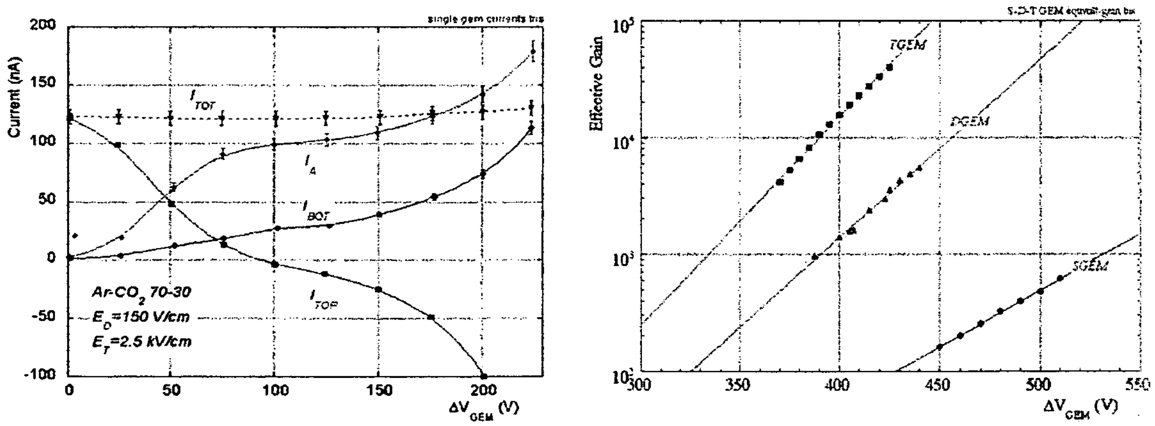

Fig. 3.5: Currents measured on various electrodes under uniform radiation as a function of the GEM voltage (see Fig. 4d) (left). the current from the drift electrode (dashed line) is deduced from charge conservation [51]; effective gain of multi-GEM structures (right) (SGEM: single-GEM, DGEM: double-GEM, TGEM: triple-GEM) [47].

3.2.3 Induction field

The induction or collection field is applied between the PCB (anode) and the bottom of the last GEM *(Fig. 3.4a)*. Increasing the induction field leads to an increase of the charge (or current), which can be read out at the anode. Moreover, the fraction of the charge, which is lost on the bottom of the last GEM is reduced. The fraction of the charge, that reaches the anode and the total charge, which has left the GEM-hole is called collection efficiency. Typical values for the induction field are in the range of 3 to 5kV/cm. At higher electrical fields the electrical force may bend the GEM-foil, which leads to a different gain behavior or even to a contact with the anode.

3.3 Prototype Detector

The simplest type of a GEM detector, the single-GEM detector, is shown in *Fig. 3.1.* It consists of a drift cathode, a GEM and a readout structure. To power the drift cathode and the GEM a simple resistor network can be used *(Fig. 3.1 & Fig. 3.6)*. Depending on the applied voltage difference gains up to ~ 10^3 can be reached with a single-GEM *(see Fig. 3.5, right)*. In order to detect the small number of electrons released by a MIP (minimum ionizing particle) or even single photoelectrons higher gains are necessary. By cascading several GEM-foils *(as indicated in Fig. 3.6)* the electrons released from the first GEM are also multiplied by the following GEM-foils. The amplification process is the same as in the case of one single foil. The process is not changed by the presence of more GEM-foils. The cascaded device permits higher gains at lower working voltages.

Fig. 3.6 shows the schematic view of a triple-GEM detector. *Fig. 3.5 (right)* shows typical gain curves for single, double and triple-GEM-detectors. Increasing the transfer fields extracts more electrons from the first GEM. At transfer fields higher than 3.5kV/cm the transparency of the second GEM decreases. Electrons coming from the amplification region terminate on the upper side of the 2nd GEM and the anode current gets smaller.

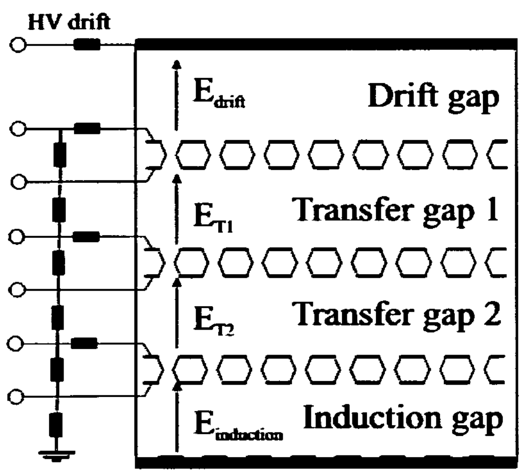

Fig. 3.6: Schematic illustration of a triple-GEM detector; also visible the protection resistors (typically 10 MOhm) in front of the GEMs and the voltage divider for powering the GEMs; the field gaps are typically 1-3mm.

Moreover, inserting further amplification stages reduces the discharge probability and prevents the detector from destructive sparks [52]. The alignment of the GEM-foils with respect to the hole-pattern is not relevant, as the diffusion of the electron clouds between two GEMs is in the order of millimeters. The avalanche coming out of one GEM-hole is spread over holes of the next GEM and the number of collected electrons is determined by the collection efficiency of the 2nd GEM [54].

Triple-GEM detectors with GEMs of different designs are used at the moment in the experiments TOTEM [56][57], MICE [55] and COMPASS [23] at CERN.

All the measurements presented in this thesis were performed with special prototype-detectors.

The advantages of such a detector are robustness and flexibility. *Fig. 3.8* shows a photograph of the inside of this detector. It supports GEM-foils with an active area of 10 x 10 cm^2 and suitable readout structures. Such a setup allows a variation of the number of the GEM-foils, the gap size and the powering scheme. Around the readout structure a Stesalite-frame is glued. Below this frame high voltage connections for the powering of the GEM-foils and the drift field are glued to the support. Additionally a gas inlet is foreseen. A suitable cap with the gas outlet and an exchangeable entrance window (Quartz, Kapton or Mylar) can be put on the bottom frame to close the detector. Gas tightness is provided by O-rings between the frame and the cap. The GEM-foils and the drift cathode are mounted on frames with four drilled holes in the corners of the frame *(Fig. 3.7)*.

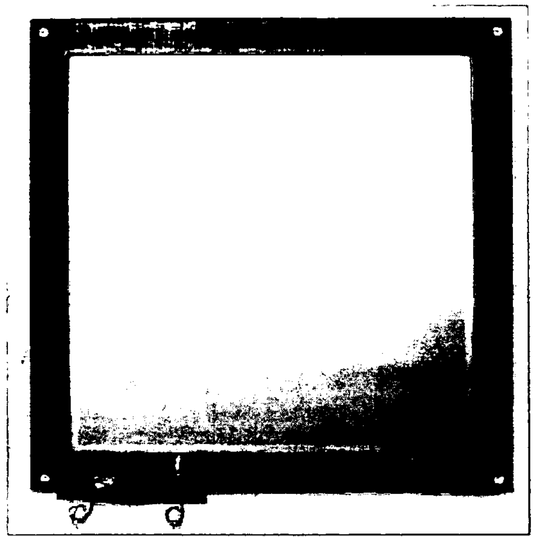

Fig. 3.7: Photograph of a framed 10 x 10 cm^2 non-segmented GEM with four holes in each corner of the frame to mount it into the prototype detector. The wires are soldered to the top and to the bottom of the GEM-foil to provide the HV contact.

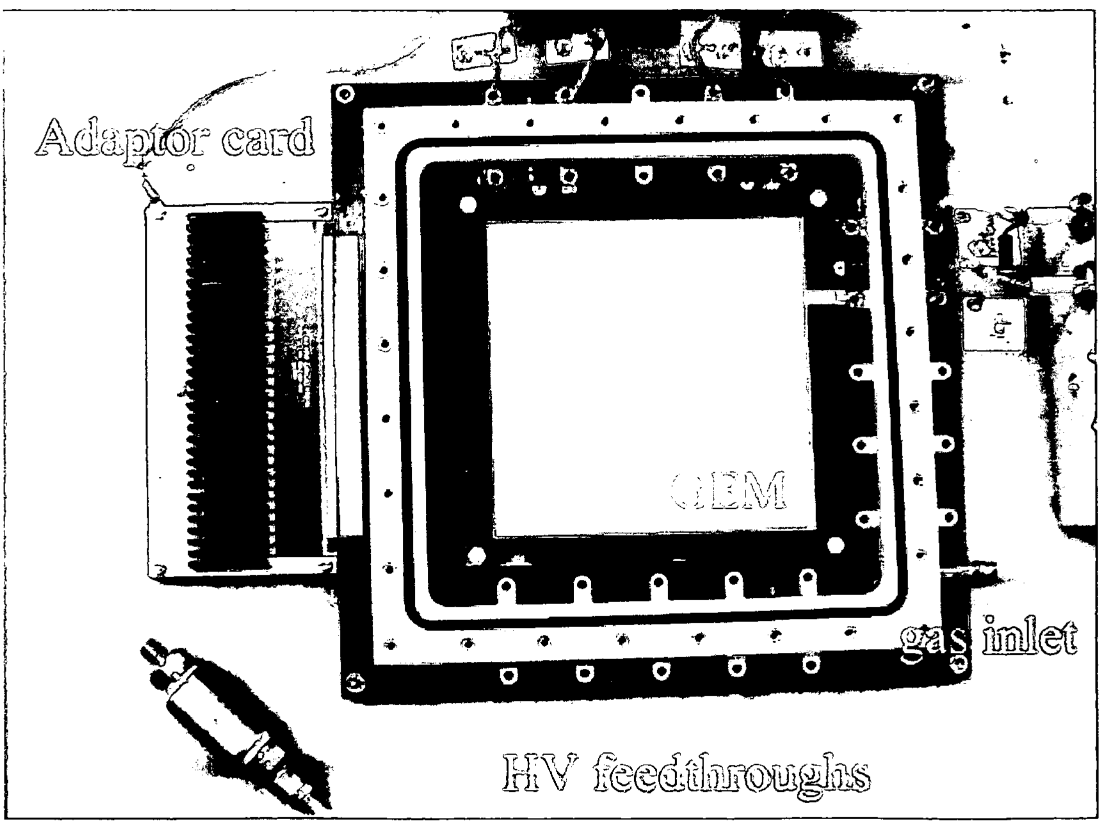

Fig. 3.8: View of the used prototype detector. Mounted with three framed 10 x 10 cm^2 GEMs; wire bonds connect the readout strips of the PCB with a 512 channel adaptor card (200μm pitch).

Teflon-pins are screwed into the readout structure. The GEM-foils and the drift cathode are fixed on these pins by Teflon-screws. *Fig. 3.8* & *Fig. 3.9* show the proper alignment. Teflon-washers are used to provide the constant gaps between the GEM-foils.

The readout is provided by strips, which are wire-bonded to an adaptor card (200μm pitch). The bonding has been performed by the PH-DT2 bonding laboratory.

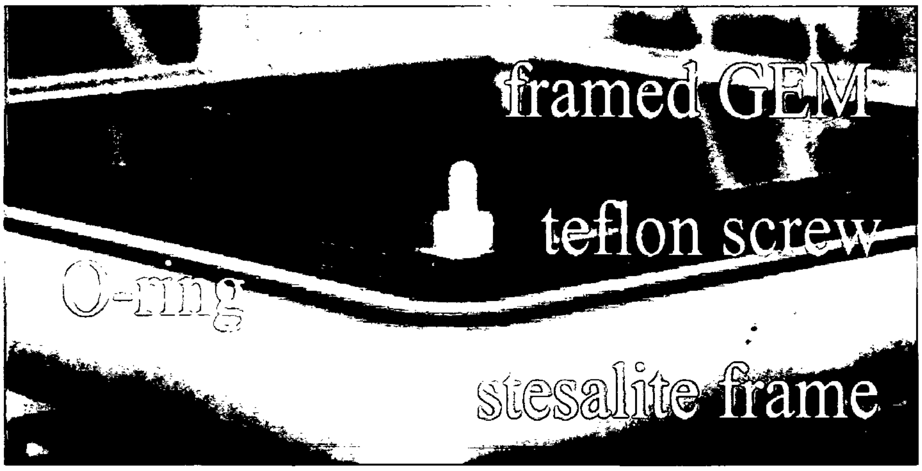

Fig. 3.9: Inside the detector: the framed GEM-foils are fixed with Teflon screws to the PCB; the GEMs are separated by Teflon-spacers. The Teflon pins are screwed into the PCB.

3.4 Calibration Issues

A common method to measure the effective gain is the measurement of the electron signal current I_S on the PCB electrode. The detector is exposed to a radiation source with a constant flux R=dN/dt (5.9keV Fe^{55} source or 9keV X-ray gun).

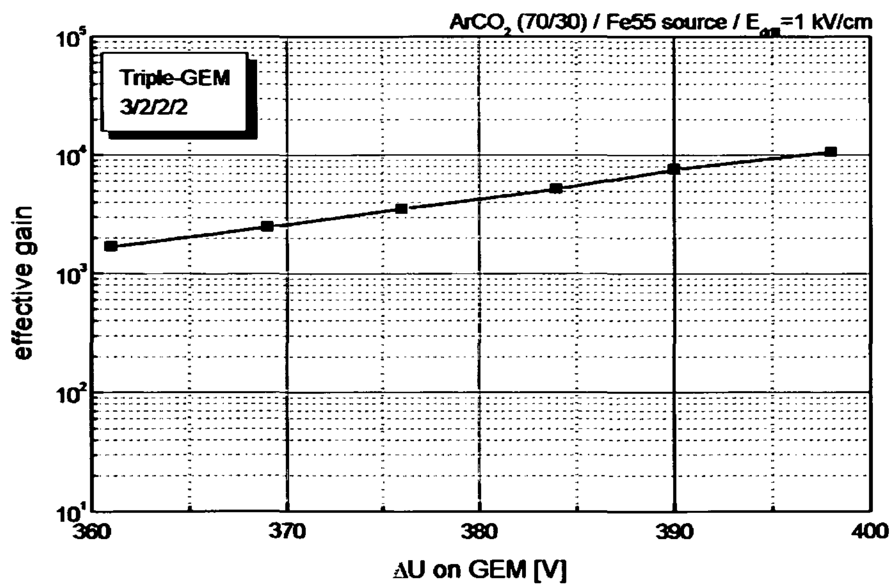

Fig. 3.10: Dependence of the effective gain on the average voltage of the three GEMs; the numbers on the left refer to the distances between the GEM foils.

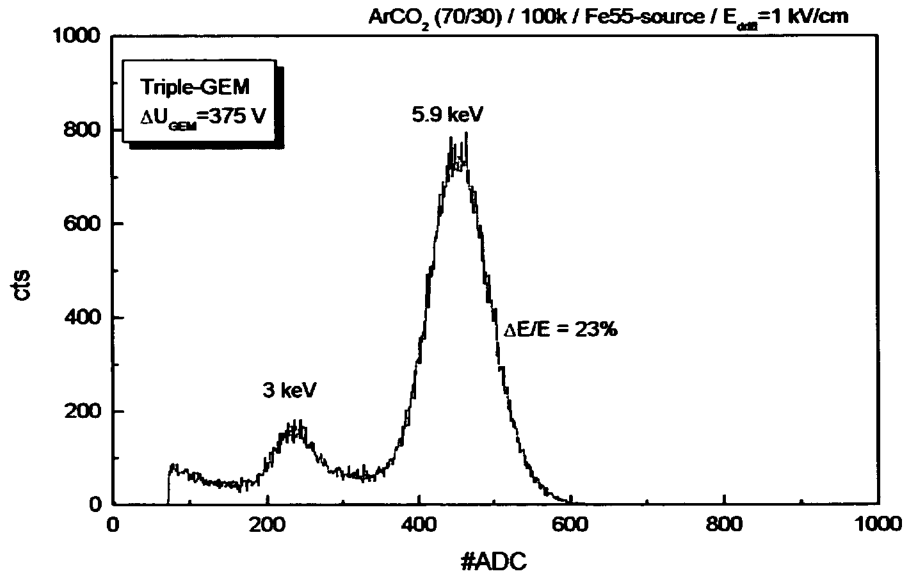

Fig. 3.11: A typical Fe^{55} pulse height spectrum obtained with a triple-GEM detector; the Argon escape peak (3keV) is well distinguishable from the main peak (5.9keV). For details see Appendix A. The energy resolution ΔE/E is 23%.

For the calibration of the detector several anode strips are connected together and the current I_S is measured by the voltage drop over a resistor of 1 MΩ. The number of the strips should be large enough to cover the whole charge clusters, which can be checked easily by moving the source. The measured current should be constant within the scanned detector area.

$$M = \frac{n_{anode}}{n_{tot}} = \frac{I_S}{n_{tot} Re} \quad \textbf{(Equ. 3.5)}$$

Following the composition rule *(Equ. 2.6)* the total number of ion pairs n_{tot} per conversion (~220 for 5.9keV) is created in the drift layer in $ArCO_2$ (70:30). Replacing the voltmeter by a charge sensitive preamplifier (ORTEC142LH) and connecting it with a ORTEC 450 Research Amplifier [53] allows to record the signals induced on the readout strips. The output of the research amplifier is connected to a discriminator. If the rectangular discriminator signal is connected to a counting unit (e.g.: CAEN Quad Scaler Mod. 145) [58] the rate can be measured. The effective gain then is given by *Equ. 3.5* where e is the electron charge. By systematically increasing the voltage on the GEMs the gain curve can be obtained. *Fig. 3.10* shows a typical gain curve of a triple GEM detector used in the experiment presented in *Chapter 5*.

The pulse height analysis of the induced signals allows also a determination of the effective gain of the gas detector. The induced signals together with the discriminator signals are sent into an analogue-to-digital converter (LRS 2259). A controller interface (CAEN Mod. 111) connects the ADC with a proper DAQ. A program written for this purpose records the pulse height spectrum *(Fig. 3.11)*.

The signal on the anode is induced by the moving charges from the last GEM. A similar signal with opposite polarity can be observed on the bottom of the GEM-foil (corresponding to the current in *Fig. 3.4d*). By connecting a capacitance of (e.g. 150 pF) to the bottom of the 3rd GEM, the pulse height spectrum of this signal can be obtained in the same way mentioned above. Therefore the stability of the gain and the energy resolution of the detector can be monitored constantly. Moreover, this induced signal can be used to trigger the readout electronics, which can be connected to the anode strips. *Fig. 3.12* shows the set-up of such a measurement. In the case of a calibration measurement the pre-amplifier has to be replaced by a voltmeter.

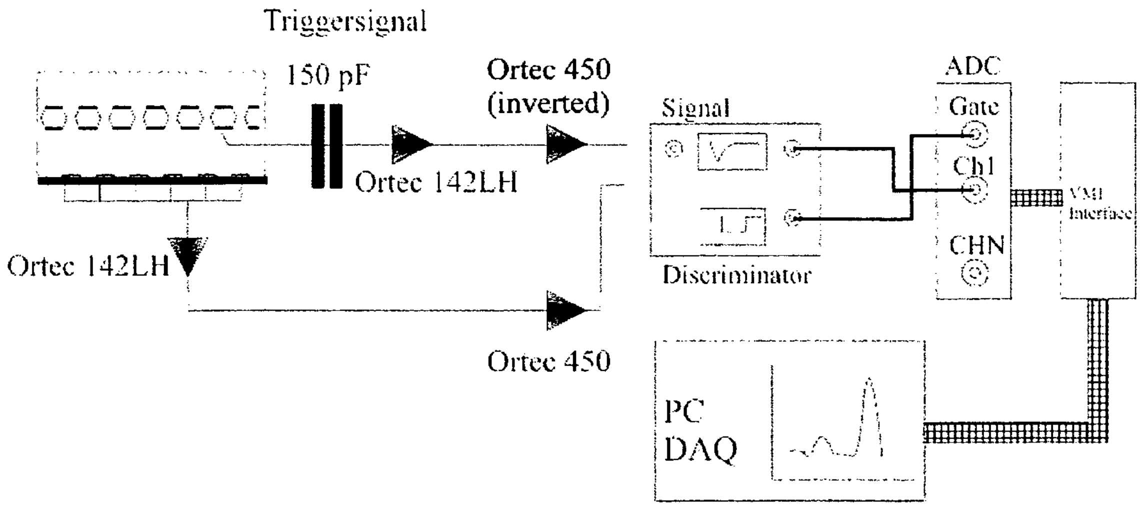

Fig. 3.12: Set-up for the calibration measurements and the permanent monitoring of the pulse height spectra, when the detector is constantly irradiated.

3.5 Operation of the Detector

In order to localize and detect particles efficiently a stable and homogenous gain over a long operation period is necessary. The quality of the GEM-foils, the cleanness and reliability of the counter gas are essential. The mounting of the GEMs into the detector has to be done in a clean room under dry and clean conditions. Only in this way a proper operation is achievable.

3.5.1 Testing of a GEM

Before the final assembly of a GEM-foil into a detector, the foil has to pass several tests. In the printed circuit workshop the resistance between the two copper sides is measured. In air it has to exceed 2 GOhm. In order to avoid fingerprints or saliva droplets on the surface gloves and masks have to be used during any handling of a GEM. Before and after the framing procedure the leakage current is measured. It has to be below 5 nA@500V (R>100GOhm) in air, in fact in most of the cases the leakage current is not measurable anymore (smaller than 1 nA@500V). Of course, also the sensitive surface has to be checked, whether it has been offended during the production- and test procedures.

3.5.2 Gas System

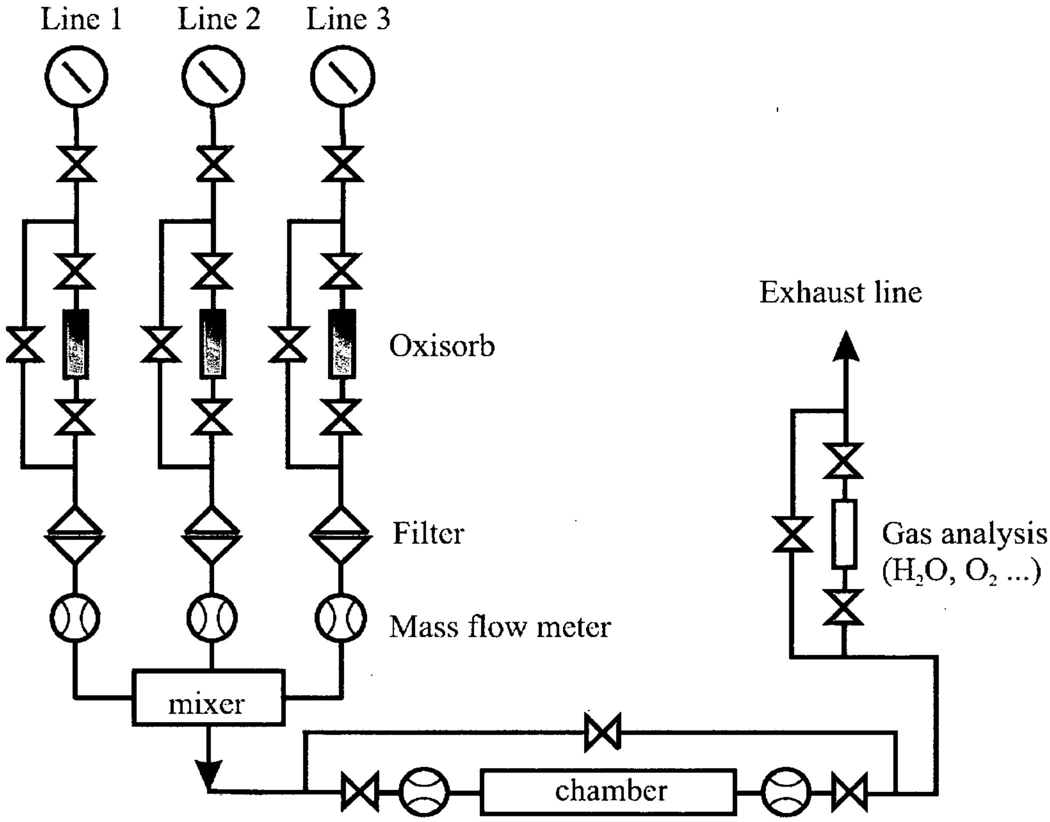

Fig. 3.13: Schematics of the gas distribution system.

In order to provide a proper operation of the gas detector it is absolutely necessary to keep the whole gas system free from any small dust and metallic particles. Gas filters are used to keep the counter gas clean. All the gas pipelines and the gas distribution system are made of stainless steel tubes. The gas racks are equipped with calibrated mass-flow meters regulating the flow electronically. In that way gas mixtures can be produced. Bubblers are not used to avoid any pollution of the chamber due to back diffusion. The gas storage is outside the laboratory. Pressure reducers decrease the gas pressure down to 1 bar. At this pressure the gas flows into gas lines *(Fig. 3.13)*.

In addition flow meters in front of and behind the detector are advisable to control the gas tightness of the detector and monitor the gas flow. A gas flow of about 30 cc/min is sufficient to guarantee a proper gas exchange in the prototype detectors. Sometimes it is important to prevent a chamber from being flushed with air, e.g. during a gas exchange. This is achieved by installing a bypass pipeline. The gas analysis system is also bypassed, because the sensitive hygrometer should not be exposed to air.

3.5.3 HV-Powering Scheme

To power the gas detectors the power supply CAEN module N 470 (4 channel programmable) (±3-8kV; I_{max}= 1mA) and CAEN module A 471 (±8kV; I_{max}= 8μA) were used [58].

In the case of discharges a reliable and robust high-voltage powering scheme is necessary. Depending on the measurement and application of the detector an individual powering scheme or a single resistor network can be chosen. In the first case the current is limited only by a large value protection resistor. The electrodes are powered individually. In critical situations the voltage across a GEM can easily exceed values, which can lead to the destruction of the device. A safer solution is the single resistor network. The disadvantage in this case is the almost fixed operation voltages.

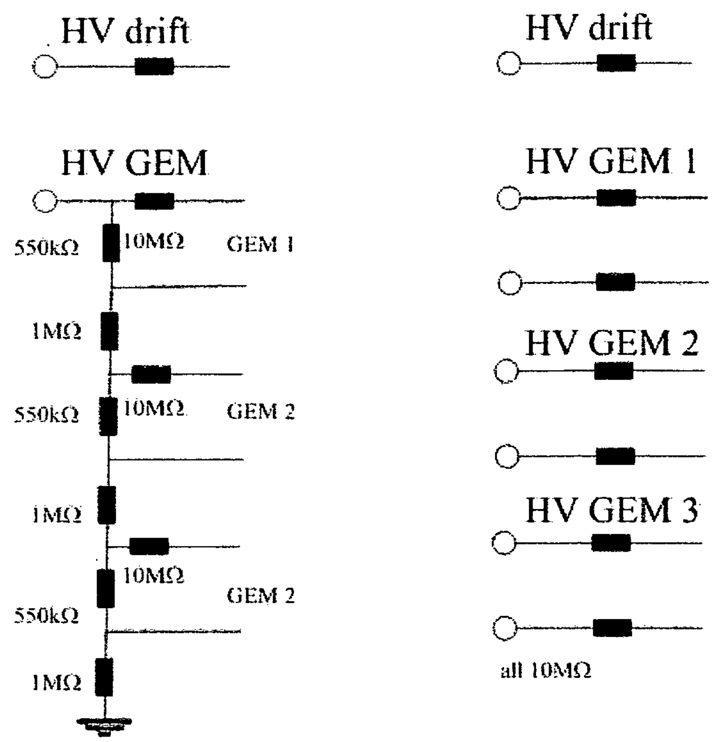

Fig. 3.14: Individual powering scheme (above); single asymmetric resistor network for powering the GEMs, only the drift is powered directly via a protection resistor. GEMs that amplify more charge are operated at a lower voltage to reduce the discharge probability [23].

Chapter 4

A GEM Photocathode

4.1 Introduction

Studies of large area CsI-based wire chambers operating as single photon detector were presented in the late eighties. High quantum efficiency (QE) values were reported [59][60] for CsI and TMAE-coated films in CH_4. A high and stable gain was achieved by the gaseous photomultipliers.

At the same time low cost integrated electronics became available. Hence it was possible to instrument large MWPCs with large areas of pad-segmented cathodes using sensitive low-noise front-end amplifiers. After years of research and development large experiments have adopted the use of CsI RICH (Ring Imaging Cherenkov) detectors; for example, HADES [61], ALICE [62] and COMPASS [63]. A detailed overview about fast RICH detectors can be found in [65].

Fig. 4.1 shows the principle scheme of a large area RICH detector. Due to the interaction of a charged particle with the radiator material *(see Chapter 4.1.1)* photons are emitted.

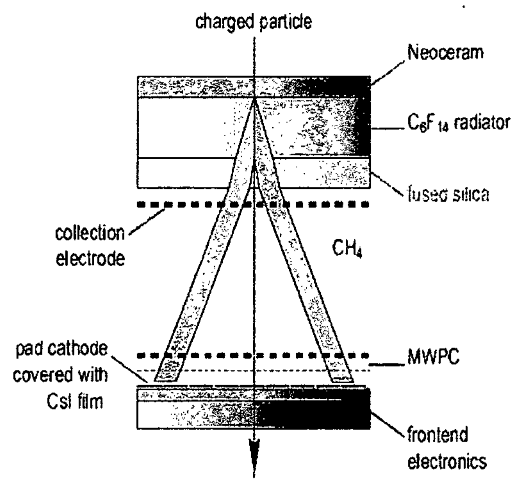

Fig. 4.1: Principle scheme of a large area proximity focusing RICH detector [64].

These UV-photons are converted by a photosensitive material into photoelectrons. The ratio of the number of converted photoelectrons to the number of photons, that have hit the photocathode, is defined as the quantum efficiency. After emission the photoelectrons are multiplied on the wires of a MWPC. The produced avalanches induce a signal on the pad-segmented cathode. The counter gas is pure CH_4, because in this the photoelectron yield is not decreased and it is highly transparent in the UV-range [66][67]. A RICH detector has to locate efficiently and accurately single photoelectrons emitted by the CsI film deposited on the pad cathode. Due to the high multiplicity a detector with multi-photon resolution to reconstruct ambiguity free the multi-photon events is mandatory.

4.1.1 Cherenkov Effect

Cherenkov radiation is emitted, when a fast charged particle transverses a medium with a refractive index $n = n(\lambda)$ and a particle velocity $v = \beta c$, that is greater than the velocity of light in the medium c/n. This occurs due to an asymmetric polarization of the medium in front of and behind the particle [45]. The result is an electrical dipole varying with time. The angle between the emitted photon and the trajectory of the charged particle is called θ_C. During a time t the wave moves the distance tc/n=AC, while the particle has moved in the medium the distance $t\beta c$=AB.

According to *Fig. 4.2* & *Fig. 4.3* the ratio of these two distances defines the Cherenkov angle θ_C.

$$\cos\theta_C = \frac{tc/n}{t\beta c} = \frac{1}{n\beta} \qquad \textbf{(Equ. 4.1)}$$

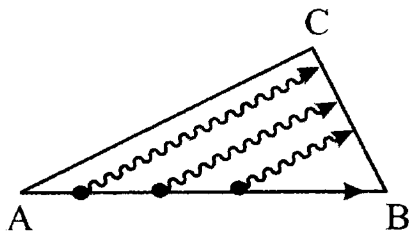

Fig. 4.2: Geometric determination of the Cherenkov angle θ_C.

This correlation between the particle velocity and θ_C allows the determination of β by measuring the radius of the Cherenkov ring *(Fig. 4.3)* mapped on the cathode plane of the MWPC or detected in an array of independent photocathodes(e.g.: HPD). For the emission of Cherenkov photons a threshold exists, β must be greater than 1/n.

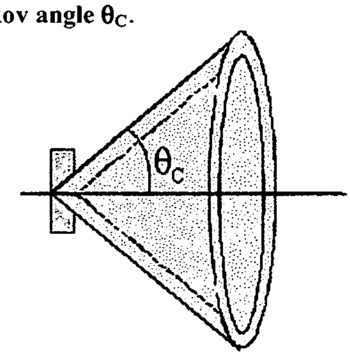

$$\theta_{C,\max} = \arccos\frac{1}{n} \qquad \textbf{(Equ. 4.2)}$$

Fig. 4.3: The Cherenkov photons leave the radiator in a cone with an angle θ_C.

At the threshold θ_C is ~ 0° and the angle increases for higher velocities until a maximum is reached at β=1. Cherenkov radiation can only be produced, if $n(\lambda)>1$ [38].

$$\gamma_{threshold} = \frac{1}{\sqrt{1-\beta^2_{threshold}}} = \frac{1}{\sqrt{1-\frac{1}{n^2}}} \qquad \textbf{(Equ. 4.3)}$$

$$\gamma_{threshold} = \frac{E_{threshold}}{m_0 c^2}$$

The threshold velocity corresponds to threshold energy according to *(Equ. 4.3)*. The Lorentz factor at a fixed energy is dependent on the mass of the particle. Therefore the measurement of Cherenkov radiation is suited for particle identification. The number of emitted photons per unit path length and unit wavelength is given by *Equ. 4.4*.

$$\frac{d^2N}{dx d\lambda} = \frac{2\pi z^2\alpha}{\lambda}\left(1-\frac{1}{\beta^2 n^2}\right) = \frac{2\pi z^2\alpha}{\lambda^2}\sin^2\theta_c \qquad \textbf{(Equ. 4.4)}$$

The factor z is the charge of the incident particle and α is the fine structure constant. The performance of a RICH detector is characterized by *Equ. 4.5* [68]. $N_{photoelectron}$ is the number of Cherenkov photoelectrons, L is the radiator thickness, N_0 is the detector figure of merit. ε_{det} is the single electron efficiency, QE the quantum efficiency and θ_C is the mean Cherenkov angle (established by the traversed media transmissions T_i).

$$N_{photoelectron} = L N_0 \sin^2 \theta_c$$
$$N_0 = 370 \varepsilon_{\det} \int QE(E) \prod_i T_i(E) dE \qquad \textbf{(Equ. 4.5)}$$

The particle identification capabilities are strongly related to the angular resolution of a RICH detector. In order to keep the angular ring resolution *(Equ. 4.6)* small, $N_{photoelectron}$ has to be maximized, whereas the angular resolution per photoelectron $\sigma_{\theta c}$ has to be minimized. $\sigma_{\theta c}$ has some intrinsic contributions as a chromatic and a geometric error. The localization error is related to the precision with which the photon impact coordinates can be measured.

$$\sigma_{\theta_c}{}^{ring} = \frac{\sigma_{\theta_c}}{\sqrt{N_{photoelectron}}} \qquad \textbf{(Equ. 4.6)}$$

This error is determined by the detector characteristics (wire pitch, pad size ...) and by the photon feedback *(Chapter 4.1.4)*. Saturated velocity particles produce 16-18 photoelectrons/ring along their tracks through the 10 mm C_6F_{14} radiatior (n=1.29). The ring radius is between 80 and 120 mm, $\sigma_{\theta c}$ is between 8 and 12 mrad, $\sigma_{\theta c}{}^{ring}$=1.8-2 mrad [69]. The detector parameters in this case are e.g.: pad size: 8 x 8 mm^2, anode-wire pitch: 4 mm and 2 mm anode-pad gap.

4.1.2 The photosensitive material

Ultra-violet photosensitive gases (e.g.: TEA-trithylamine, TMAE-tetratisdimethylaminoethylene) suffer from some crucial disadvantages compared to a solid state CsI thin-film photon converter (e.g.: detectors equipped with TMAE need to be heated due to the low vapour pressure; the long absorption length – 18 mm for a photon with λ=70nm at T=28°C and 1 atm, the slowness due to the long photoelectron drift [70]). The QE-values reached with CsI photocathodes were comparable with those of other devices based on saturated TMAE vapors in CH_4 in the UV region (35%@7.5eV).

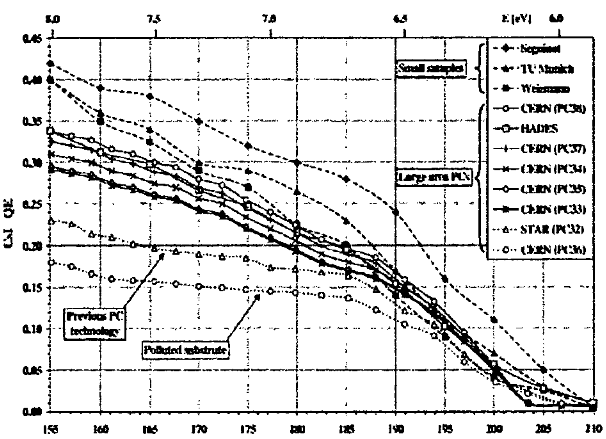

Fig. 4.4: CsI quantum efficiencies from several groups, obtained from small samples (dashed lines) or from large area photocathodes. (threshold of CsI is 210 nm) [71].

Further results proved the feasibility, the reproducibility and the working power of large area CsI photocathode technology [72]. CsI is hygroscopic, therefore an exposure to gases with high humidity (e.g.: air) has to be avoided, otherwise the layer deteriorates and the QE decreases. An advisable upper limit for counter or storing gases is about 10 ppm of H_2O. *Fig. 4.4* shows the quantum efficiencies from R&D results (dashed lines) together with some large area (64 x 60 cm^2) photocathodes produced by ALICE HMPID-group. CsI-coated photocathodes can be produced with high and reproducible quantum efficiencies [73].

4.1.3 The single photon pulse height spectrum

According to *Equ. 2.33*, the average avalanche gain M in a homogenous electrical field is given by *Equ. 4.7*. n is the average avalanche size and α the number of ionizing collisions per unit length (Townsend coefficient).

$$M = \frac{n}{n_0} = e^{\alpha x} \qquad \textbf{(Equ. 4.7).}$$

P(k,x) is the probability that the avalanche consists of k electrons after a path x. The probability P(1,x) that there is no ionizing collision after a path x is:

$$P(1,x) = e^{-\alpha x} \qquad \textbf{(Equ. 4.8).}$$

In order to obtain two electrons after a collision within a distance x, the probability yields to *Equ. 4.9*.

$$P(2,x) = e^{-\alpha x}\left(1 - e^{-\alpha x}\right) \qquad \textbf{(Equ. 4.9)}$$

The probability to have k electrons after a path x is given by *Equ. 4.10*.

$$P(k,x) = e^{-\alpha x}\left(1 - e^{-\alpha x}\right)^{k-1} \qquad \textbf{(Equ. 4.10)}$$

Combing *Equ. 4.10* with *Equ. 4.7* and setting n_0=1, an avalanche has always to start with one electron, leads to *Equ. 4.11*. The approximation made in *Equ. 4.11*, is known as Furry's law. It is valid for n>>1.

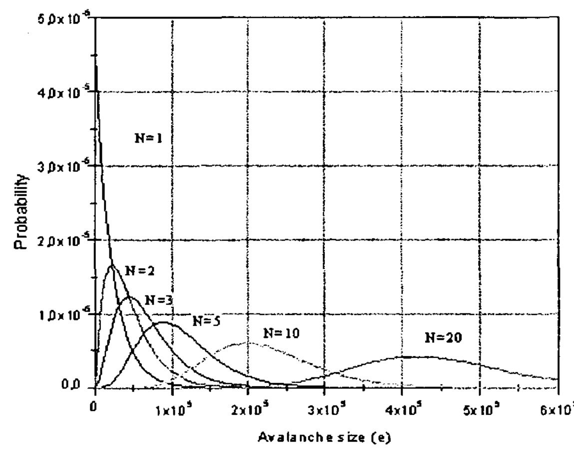

Fig. 4.5: Avalanche size probability distributions for increasing values of N.

As can be seen the probability decreases exponentially and furthermore it has a maximum at k=1. Therefore for electrons it is most probable not to multiply. Both the mean and the variance are equal to the average avalanche size n.

$$P(k,x) = \frac{1}{n}\left(1 - \frac{1}{n}\right)^{k-1} \approx \frac{e^{-\frac{k}{n}}}{n} \qquad \textbf{(Equ. 4.11)}$$

To get the avalanche size distribution for an avalanche starting with N electrons, N independent exponentials must be convoluted [74].

$$P(k,N) = \frac{1}{n}\left(\frac{k}{n}\right)^{N-1}\frac{e^{-\frac{k}{n}}}{(N-1)!} \qquad \textbf{(Equ. 4.12)}$$

For N=1 *Equ. 4.12* reduces to *Equ. 4.11*. *Equ. 4.12* is identical to a Poisson distribution in k/n. *Fig. 4.5* shows the computed avalanche size distribution for several numbers of primary electrons. As stated before, for a larger number of primaries (>20) the distribution becomes of a Gaussian shape. The center of this bell-shaped curve is around the average total charge $Ne^{\alpha x}$. The distribution starting with one single electron is of an exponential shape.

4.1.4 The problems of RICH counters coupled to MWPC

In the case of single electrons, very small signals have the highest probability of being generated owing to the expected exponential pulse-height distribution, the small avalanche size, and the loss due to anode/cathode coupling. An increase of the chamber gain is mainly limited due to the photon feedback. Excitations in the avalanche process lead to the isotropic emission of photons in the counter gas. Their number depends on the gas and the total avalanche charge. In the case of single electrons, the total avalanche charge is equivalent to the chamber gain. If these feedback photons hit the CsI layer photoelectrons are emitted, too. Such a feedback can diverge at higher gains and it causes an increase of the background uncorrelated to the Cherenkov events.

Another gain limitation is related to aging process of the CsI layer. The main source of degradation (if long term exposure to air is avoided) is the impact of the ion clouds produced in the gas amplification process [69][75]. The higher the gain the larger is the ion bombardment on photocathode and the stronger is the deterioration process. Decreasing the distance between anode and cathode to maximize their coupling would lead to an enhancement of the pad signal amplitude at a given gas gain. This leads to technical problems in the stability and feasibility of large area chambers. Large integrating times (compatible with the expected event rates) of the FE pad electronics also increase the signal amplitude For example, in the ALICE HMPID experiment an integrating constant of >700ns is chosen, which is sufficient to get enough signal induced on the pads. At interaction rates of 100 kHz (ALICE proton mode) and a few kHz in the lead mode efficient single electron detection is guaranteed [64]. Due to the low operation rate the use of low cost analog multiplexed readout electronics is possible and it allows an accurate localization by using the charge centroid determination (equal to the method of center of gravity). The smaller the pad size the more accuracy can be achieved in the centroid finding process and a too small pad size affects the detection efficiency in a negative way. A compromise between the localization accuracy and the price for electronics has to be found.

4.2 Experimental Setup

The triple-GEM detector used for these measurements is described in *Chapter 3.* The first copper standard 10 x 10 cm^2 GEM has been replaced by a gold-plated one. On top of the gold surface a 300 nm photosensitive layer of CsI is deposited (*Fig.* 4.6). The vacuum evaporation process is described in [73]. It has been developed at CERN (PH-DT2). The change from copper to a gold-plated surface has chemical reasons. The photon sensitive material interacts with the copper promoting its dissociation [76].

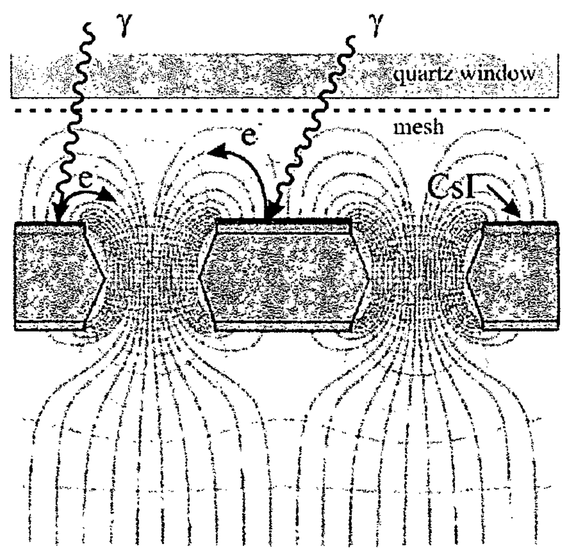

Fig. 4.6 (right): Schematics and field lines of the first gold plated GEM; on top 300 nm of CsI are deposited serving as a reflective photocathode.

With a gold substrate the best performance is achieved. In this setup the quantum efficiency could not be verified directly, but the workshop has a large experience in coating large area devices concerning an optimization of the quantum efficiency [64][77].

The detector front cap consists of a 5 cm diameter UV quality quartz window clued into a Stesalite frame. Therefore the central part of the detector can be irradiated by ultraviolet photons emitted from a low-pressure hydrogen flash lamp *(see Chapter 4.2.1)*. The transmission curve of the quartz window is shown in *Fig. 4.7*. Additionally four polymer-covered openings are foreseen in the cap allowing an exposure to X-rays for calibration purposes. The electrode providing the drift field is made with a thin mesh (90 % optical transparency). The transfer and induction gaps are 2 mm thick with a 3 mm drift region. Below the triple-GEM device for charge multiplication the detector has a projective parallel strip readout on the anode. Charge signals are recorded on eight adjacent readout strips. The strip pitch is 200 µm. An adjustable collimator *(Fig. 4.13)* in front of the detector defines the size of the beam. A set of fine wire meshes put between the detector and the UV-source allows the variation of the beam intensities.

Before CsI evaporation the contact wires for powering the GEM were soldered to the contacts. The CsI-coated GEM was handled in air only during the transfer from the evaporation vessel to a closable gas tight transportation box. After the evaporation in the stainless steel box the GEM was tested again. During test and storage the GEM was constantly flushed by nitrogen. All care was taken to avoid prolonged air exposure. The counter gases are $ArCH_4$ (90/10) and pure CH_4. The CsI quantum efficiency threshold is 5.9 eV *(Fig. 4.4)*,the cutoff energy of the quartz window *(Fig. 4.7)* is 7.5 eV.

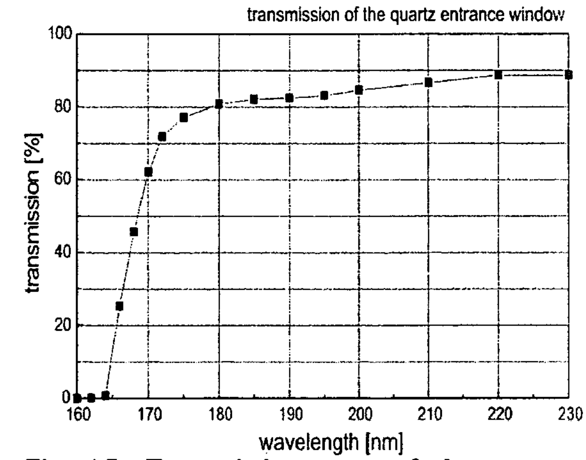

Fig. 4.7: Transmission curve of the entrance window clued into the front cap of the detector (cutoff: ~165 nm or 7.5 eV).

Both gases are transparent in this energy range. The noble gas mixture offers the advantage of operating the detector at a lower voltage. Whereas pure noble gases show a quantum efficiency decrease due to electron backscattering, noble gas mixtures do not show this behavior [67]. The triple GEM detector is powered by a symmetric voltage divider. The voltages across the GEMs are 515 V and the strength of the electrical fields in the induction and transfer gaps are 4.6 kV/cm. The drift field is inverted (- 60V/cm) to exclude events in which the photons are ionized in the drift region. The uniformity of the gain and the linearity of the response are calibrated by using an external X-ray source.

4.2.1 UV source

As an ultraviolet photon source the relaxation discharges in a sealed vessel containing low-pressure hydrogen is used. The beam exit window is made of CaF_2. Energy and frequency of the discharges can be controlled by external circuitry. The schematics of the hydrogen lamp can be seen in *Fig. 4.8*. By changing the resistance (from 300 to 1000 MΩ) the frequency of the discharges can be controlled. A modification of the capacitance (typical between 1 and 50 pF) leads to a change of the energy. A capacitive pickup on the lamp provides the discharge time, used for measurements in coincidence.

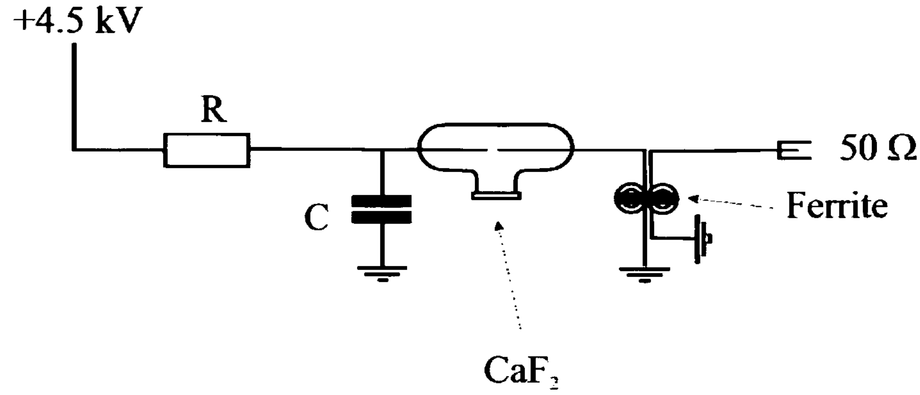

Fig. 4.8: Circuit diagram of the H_2 flash lamp.

4.2.2 Electronics

In order to have the capability to read the charge signals on eight strips, a low noise eight channel charge sensitive preamplifier based on the hybrid (CAEN Mod. 422 - 1/45/90 mV/MeV (Si) selectable via internal jumpers; typical rise time <20 ns) has been constructed [78].

In all the measurements the jumpers are set for the energy sensitivity of 45mV/MeV. *Fig. 4.9* shows a picture of the hybrid card. *Fig. 4.10* illustrates the pinning and the circuit for changing the energy sensitivity. In order to calibrate the gain of the electronics these hybrid cards are provided with additional input pin (test) via a capacitance of 10 pF

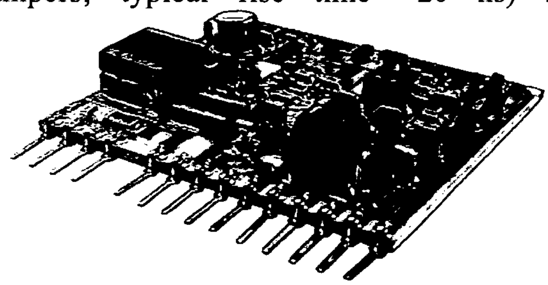

Fig. 4.9: CAEN Mod. 422 charge sensitive hybrid preamplifier [78].

The signals are further amplified by a programmable amplifier unit (4 channel programmable spectroscopy amplifier CAEN Mod. 402A). Charge sensitive gated ADCs (LeCroy 2259) follow the amplifier. As illustrated in *Fig. 4.13* a VME interface connected the ADCs with a data acquisition. A BASIC program (Q1plus8.bas) has been written to record per event the signals received from eight strips.

Switch Configuration			
Sensitivity (mV/MeV)	SW1/A	SW1/B	SW2
90	OFF	OFF	ON
45	ON	OFF	ON
1	ON	ON	OFF

The switches appear as soldering pads:
- switch OFF means no soldering;
- switch ON requires a drop of lead.

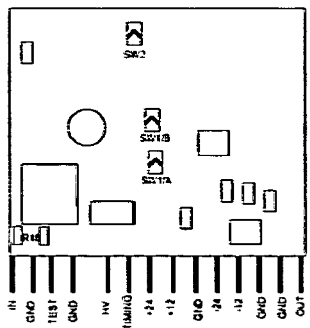

Fig. 4.10: Pinning of the hybrid card and circuit for the selection of the energy sensitivity [78].

By sending pulses of a rectangular shape into the DAQ-chain via the test-input the electronics was calibrated. *Fig. 4.12 (left)* shows the linear response of an arbitrary channel. The measured points are the mean values of a Gaussian fit over a thousand event sample. *Fig. 4.11* shows the measured noise distributions of two channels; as can be seen, one of the two channels has a higher noise. *Fig. 4.12 (right)* illustrates the response of the eight channels. The standard deviation σ of these distributions is later used to perform a 3σ noise-cut on the obtained data.

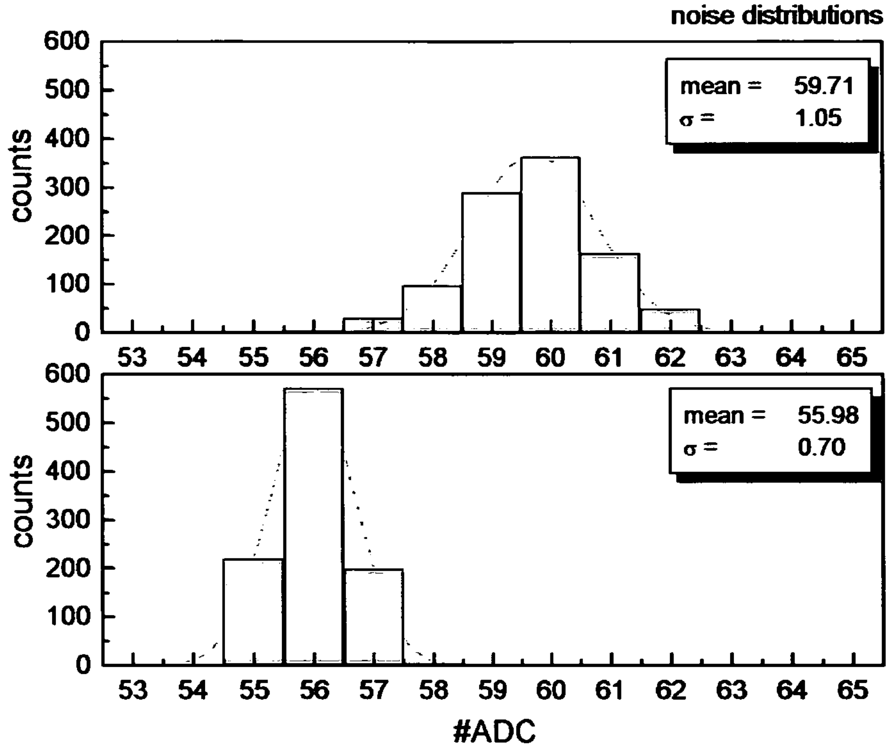

Fig. 4.11: Pedestal and noise determination for two channels with a higher and a lower noise. The dashed lines indicated the Gaussian fits applied on the noise distributions[1ADC=0.17fC].

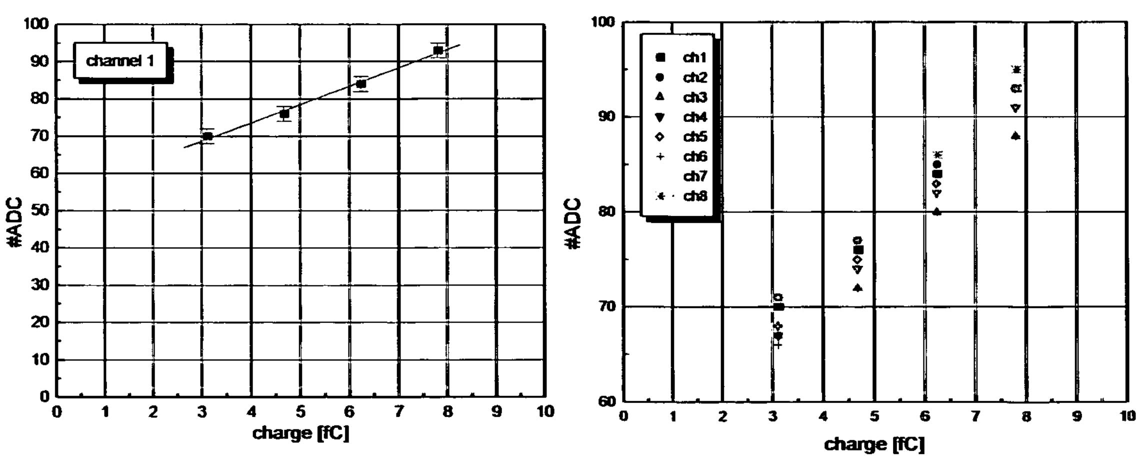

Fig. 4.12: Pedestal determination for channel one (left); the eight channels have a different noise, which leads to the different pedestals and different calibration constants.

A linear fit through the obtained measured ADC positions (obtained by increasing the input amplitudes) determines the pedestal and the calibration constant for every channel.

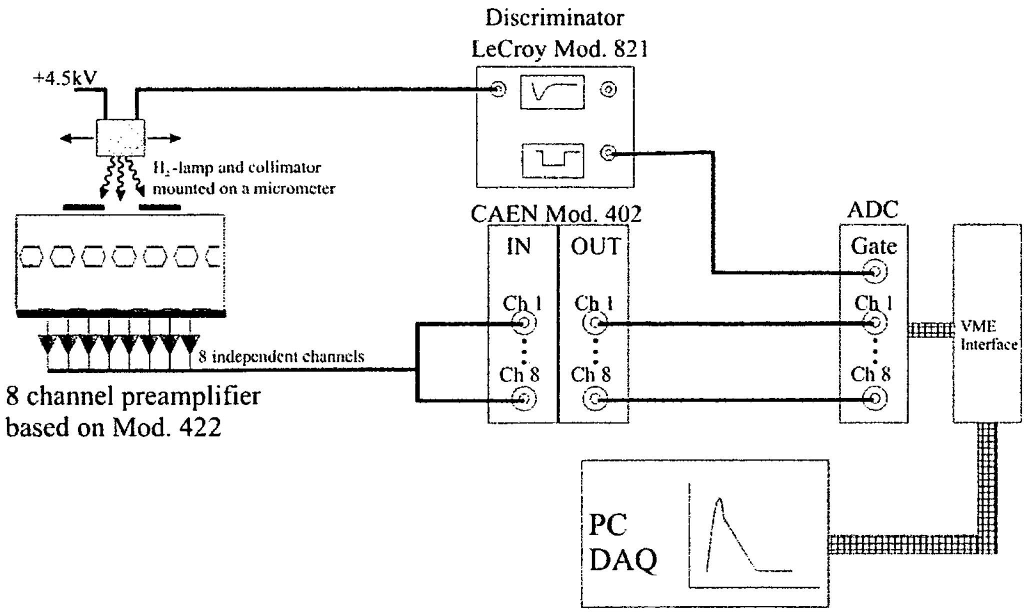

Fig. 4.13: Schematics of the experimental setup. The UV-source can be moved parallel to the detector. The discharge time provides the trigger for these measurements.

4.3 Experimental Results

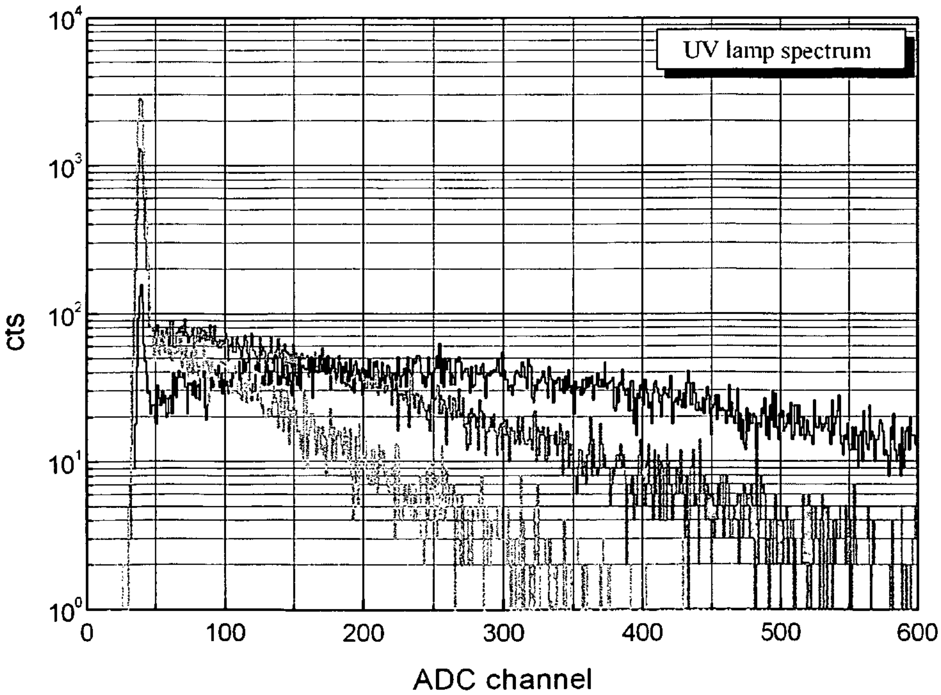

Fig. 4.14: Charge distributions at a decreasing UV light intensity.

Typical pulse height spectra recorded with the detector described above are shown in *Fig. 4.14 & Fig. 4.15*. Decreasing the UV source intensity systematically at a constant gain and trigger signals from the lamp leads to a transition from multiple photon counting to single photon detection, which is definitely distinguishable in *Fig. 4.14*. The pulse height spectra in *Fig. 4.14 & Fig. 4.15* have been recorded with sixteen strips connected together.

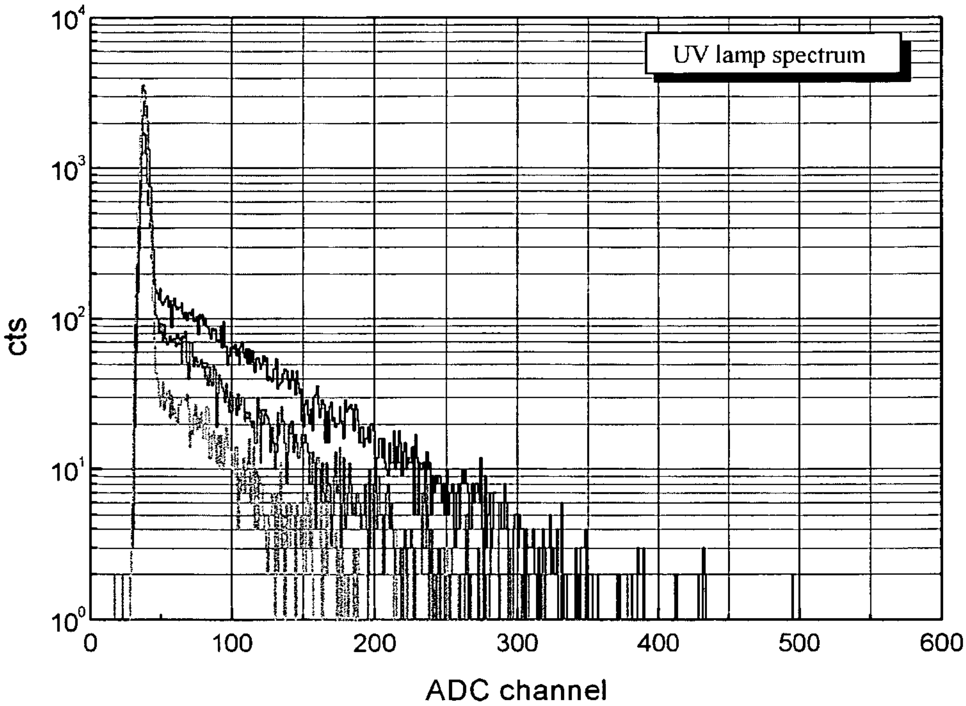

Fig. 4.15: Integral charge distributions in the single photoelectron region.

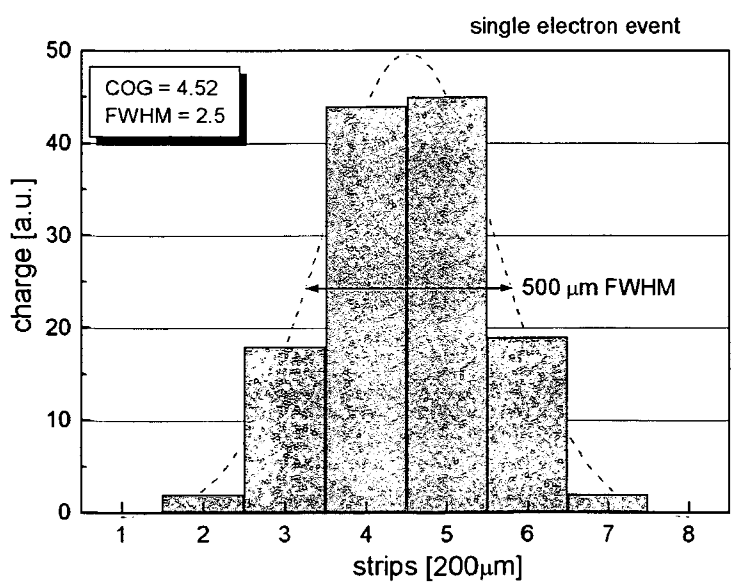

Fig. 4.16: Single event charge distribution. The dashed line represents the Gaussian fit applied on this event to determine the COG and the cluster size.

As outlined in *Chapter 4.1.3* the single photon pulse height spectrum is of an exponential decreasing shape. By reducing the integrated count (at constant detector gain and equal number of coincidence signals from the lamp) without changing the identical exponential shape of the spectrum it is ensured that most of the events contributing to the spectrum are from single photons converted on the CsI layer. The ratio of the number of the integrated counts and the number of triggers gives the probability of measuring one or more photoelectrons. Assuming a Poisson distribution *(Chapter 4.1.3)*, if the integrated probabilty is about 30 % it is guaranteed that most of the events correspond to single photoelectrons (lower curve in *Fig. 4.15*).

As indicated in *Fig. 4.13* the UV source is movable perpendicular to the set of eight parallel strips. A collimator is placed between the detector and the source to focus the photon beam to a width of about 100 μm. The lamp itself is mounted on a micrometer, which allows its movement with the accuracy of about 5 to 10 μm. At every position, corresponding to a measured point in *Fig. 4.18* a data-set (10k events) has been recorded. For example, *Fig. 4.17* shows the pulse height spectrum after having applied a 3σ-cut.

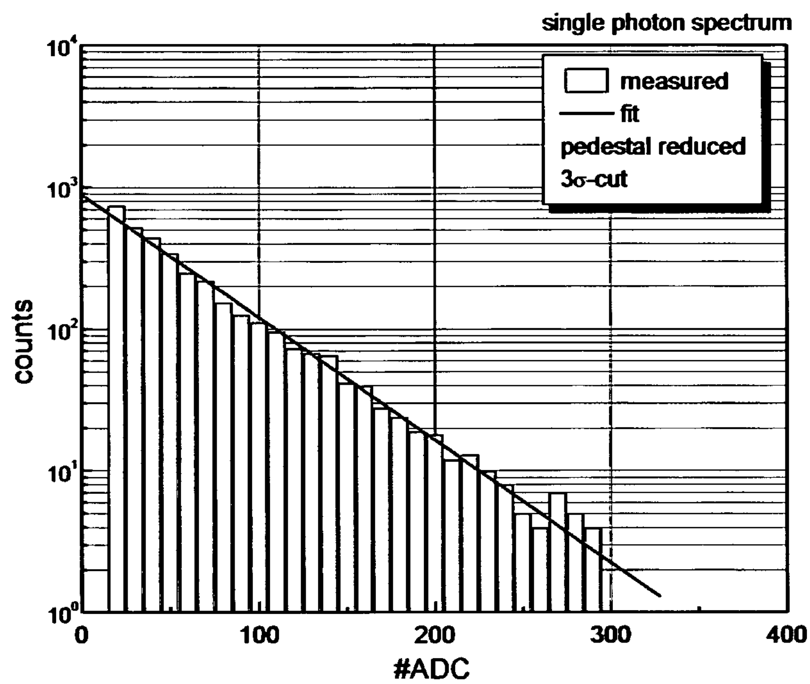

Fig. 4.17: Single photon pulse height spectrum (#pos. 11550 in *Fig. 4.18*).

4.3.1 Method of Center of Gravity

The avalanches drifting from the last GEM induce signals on the anode strips. On the strip closest to the avalanche the signal is the largest and it diminishes proportionately with the distance from the avalanche point. If x_i is the coordinate of the i^{th} strip and q_i the charge measured on this strip, then the avalanche point x can be computed by *Equ. 4.13*.

$$x = \frac{\sum_i (q_i - k_i)x_i}{\sum_i (q_i - k_i)} \qquad \textbf{(Equ. 4.13)}$$

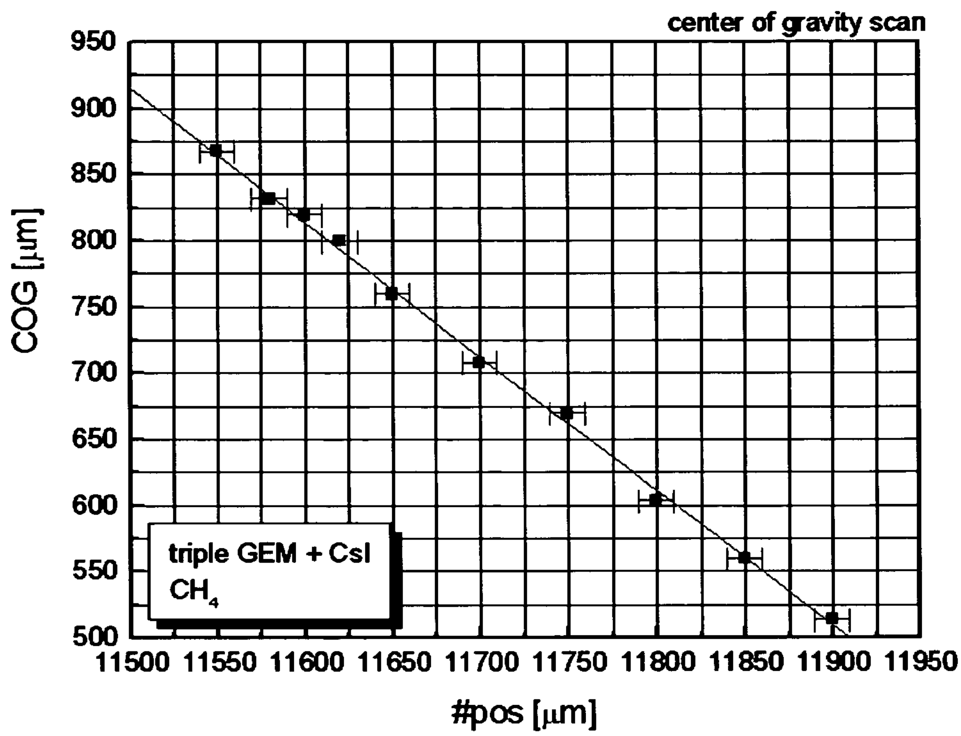

Fig. 4.18: Correlation between the real lamp position and the COG of the charge distribution

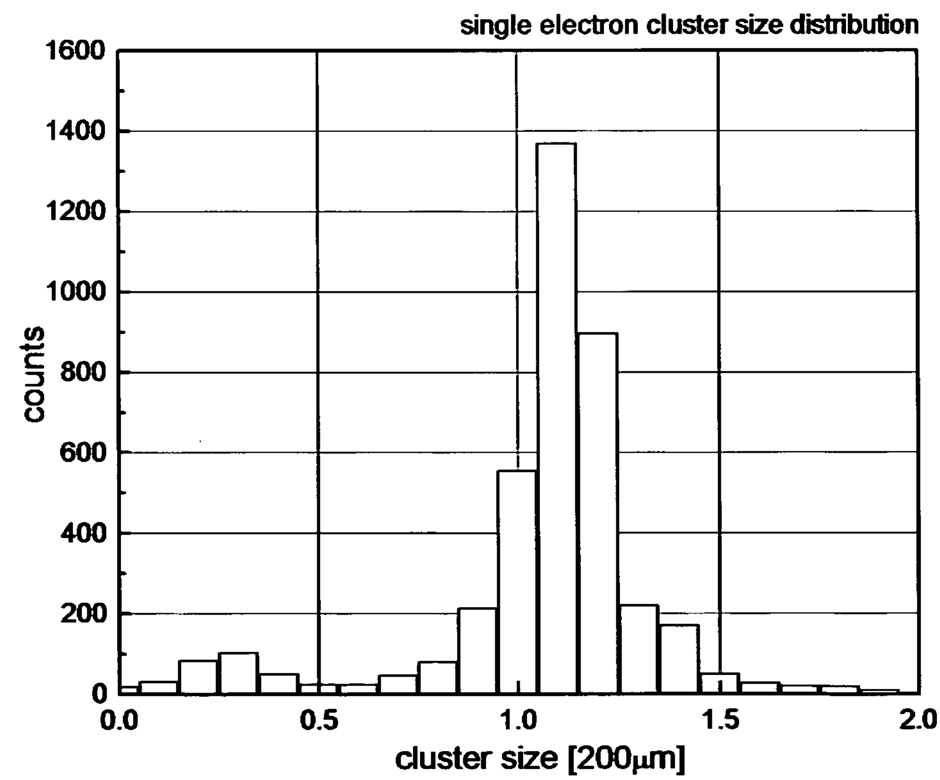

Fig. 4.19: Cluster size distribution for single electron avalanches in strips (strip pitch=200μm).

The factor k_i is the so called pedestal of the i^{th} channel, which has to be reduced from the charge in order to correct for noise effects. A histogram (pulse height spectrum) of the total charge (recorded on the eight strips) after pedestal correction of all events gives the single photon spectrum *(Fig. 4.17)*.

Fig. 4.18 shows the correlation between the geometrical position of the lamp and the computed center of gravity (COG) within about half a millimeter. The charge distribution of a single photon event follows a Gaussian distribution *(Fig. 4.16)*. By fitting every event with a Gaussian function the mean and the standard deviation (respectively the FWHM) of the charge distribution is obtained. The mean value of this distribution corresponds to the center of gravity, the standard deviation gives the cluster size. The COG-distributions for two positions (200 µm apart) are shown in *Fig. 4.20*. These distributions have a FWHM of 160 µm. With the calculated beam size of 100 µm the intrinsic single photon localization accuracy is about 125 µm FWHM (~55 µm rms). The cluster size distribution of single photon avalanches recorded on the anode strips with a pitch of 200 µm is illustrated in *Fig. 4.19*.

Due to the limited sensitive region equipped with electronics in these measurements the two photon resolution could not investigated directly.

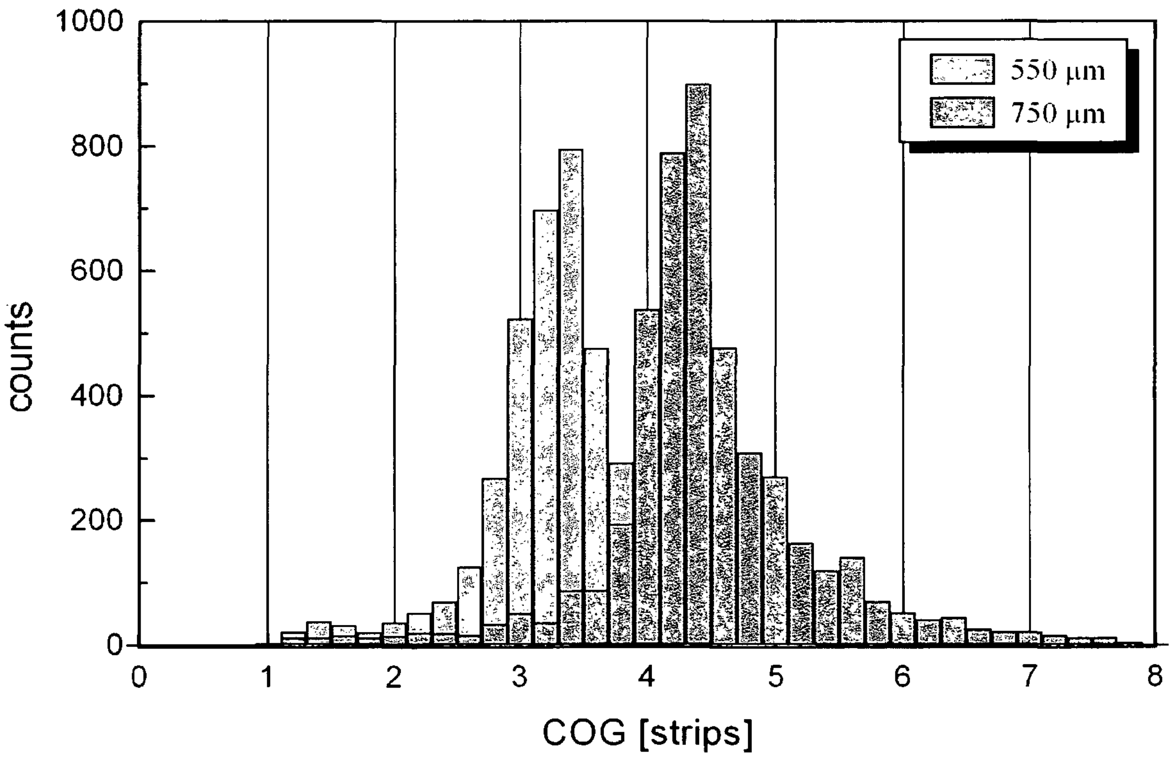

Fig. 4.20: COG distributions for two positions, 200 µm apart, of the collimated photon source.

Chapter 5

Photon Detection and Localization

5.1 Introduction

As outlined in *Chapter 4.1.4* RICH detectors coupled to MWPCs suffer from several problems connected with the limitations of MWPCs and the aging of the CsI photocathode due to the ion bombardment on the CsI surface. A possible way to solve these problems is presented in the following chapter.

A GEM based photon detector *(as introduced in Chapter 4)* allows the detection of single photons with a high efficiency and a good spatial resolution (55 μm rms). Such a GEM photon detector provided with multi-hit capability and the advantages of the GEM-technology *(see Chapter 1.4)* would be suitable for fast RICH applications.

Due to the avalanche confinement in the GEM-channels a suppression of the ion and photon feedback is achieved and high gains are attainable [80]. The high surface field allows extracting efficiently the photoelectrons and injects them into a cascade of three or four GEMs *(Fig. 4.6)*. A reversed drift field eliminates the contribution of ionization released by charged particles in the drift gap. The photon feedback from avalanches is absent due to the fact that the charge amplification is separated from the photon conversion. Most of the ions are produced in the last stage of the multi-GEM detector, therefore ion-feedback is also strongly reduced [83][84].

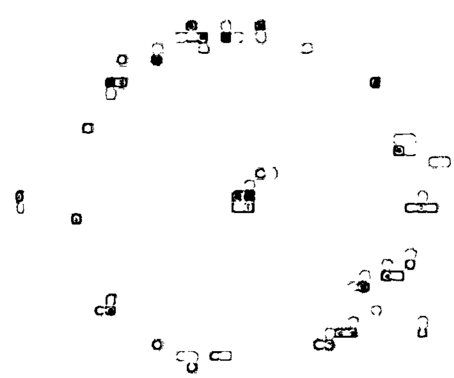

Fig. 5.1: Cherenkov ring of a MIP measured by a RICH detector. The color map represents the signal induced on the pads [86].

Conventional two-dimensional readout devices (e.g.: a set of perpendicular strips) do not allow an ambiguity free reconstruction of close multi-photon hits present in RICH events, although charge sharing may add up to the multi-hit resolution power [82]. The unique feature of the GEM-detector technology, that the amplifying electrodes are electrically separated from the readout structure allows a free choice of the readout structure [79]. In these experiments a special readout board, providing three projections for each coordinate has been used to resolve ambiguities of multi-hit events *(see Fig. 5.1)*. This readout structure is known under the name "HEXABOARD".

Such an approach is cheaper than the use of a matrix of pads as a pick-up electrode providing the best achievable multi-hit resolution.

5.2 Hexagonal Printed Circuit Board - HEXABOARD

As soon as more photons are detected in the same event a reconstruction fails with a standard two dimensional readout board. These kinds of events occur at high rates or if Cherenkov photons are detected. Ambiguities, as illustrated in *Fig. 5.2,* make a unique assignment impossible.

By adding a 3rd coordinate the information necessary to reconstruct such an event is provided. A N photon hit results 3N positions in the respective three projections u_1 .. u_N, v_1 .. v_N, w_1 .. w_N. Hence every position of the charge cluster is determined by three values, which must fulfill the plane equation:

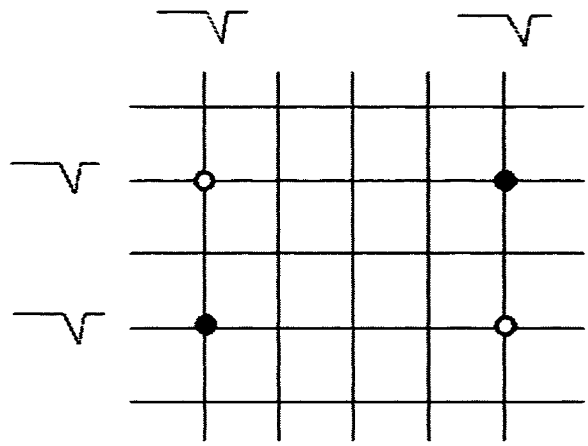

Fig. 5.2: Double photon hit on a Cartesian readout board; the positions of the photons are ambiguous.

$$au_i + bv_j + cw_k = d \quad \textbf{(Equ. 5.1)}.$$

The parameters in *Equ. 5.1* a ,b ,c ,d depend on the angles between the strip layers.

The hexagonal pads, as visible in *Fig. 5.4* – a magnified image of *Fig. 5.3,* are connected alternating to the three different layers. The layers are orientated by an angle of 120°.

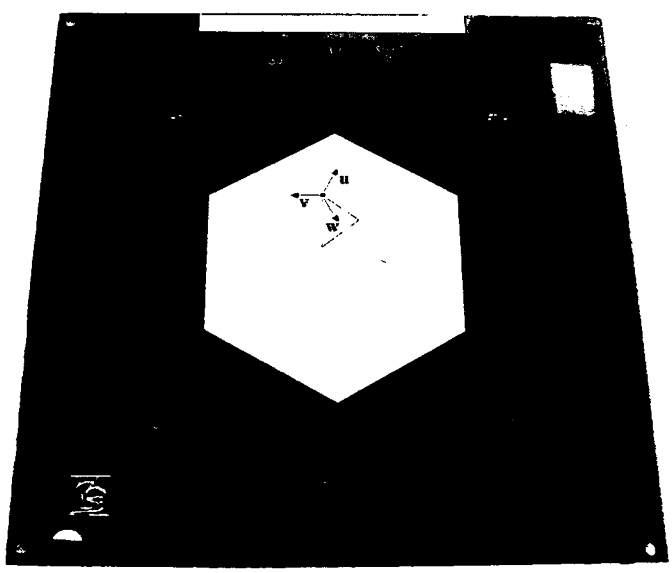

Fig. 5.3: Picture of the hexagonal readout structure (HEXABOARD); the notation of the three projections and the assignment of the mathematical axes are described. The pads and the stripsare made out of Au.

The active are of the board has a hexagonal shape with an edge-length of 5.3 cm and is shown in *Fig. 5.3.* The whole board contains 510 strips, 170 per projection. The mathematical axes are defined orthogonal to the strips. u corresponds to the upper layer, v to the middle layer und w to the bottom layer. The strip pitch of all projections is 520 µm. The pitch between two adjacent pads on the same strip is 600 µm. Due to the limitations concerning the available electronics at the time of this experiment, the useful sensitive area was an overlay of 3x16 channels, which results in a triangular shape (*Fig. 5.4, left)* of an area of about 0.5 cm^2.

The HEXABOARD was developed and produced R. de Oliveira in the CERN-workshop based on an idea of F. Sauli [79][81].

Fig. 5.5 shows the capacitance map of the used HEXABOARD. Unfortunately a lot of shorts between adjacent strips (negative capacitance) and shorts between strips of different layers (larger values than the trend capacitances) complicated the search for a feasible zone. During the writing of this thesis de Oliveira managed to produce flawless boards.

The position of this zone can be specified by three numbers on the adaptor card corresponding to the respective projection layer. In this case the positions 8 (w), 16 (v) and 25 (u) have been chosen. The origin of the coordinate system is set in the corner of the triangular (indicated by the blue dot in *Fig. 5.4, left*). For this hexagonal geometry *Equ. 5.1* becomes

$$(u_i - 15) - v_j + (w_k + 1) = 0 \quad \textbf{(Equ. 5.2).}$$

u_i, v_j, w_k are the COG positions (in terms of strips) *(see Chapter 4.3.1)* of the charge cluster.

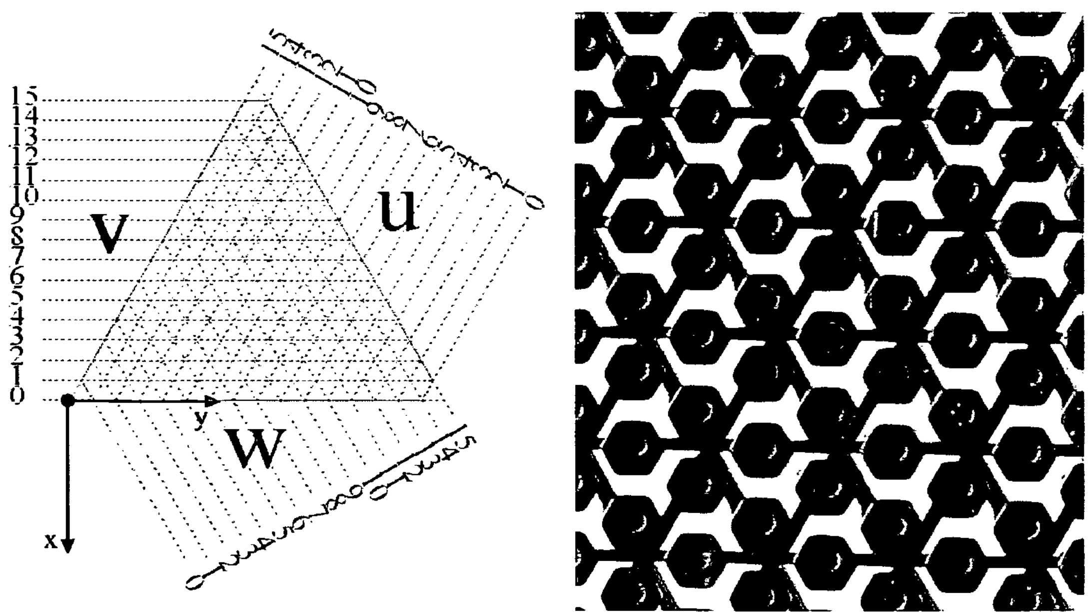

Fig. 5.4: Mapping of the 3 x 16 channels. The coordinate system indicates the choice of the axis, which is needed for the definition of the transformation matrices (left). On the right a magnified spot on the HEXABOARD is visualized. Alternatively the hexagonal pads are connected to the respective projection (black: v-projection, blue: u-projection, red: w-projection). The strip pitch is 520 µm. Pads on the same strip are 600 µm away from each other.

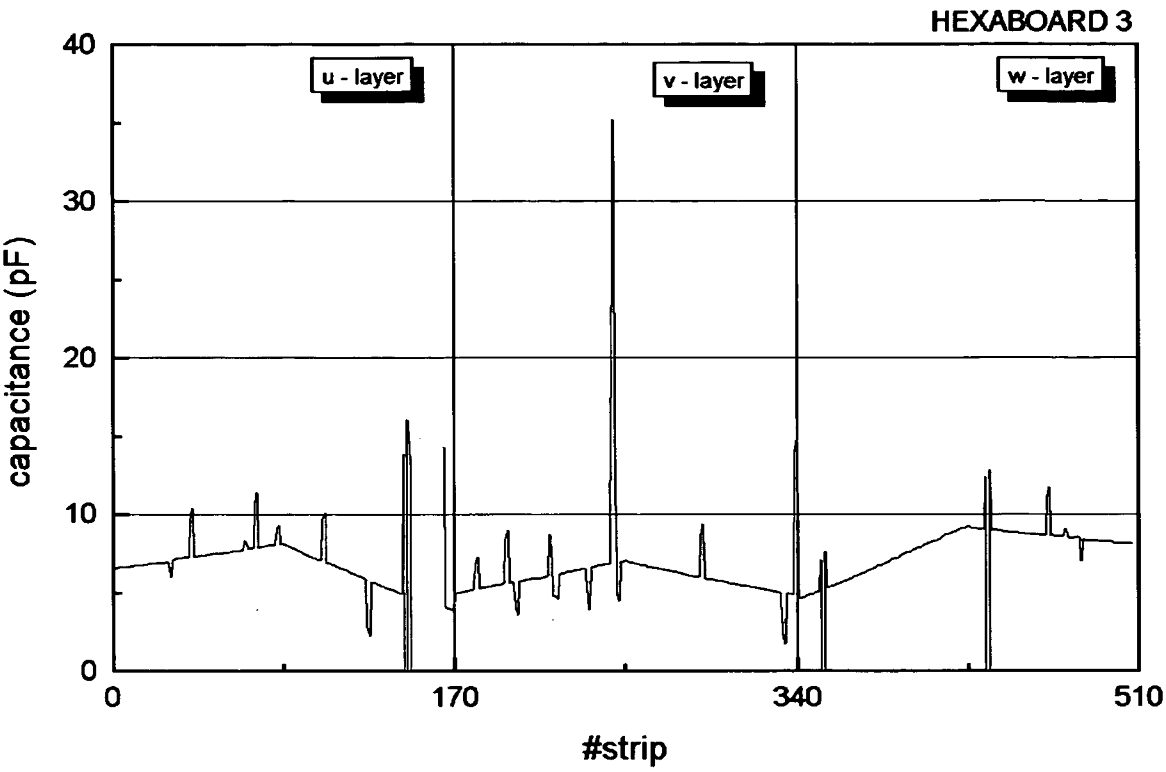

Fig. 5.5: Capacitance map of the used readout board. The capacitance between two adjacent strips was measured. Negative values denote a short between the two strips. Smaller values than the trend values indicate broken strips and higher values than the trend values are shorts between the layers.

5.3 Front End Electronics

In order to readout the charge signals induced on the single pads the Front End Electronics (FEE) is connected to the adaptor Card *(Fig. 3.8)*, which is wire-bonded to readout strips of the HEXABOARD. A single FEE channel is comprised of three basic functional units: (1) a charge sensitive amplifier/shaper with a semi-Gaussian response (200 ns FWHM) *(see Chapter 5.3.1)*; (2) a 10 bit ADC (up to 25 MHz sampling rate); (3) a data processor with a multi-acquisition buffer *(see Chapter 5.3.2)*. The ADC and the data processor for 16 channels are implemented in one ALTRO chip, a custom mixed-signal chip. The Front End Card (FEC), which is a modified version of the ALICE TPC front end card, is equipped with 4 ALTRO chips and therefore accommodates 64 channels.

Front End Bus cables interface a Mezzanine Card to the FECs and establish the link between the FEC and PCI-based Readout Control Unit (RCU). The RCU controls the FECs and interfaces them to the trigger and Data Acquisition (DAQ). The RCU broadcasts the trigger information to the individual FEC modules and controls the readout procedure. The implementation of these functions is done by a custom bus, based on low-voltage signaling technology (GTL), the ALTRO bus.

A LABVIEW program (DAQ2tkm.vi) written for this purpose records per event the digitized signals of each channel within an adjustable time window of maximal hundred time slices (4 μs). Depending on the respective measurement the event data is saved in an ASCII-file. The data analysis is performed offline by developed ROOT programs.

5.3.1 Preamplifier

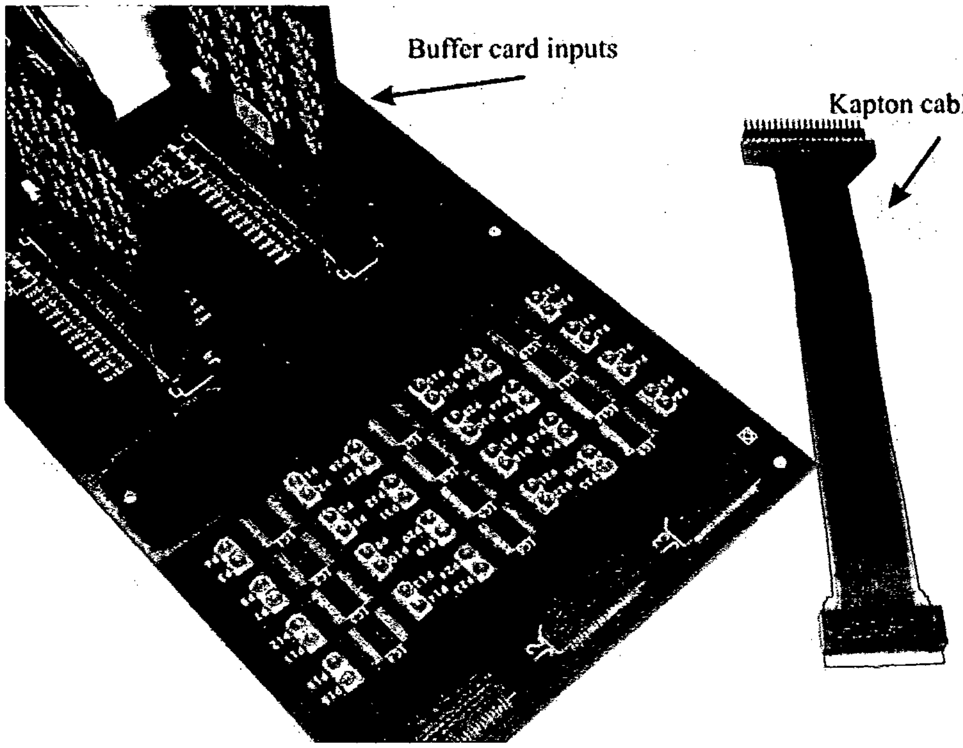

Fig. 5.6: Picture of the preamplifier card equipped with J.C. Legrand's amplifier. Each chip processes four channels. The whole preamplifier card contains 3 x 16 channels. Special flexible Kapton cables connect the output of the Adaptor card with the input of the preamplifier card. The connection is performed with a SAMTEC QTE-020-01-L-D connector.

The charge collected on the pads is amplified and integrated by a charge sensitive amplifier (developed by J. C. Legrand). The FECs are connected to the preamplifier cards (*Fig. 5.6*) by buffer cards. These transport the amplified and shaped signals via about four meter long small coaxial cables to the input of the respective FEC. These FECs are not close to the detector. The preamplifier cards are connected to the adaptor card *(Fig. 3.8)* by means of short (10 cm) flexible Kapton cables. Due to the use of the buffer cards and the preamplifier cards, which have been available from the HARP-experiment, one FEC has to handle only 48 channels, whereas it is capable of processing 65 channels.

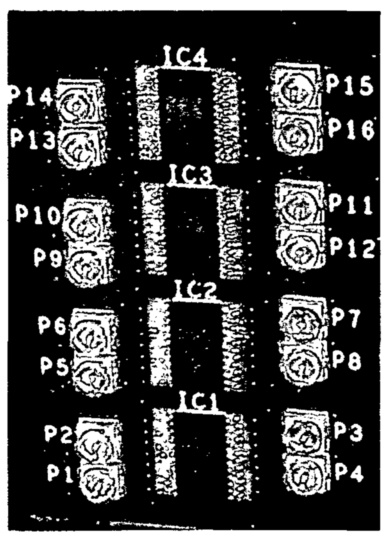

Fig. 5.7: Notation of the 4 ICs of the preamplifier input J1, together with the potentiometers (see Table 5.1, 3rd column).

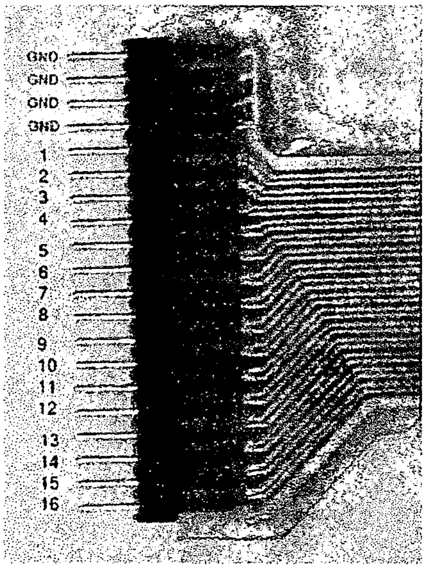

Fig. 5.8: Notation of the pinning of the readout channels of the flexible Kapton connector cables. On the other side of the cable a SAMTEC-connector is soldered.

channel	CC	P (Potentiometer)	ALTRO channel
16	SW 3/8	1	60
15	SW 4/8	2	24
14	SW 3/7	5	21
13	SW 4/7	6	25
12	SW 3/6	9	23
11	SW 4/6	10,bad	26
10	SW 3/5	13	22
9	SW 4/5	14	20
8	SW 3/4	16	52
7	SW 4/4	15	57
6	SW 3/3	12	62
5	SW 4/3	11	58
4	SW 3/2	8	63
3	SW 4/2	7	55
2	SW 3/1	4	50
1	SW 4/1	3	27

Table 5.1: Mapping of the real neighboring channels with the ALTRO output channels for the 2nd preamplifier card P2.

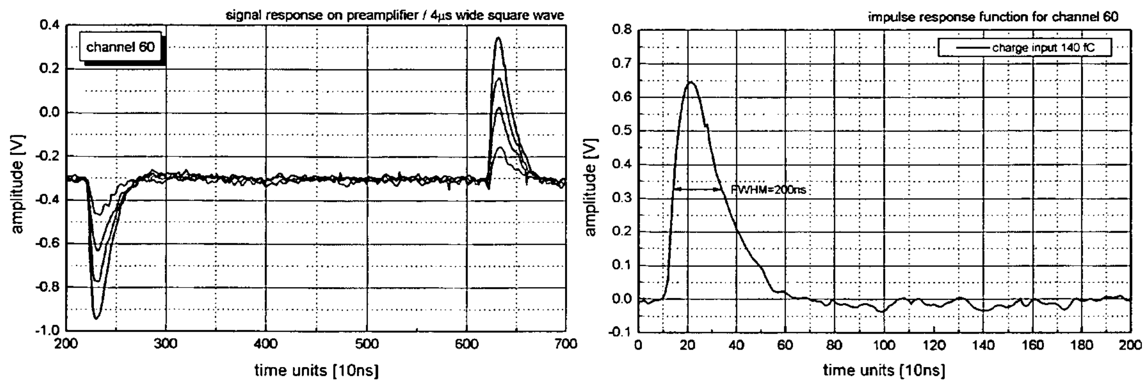

Fig. 5.9: Response of channel 60 (P1) for four different amplitudes of a square wave, measured on the preamplifier output before the FEC (left). Legrand amplifier response function (right). The rise time is 80-90 ns and the FWHM of the signal about 200ns.

Neighboring strips on the readout board of the detector are not necessarily adjacent ALTRO channels. Therefore every single channel has to be allocated to its ALTRO channel. *Fig. 5.7* shows the four chips and the notation of the preamplifier input J1. The dynamic range of each channel could be adjusted by changing the value of the potentiometer. *Table 5.1* illustrates the mapping of the first 16 channels of the 2nd preamplifier card (P2). For example, a charge induced on channel number 10 would lead to a recorded digitized signal on the ALTRO channel number 22. For calibration purposes a special calibration card (CC) has been built *(Fig. 5.14)*. In the 2nd column of *Table 5.1* the notation on the CC and the corresponding ALTRO channel is specified. With this card single channels can be addressed. *Fig. 5.9* shows the response of an arbitrary channel on the preamplifier output, when a 4 µs square wave is sent into the preamplifier card via the

SW3/8 connector on the CC. A rise time of 90 ns and a shaping time of 200ns of the response function could be measured.

The mapping of the whole readout chain of the two existing FECs and the two Legrand-preamplifier cards (P1 & P2) can be found in Appendix B.

5.3.2 ALTRO (ALICE TPC Read Out) chip

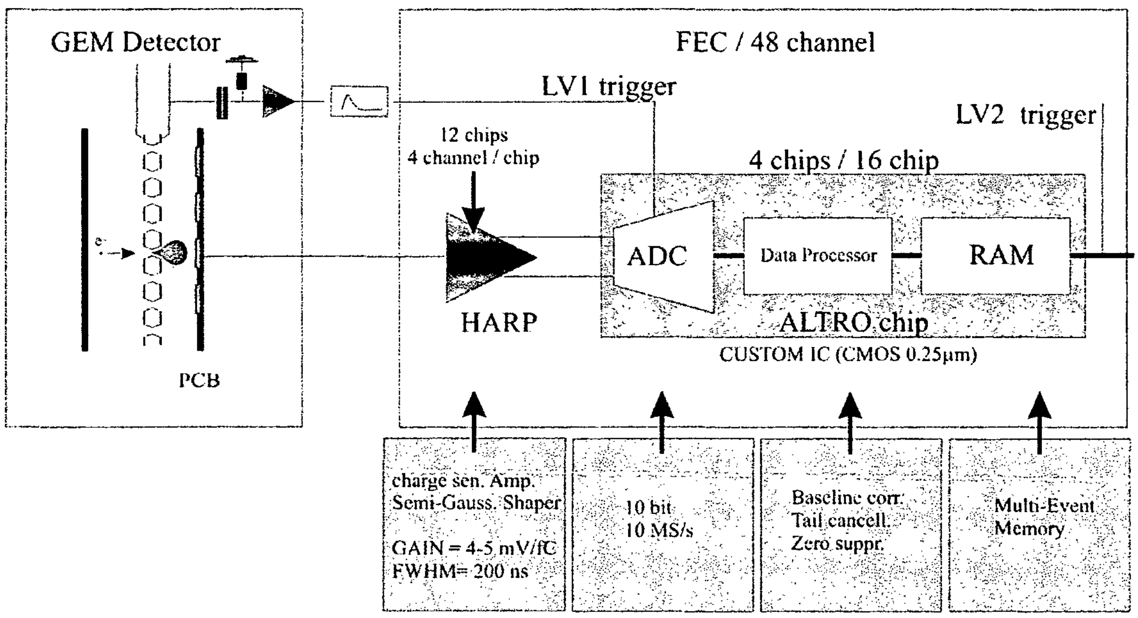

Fig. 5.10: An overview of the detector front end electronics. LV1 needs a +3.3V (TTL) signal. The trigger signal is processed as shown in Fig. 3.12, before a Level Adapter (LRS 688AL) converts it.

The ALTRO chip is a mixed-signal ASIC designed to be one of the building blocks of the readout electronics for gaseous detectors. Originally developed and optimized for the TPC of the ALICE-experiment at CERN its architecture and programmability make it suitable for the readout of a wider class of detectors. It operates concurrently on the analogue signals from 16 channels, which are digitized, processed, compressed and stored in a multi-acquisition memory. The analog-to-digital converters embedded in this chip have a 10-bit dynamic range and a maximum sampling rate in the range of 25 MHz.

After digitization, a pipelined data processor is capable of removing perturbations from the input signal, related to the non-ideal behavior of the detector, temperature variations of the electronics, environmental noise etc. Moreover, the data processor is able to suppress the pulse tail within 1 μs after the peak with 1‰ accuracy, thus narrowing the pulses to improve their identification.

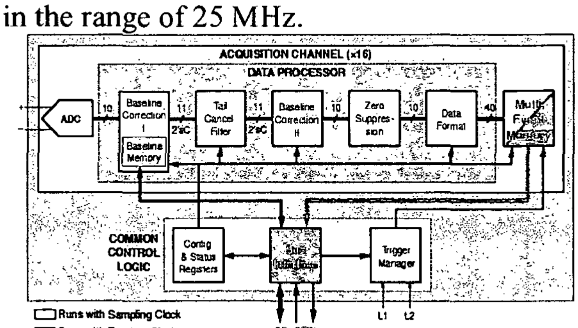

Fig. 5.11: Block diagram of the ALTRO chip [85].

This feature is not used due to the fact that GEM signals do not have an ion-tail.

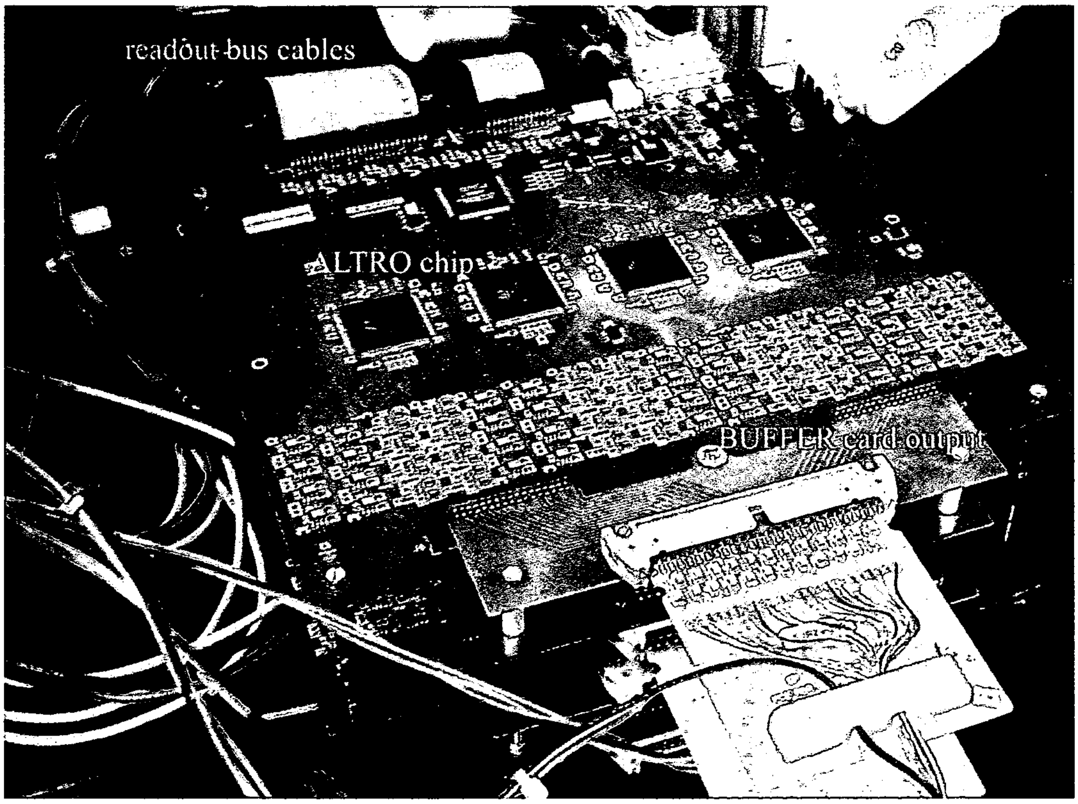

Fig. 5.12: Two FECs with four ALTRO-chips. Buffer cards establish the connection between the preamplifier and the FEC.

The signal then can be compressed by removing all the date below a programmable threshold (Zero Suppression). The data can be readout from the chip through a 40 bit wide bus. Each data packet is marked with its time stamp and size – so that the original data can be reconstructed afterwards – and stored in a multi-acquisition memory that has a readout bandwidth of 300MByte/s. The data processing and the readout of the data memory are performed at different frequencies (sampling clock: max. 20 MHz / readout clock: max. 60 MHz).

When a first level trigger (LV1) is received *(see Fig. 5.10)* a predefined number of samples of a digitized signal is processed and stored temporarily in a data memory. Trigger related data is stored in a multi-event buffer. A multi-event buffer is a 1024x40 RAM partitioned in a programmable number (4 to 8) of fixed-length buffers. The maximum number of samples that can be processed for each trigger (data stream) is 1008, if the data memory is partitioned in four buffers. 8 buffers can be used if the data processor is configured to process less than 512 samples. Upon the arrival of a second level trigger (LV2) the latest acquisition is frozen, otherwise the data stream will be overwritten by the next acquisition.

As shown in *Fig. 5.11*, after the analogue digital conversion, the signal processing is performed in five steps: a first correction and subtraction of the signal baseline, the cancellation of long-term components of the signal tail, a second baseline correction, the suppression of the samples so close to the baseline that contain no useful information, and formation. Every single ALTRO channel is comprised of seven main building blocks described hereafter:

- The analogue input signal is converted into a digital stream by an Analogue-to-Digital (ADC) with 10-bit dynamic range and up 40 MS/s (25MHz) sampling rate. It is based on a commercial ADC, the ST Microelectronics TSA1001. The ADC is based on a fully differential circuit. It measures the voltage difference (V_d) between the ADC inputs (V_p: positive input, V_n: negative input) while it is insensitive to the absolute values V_p and V_n, provided within the ALTRO supply voltages. Two reference voltages (V_t top ref. Voltage) and V_b (bottom ref. Voltage) define the dynamic range and the conversion gain accordingly.
- The first baseline correction corrects the systematic instability of the signal baseline, allowing the subtraction of time-dependent pedestal values taken from the pedestal memory. At this step the variations of the pedestals in between the triggers are also self-corrected. Alternatively the pedestal memory can act as a look-up table, addressed by the input data that can be used to perform a conversion of the input signal during the pedestal subtraction. Finally the pedestal memory can be used to generate a test pattern; an important feature that allows a complete test of the overall processing chain without input signal.
- Although suited for a wider class of applications, the ALTRO chip has been designed for the readout of the cathode pad plane of a conventional multi-wire proportional chamber *(see Chapter 1.3.1)*. There the signal is created by an ionization avalanche created in the vicinity of the anode wires. Moving from the anode wires towards the surrounding electrodes positive ions induce a positive current signal on the pad plane. This current signal can be characterized by a fast rise time (less than 1 ns) and a long tail with rather complex shape, which depends on the wire and pad geometry. The signal tail increases the superimposition of subsequent pulses (pile-up) rendering the zero suppression quite inefficient. An accurate cancellation of the signal tail is required to perform efficiently the zero suppression. The tail cancellation filter is based on the approximation of the tail by the sum of exponential functions. Flexibility for the different 16 channels is given by the possibility to re-configure channel by channel the digital processing by changing programmable coefficients. The use of the tail cancellation filter in the processing chain can be optional.
- After tail cancellation a second baseline correction corrects the perturbation of the baseline produced by non-systematic effects. Assuming the systematic and tail-dependent perturbations have been removed in the previous two stages, any remaining deviation is due to non-systematic effects. The second baseline correction computes a moving average on certain samples and then subtracts this value form the signal.
- The zero suppression is based on a fixed threshold pulse detection scheme, where samples of value smaller than a constant threshold, are rejected. To reduce the noise sensitivity a glitch filter checks for a consecutive programmable number of samples above the threshold. In order to keep enough information for further extraction a programmable sequence of pre-samples and post-samples is also recorded.

- The zero suppressed data is formatted in 40-bit words. Every block of samples is labeled with its time and length to allow posterior reconstruction. At the end of the acquisition period, the data block is labeled with a trailer word. The whole structure is back-linked, that is, each trailer word points to the end of the previous block.
- The trigger information is received in the Readout Control Unit (RCU) and then distributed to the ALTRO chips by means of two signals. The first one, LV1, starts the data processing; the event triggered is also stored in the multi-event memory. The dead time generated by a gaseous detector has two contributions: the detector dead time, e.g.: the drift time, and the front electronics dead time (read out dead time). The multi-event buffer scheme can reduce the second contribution.
  The system dead time depends on the dimensions of the front-end multi-event buffer. The data is continuously processed when a trigger is received, a window (Processing Time Window, PTW) defines the stream of data to be formatted and stored in the multi-event memory. The implementation of the processing chain requires 18 pipelined stages. With this pipeline a programmable number of samples before the trigger (pre-trigger samples) can be stored by enlarging the PTW. This feature allows the compensation of the trigger latency to the extent of 12 times the sample clock period.

The ALTRO chip is interfaced to the external world via 16 analogue inputs and to the readout system through a digital bus composed of a 40 bit bidirectional lines and 8 control lines. The bus protocol is asynchronous for instructions, with a 2-line handshake. The readout, however, is a synchronous block transfer that allows a rate up to 300MByte/s.

A FEC is powered by three different voltages *(Fig. 5.13)*. The Mezzanine card and the RCU operate independently at a voltage of +5V and zero. On the buffer cards a voltage difference of 10 V (-5V / 5 V) is applied.

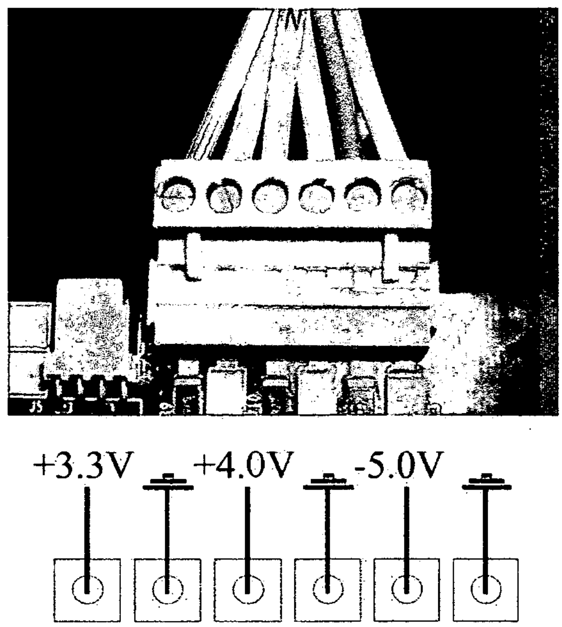

Fig. 5.13: Powering of one FEC.

5.3.3 Calibration of the FEE

With a pulse generator (Stanford Research System, Inc., Mod. DG535) a variable positive square wave was given on a defined capacitance of 15pF situated on the CC *(Fig. 5.14)*. *Fig. 5.15 & Fig. 5.16* show the response functions of an arbitrary channel measured on the output of the preamplifier and by the ALTRO FEE.

The CC allowed addressing all 16 channels of one preamplifier input in the same readout cycle, which simplified the calibration procedures tremendously. The LV1 trigger for the DAQ was obtained by the negative square wave of the pulse generator.

Systematically the amplitude of the square wave was increased and 100-event data samples for each channel and voltage amplitude were recorded. *Fig. 5.17* illustrates the signals for seven different amplitudes corresponding to a certain amount of charge.

A ROOT program written for this purpose computed the mean value and the standard deviation of the amplitude distribution (for the 100 events) for each time slice. The results were written to a file and a LABVIEW program processed in a next step the respective data files.

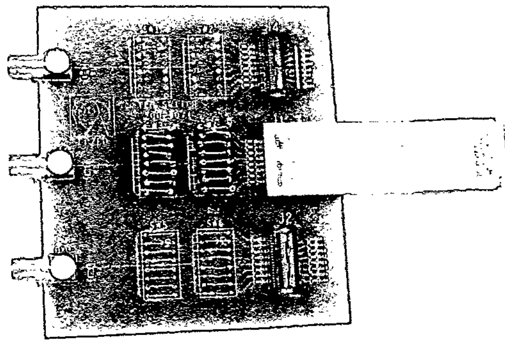

Fig. 5.14: Calibration card (CC): by removing the respective connections single readout channels can be addressed; the capacitance of the connector position J1 (middle) is 15pF.

For a given time slice (time sample) the program applied a linear fit on the computed data points for determining the baseline (#ADC) and the calibration constant (#ADC/fC) of each channel (*Fig. 5.17*).

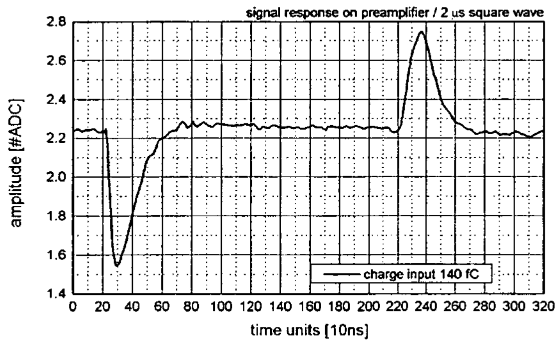

Fig. 5.15: Response function of the preamplifier (channel 12) measured with scope-probe.

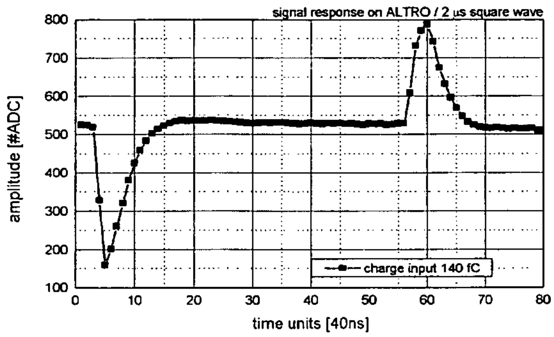

Fig. 5.16: Response function of the same preamplifier channel recorded with the ALTRO FEE.

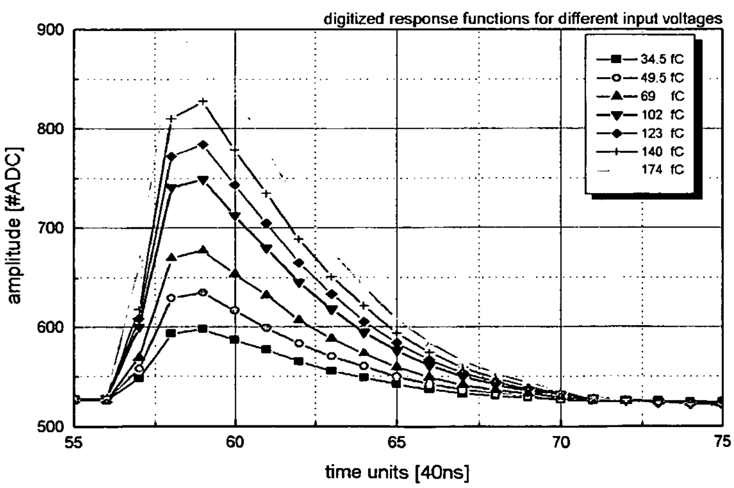

Fig. 5.17: Response functions of channel 49 for different input charge values in order to calibrate the DAQ readout chain.

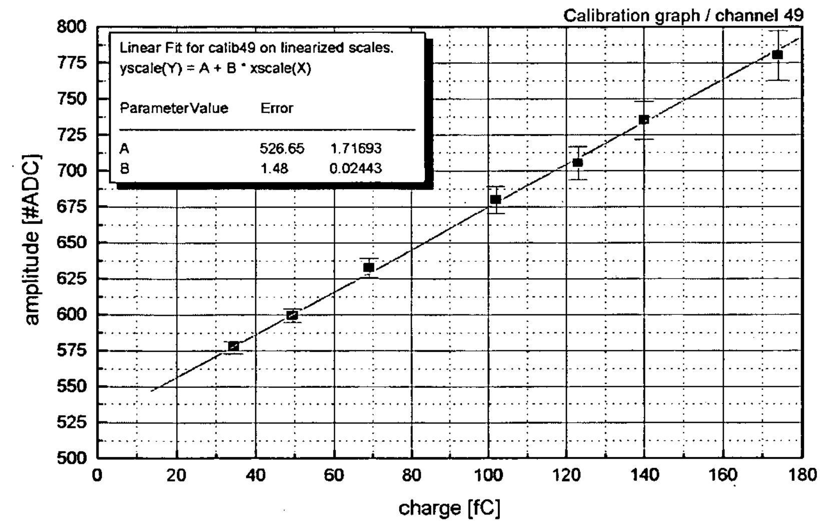

Fig. 5.18: Correlation between the input charge and the amplitude (in ADC units). The parameter A refers to the baseline of this channel. B is the calibration constant in #ADC/fC.

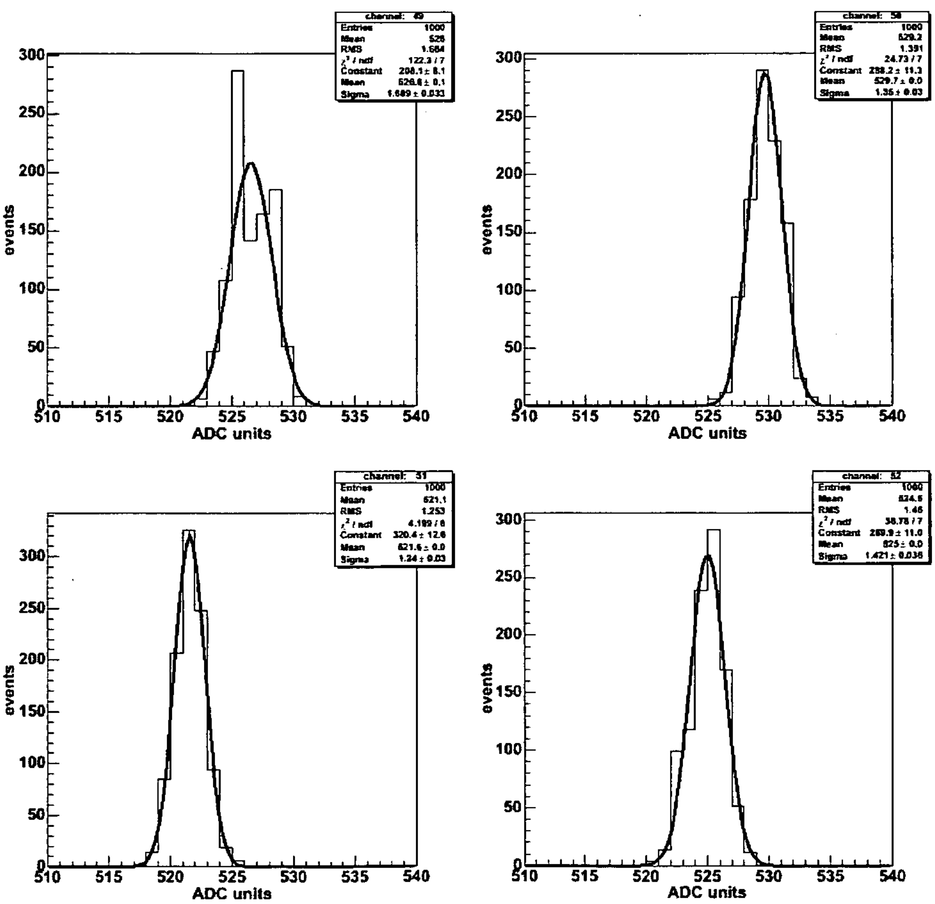

Fig. 5.19: Noise distributions of four arbitrary channels; the mean values of the Gaussian fits are the measured baselines. The width (2σ) is an indicator for the amount of noise of a channel.

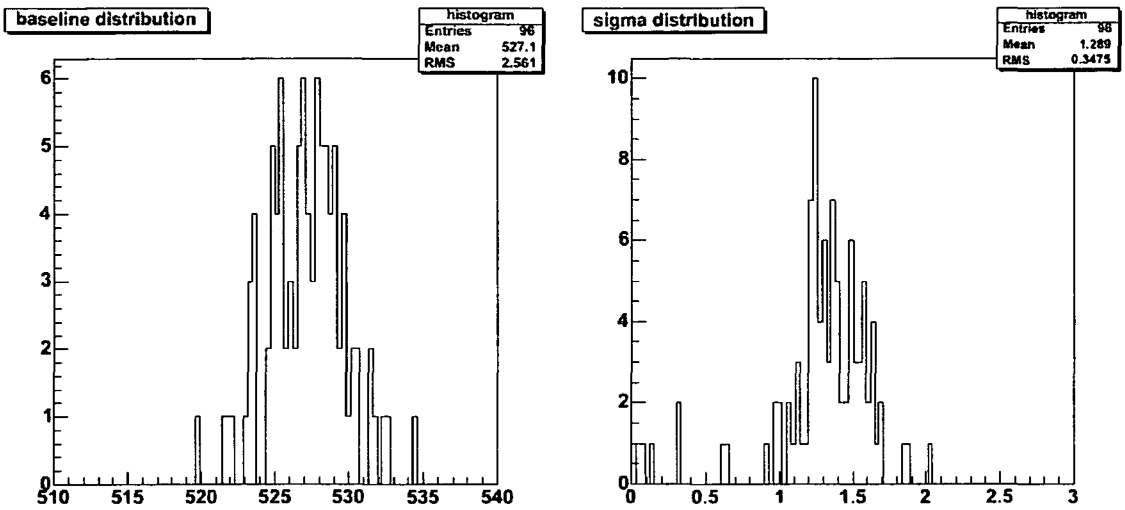

Fig. 5.20: Baseline and sigma distribution of the 96 available readout channels of the ALTRO FEE.

When the GEM-detector is coupled to the FEE and the GEM-detector is operational the noise levels can be different. In order to measure the noise levels (in terms of the σ of its noise distribution) the DAQ is provided with an internal random trigger, by which a 1000 event sample for an arbitrary time slice is recorded. *Fig. 5.19* shows the noise distributions of four arbitrary channels.

A different way to measure the noise distributions per channel is to irradiate the detector with external radiation source (X-ray or UV-lamp) outside the sensitive zone of the HEXABOARD. In that way the DAQ can be triggered by real signals induced from the electron avalanches on the bottom of the last GEM (Fig. 3.12). The values obtained in that way are not different from the values measured by the first method.

The baselines and the standard deviations are finally used for an offline baseline reduction and a noise cut applied on the measured data. The baseline and noise distribution are presented in *Fig. 5.20*. σ-values close to 0 indicate dead channels.

5.3.3.1 Test of the FEE with a parallel-strip GEM-detector

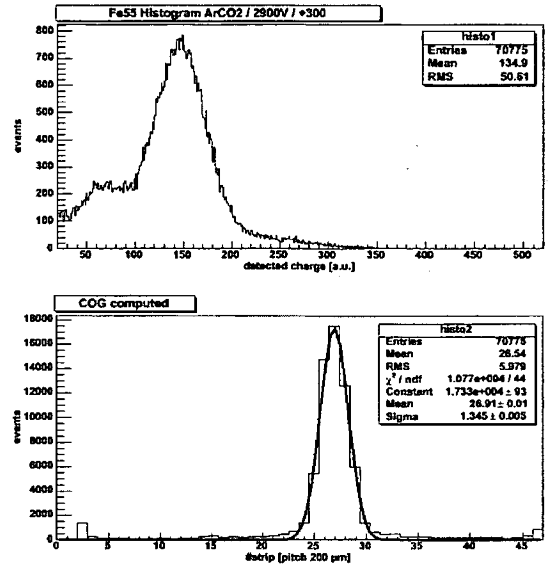

Fig. 5.21: Recorded Fe_{55}-source pulse height spectrum by a parallel strip GEM-detector in $ArCO_2$ (70:30) (above); (below): COG-distribution for evaluating the COG (200 µm strip pitch).

After the calibration of the Data acquisition (DAQ) the complete readout chain was connected to a GEM-detector equipped with a parallel strip readout board *(see Chapter 4)*. The noise distributions of each channel were measured as described above.

A perpendicular to the strips movable X-ray source was put in front of the gaseous detector. *Fig. 5.21* shows the measured Fe55-spectrum together with the COG-distribution obtained on an arbitrary spot in the sensitive zone. A 3σ noise-cut has been applied on the datasets.

In order to check the correct mapping and the response of the channels the source was moved and less detailed datasets (10k events) were recorded to perform a COG-scan, which is illustrated in *Fig. 5.22.*

The plot correlates the position of the source and the corresponding center of gravity *(see also Chapter 4.3.1)*.

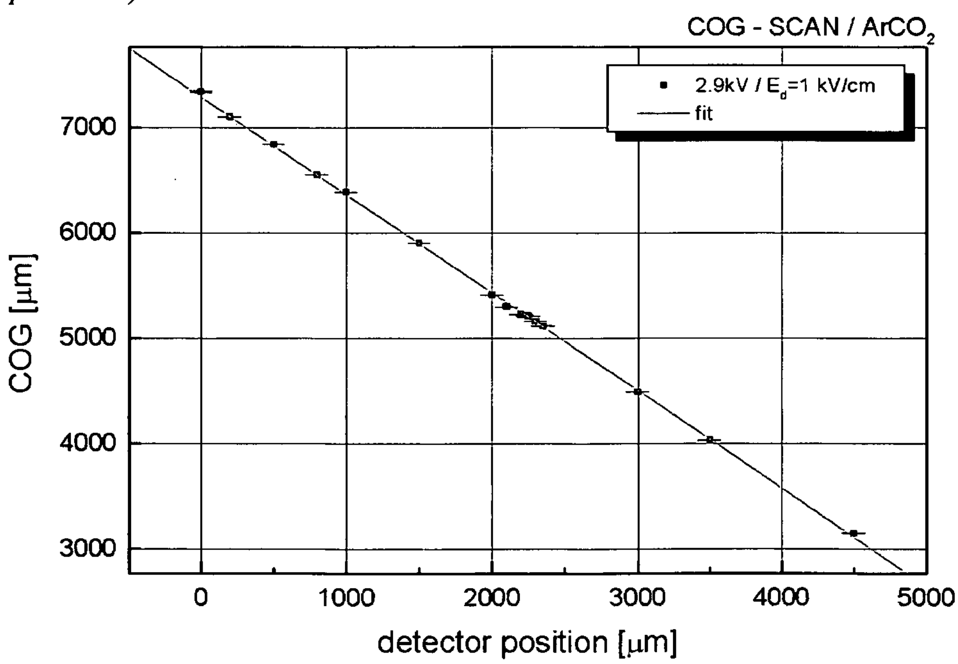

Fig. 5.22: COG-scan over a range of 5 mm in order to check the mapping and the response of the channels.

5.4 Commissioning of the GEM Photo-Detector

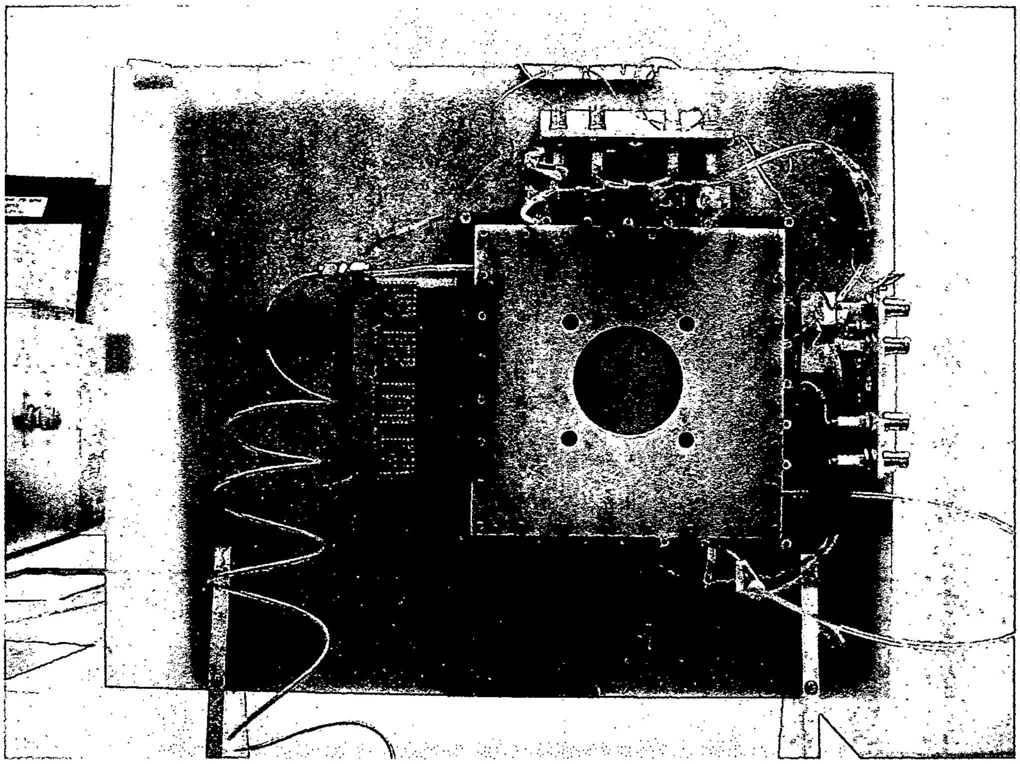

Fig. 5.23: Front view of the GEM Photo-Detector equipped with the HEXABOARD for the performance of multi-hit studies.

A first step in the commissioning of the prototype GEM-photo-detector *(as in Chapter 4.2)* had to be performed with the standard Kapton front-cap. Under these conditions the Fe55-spectrum *(Fig. 5.24)* was recorded with the ALTRO FEE to check, whether the energy resolution of the triple-GEM detector was adequate and the ROOT-programs written for data analysis of the HEX-data (data from the detector equipped with the HEXABOARD) ran without any errors. The HEXABOARD *(Fig. 5.3 & Fig. 5.4)* is a multi-layer structure equipped with hexagonal pads facing the GEM cascade. The pads are connected to three sets of strips (u/v/w) running at three different depths. The angle between the strips is 120°. The use of three projections allows removing ambiguities from multi-hit events.

The counter gas was $ArCO_2$ (70/30) and the detector was irradiated with X-rays from the F_{55}-source. The average voltage ΔU was 365V per GEM and the electrical fields between them about 3.5kV/cm. The effective gain was about 2 10^3. The drift field was 1kV/cm.

In the pulse height spectrum *(Fig. 5.24)* only events were taken into account which had hits in all the three projections (c1&c2), which is equivalent of a fulfillment of the plane equation *(Equ. 5.1)*. As presented in *Chapter 4.2,* in CH_4 the triple-GEM detector should be in the single photon mode at a voltage of 512 V across the three GEMs. Before mounting the CsI-GEM was tested in the clean room in the stainless steal storage box up to 550V under the constant flush of N_2, but mounted into the detector and flushed with CH_4 the chamber was not able to reach the necessary effective gain of about 10^6. At an average voltage of about 480V the detector started to discharge. The necessary gain could be reached by adding a 4th GEM. In order to achieve that also the resistor chain had to be modified due to the fact that the current limit (1mA) of the HV power supply was reached *(Fig. 5.25)*.

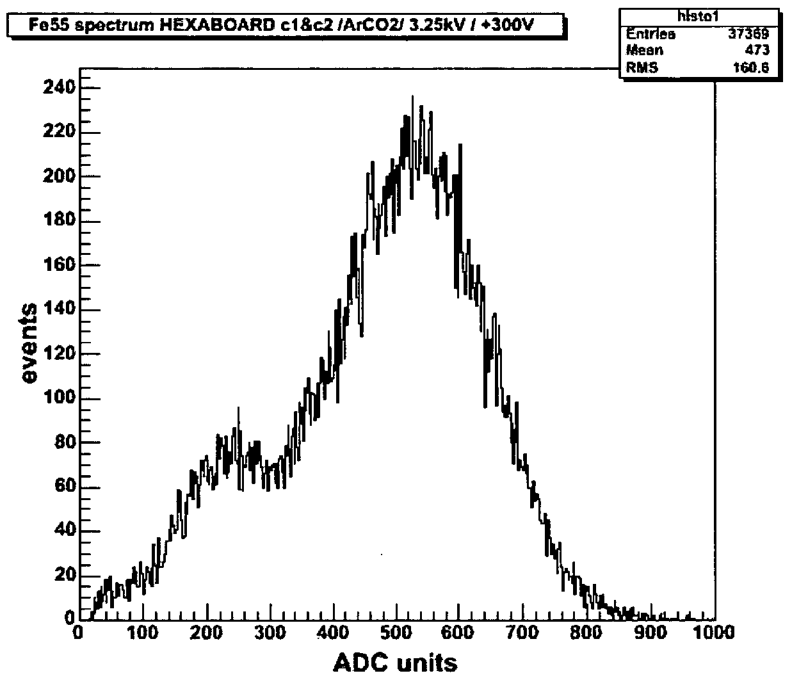

Fig. 5.24: Fe55-spectrum recorded in $ArCO_2$ (70/30) with the GEM photo-detector presented in Fig. 5.23. A voltage of 3.25kV is applied on the on the voltage divider (~360V across the GEMs). 300V over 3 mm drift gap equals a drift field of 1 kV/cm. c1&c2 denote that two cuts have been applied on the data.

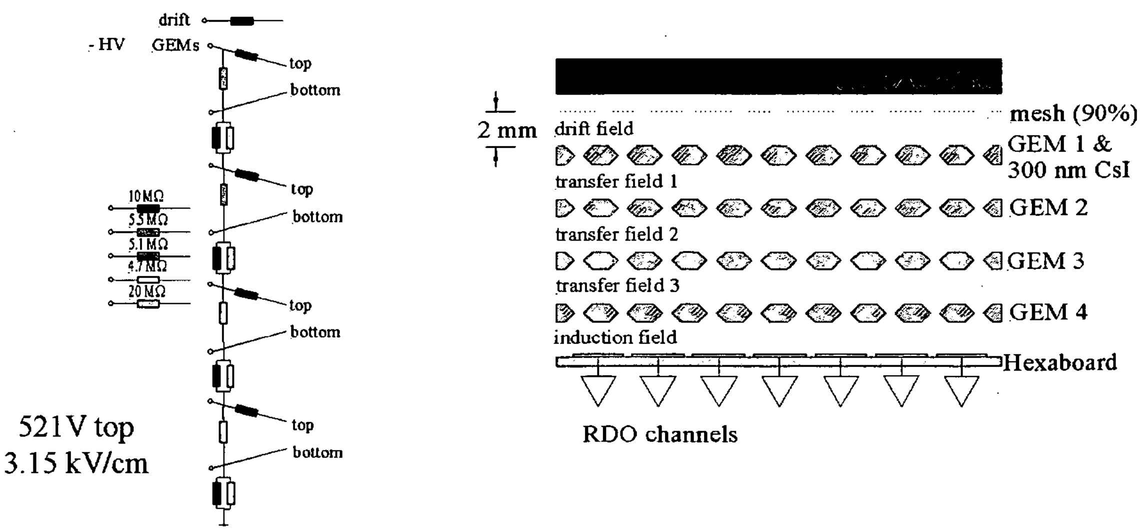

Fig. 5.25: Modified resistor chain (left) and quad-GEM photo-detector (right). Below the quartz window a fine mesh was used a drift cathode (90% optical transparency). The voltage across the top GEM was 521V and the electrical fields between the GEMs 3.15kV/cm.

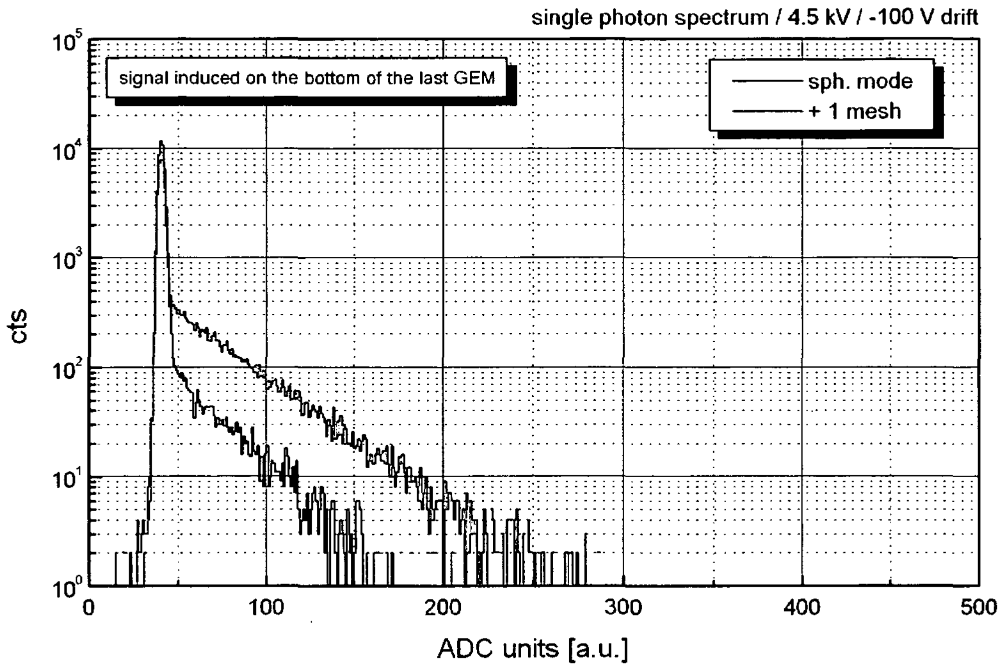

Fig. 5.26: Single photon spectrum obtained from the bottom of the last GEM in cascade of four (in the same way as shown in Fig. 3.12); the average voltage across the GEMs was 493V and the inverted drift field was 0.5kV/cm.

5.5 Reconstruction of Single Photon Multi-Hit Events

For the photon multi-hit studies a UV-transparent quartz window was used and the counter gas in the following measurements was always CH_4. The slope of the exponential single photon pulse height spectrum *(Fig. 5.26)* did not change, when the photon intensity was reduced, which proved that the detector operated in the single photon mode. The spectrum was obtained from the signal induced from the electron avalanche on the bottom of the last GEM.

Single electron clusters were recorded on the three projections. The next step in the reconstruction process was to compute the center of gravity of each recorded cluster and to check whether the in this way obtained three COG-values fulfilled the plane equation. Since the accuracy of evaluated coordinates were influenced by noise and the cluster size of its charge distribution it is unlikely that the *Equ. 5.2* was fulfilled exactly.

The COG-values u_i, v_i, w_i (i= 1..N) were obtained in the Hexagonal coordinate system. To get the position in the Cartesian coordinates a coordinate transformation had to be performed.

$$\vec{x}_1 = \begin{pmatrix} x \\ y \end{pmatrix}_1 = \hat{M}_{vw} \begin{pmatrix} v \\ w \end{pmatrix} \qquad \text{with } \hat{M}_{vw} = \begin{pmatrix} \cos 0^\circ & \cos 120^\circ \\ \sin 0^\circ & \sin 120^\circ \end{pmatrix} = \begin{pmatrix} 1 & -\frac{1}{2} \\ 0 & \frac{\sqrt{3}}{2} \end{pmatrix} \quad \textbf{(Equ. 5.3)}$$

$$\vec{x}_2 = \begin{pmatrix} x \\ y \end{pmatrix}_2 = \hat{M}_{wu} \begin{pmatrix} w \\ u \end{pmatrix} \qquad \text{with } \hat{M}_{wu} = \begin{pmatrix} \cos 120^\circ & \cos 240^\circ \\ \sin 120^\circ & \sin 240^\circ \end{pmatrix} = \begin{pmatrix} -\frac{1}{2} & -\frac{1}{2} \\ \frac{\sqrt{3}}{2} & -\frac{\sqrt{3}}{2} \end{pmatrix} \quad \textbf{(Equ. 5.4)}$$

$$\vec{x}_3 = \begin{pmatrix} x \\ y \end{pmatrix}_3 = \hat{M}_{uv} \begin{pmatrix} u \\ v \end{pmatrix} \qquad \text{with } \hat{M}_{uv} = \begin{pmatrix} \cos 240^\circ & \cos 0^\circ \\ \sin 240^\circ & \sin 0^\circ \end{pmatrix} = \begin{pmatrix} -\frac{1}{2} & 1 \\ -\frac{\sqrt{3}}{2} & 0 \end{pmatrix} \quad \textbf{(Equ. 5.5)}$$

Due to the obvious symmetry three transformations are possible *(Equ. 5.3 to Equ. 5.5)*. In the ideal case that the plane equation is fulfilled exactly the three coordinates $\vec{x}_1 = \vec{x}_2 = \vec{x}_3$ are the same. As already mentioned, the three points could be slightly different. The three computed points had to be interpolated.

$$\begin{pmatrix} x \\ y \end{pmatrix} = \frac{1}{3}\left(\vec{x}_1 + \vec{x}_2 + \vec{x}_3\right) \quad \textbf{(Equ. 5.6)}$$

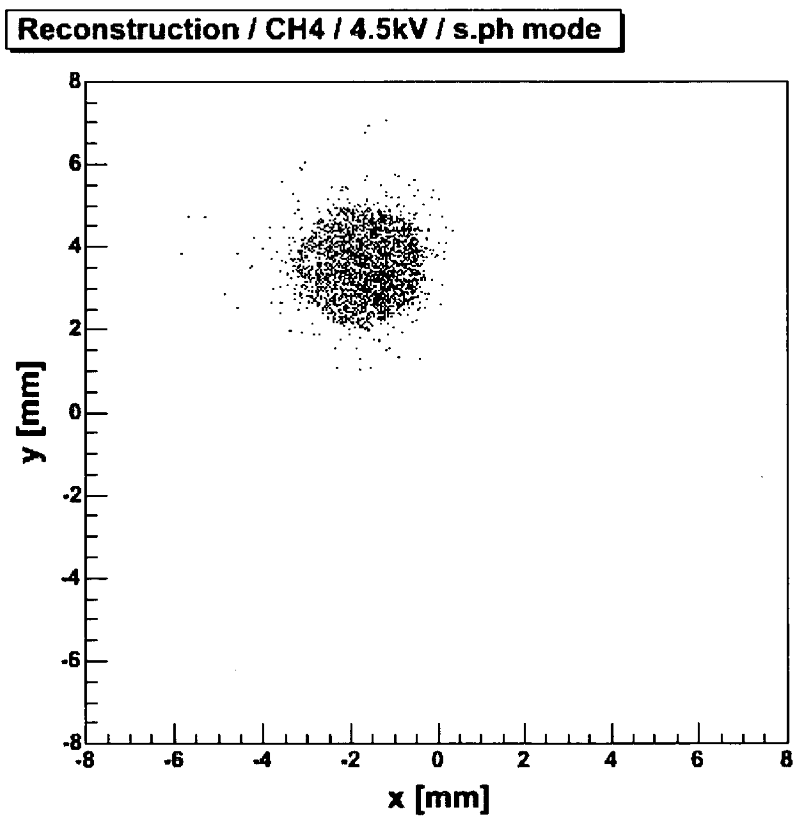

Fig. 5.27: Reconstructed image for UV photons of a circular mask on the top of the quartz window.

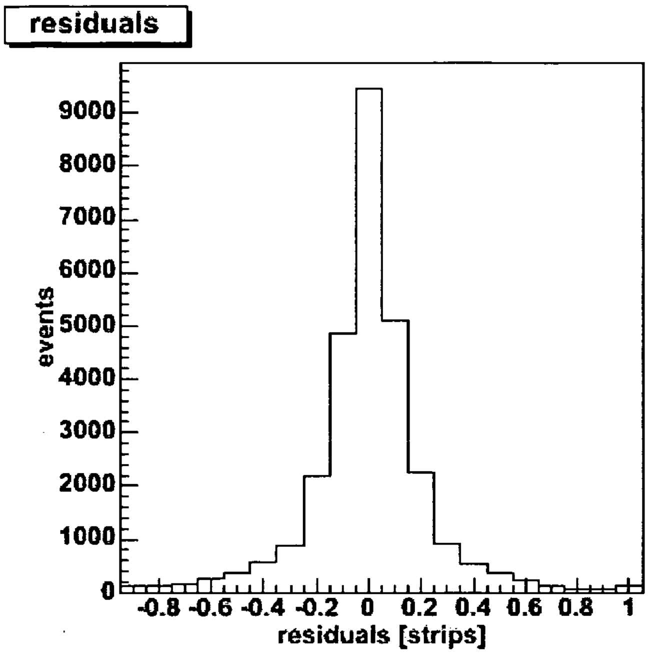

Fig. 5.28: Residual distribution. If the plane equation is fulfilled perfectly the residual equals 0. The FWHM of this distribution is 0.3.

This average value *(Equ. 5.6)* was then interpreted as the detection position (x/y) of the photon. This position in then counted in the corresponding image matrix. *Fig. 5.27* illustrates the image of a circular mask on the top of the quartz window obtained in the way described above.

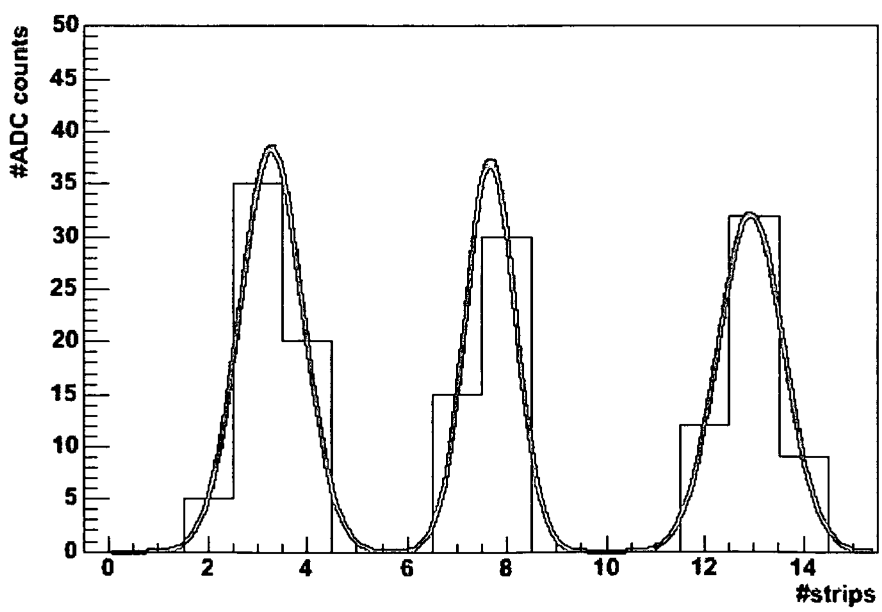

Fig. 5.29: Example of multi-photon event in one projection.

In order to determine the cluster width of the recorded single photon events, a program was written, which fitted the recognized clusters with a Gaussian function. In this way the mean value of this fit, which should equal the computed COG-value, and the cluster width were obtained. In this simple cluster recognition separated clusters were identified and fitted, even single strip hits.

The resolution properties of the photo-detector for multi-hit resolution were studied by using masks with several holes. A reconstructed single photon event is presented in *Fig. 5.30.* A clean double photon hit can be found in *Fig. 5.31.* In both cases the reconstruction is free from ambiguities.

In the case that clusters overlap in one projection *(Fig. 5.32)* the strong correlation between the charges recorded on the three projections adds up to the resolution power of the novel readout device.

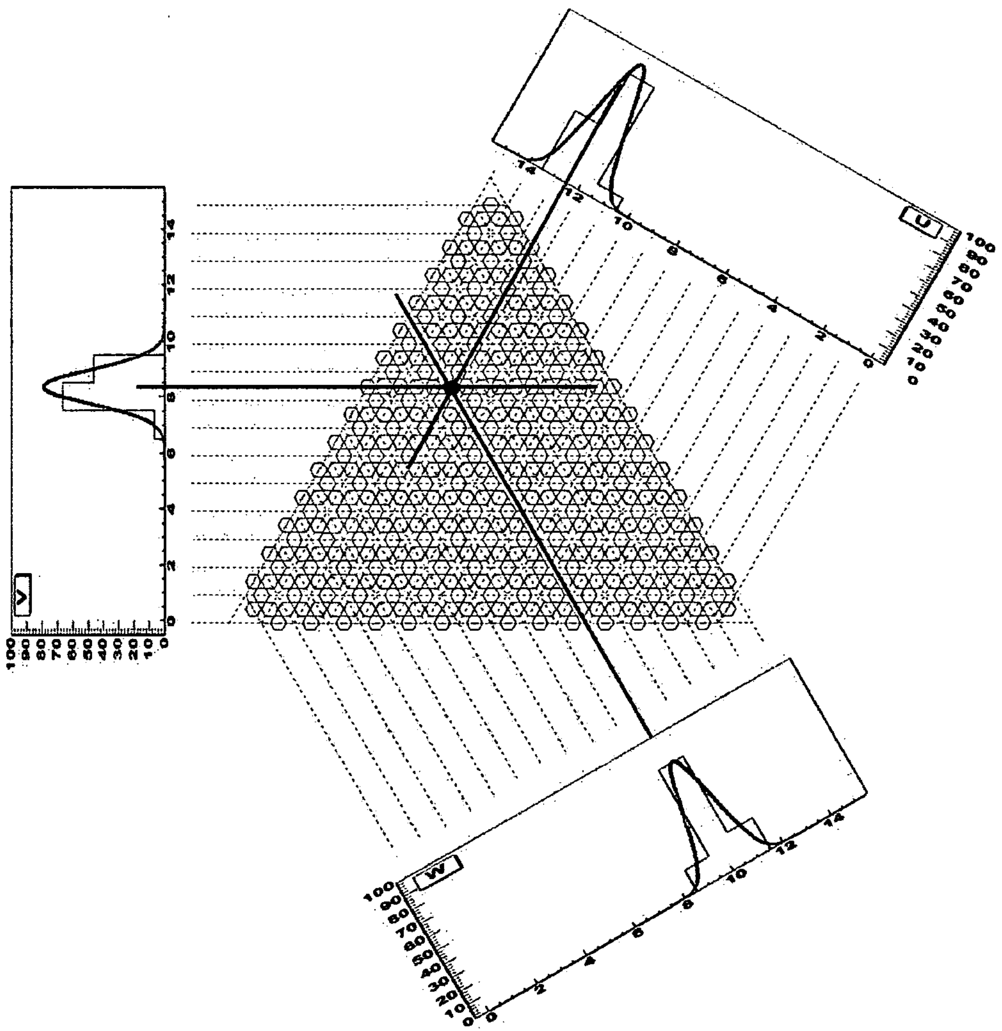

Fig. 5.30: Reconstruction of a single photon event. The respective plots show the charge distributions as a function of the strip number. By fitting the distributions with a Gaussian the COG and the cluster size are obtained.

Fig. 5.33 presents a plot of the cluster charge correlation between two projections (u,v) for all (single and double) photon events. The recorded charge per event and per projection were summed-up and a two dimensional histogram was filled. *Fig. 5.34* shows the charge correlation between two projections (u,v) where only double photon events have been taken into account. The mask was placed, that the two photon hits have to overlay in on arbitrary projection. According to *Fig. 5.32* in these measurements this was the u projection. In the other projections always two clusters could be recognized. If there is a good charge correlation between the projections the slopes in the corresponding two-dimensional histograms had to be the same.

Fig. 5.33 & *Fig. 5.34* imply that the charge sharing fraction between two projections is close to one, which is true, as can be seen in *Fig. 5.35*. Similar relations could be found in the two other projections. According to *Fig. 5.37* the charge is typically shared between two adjacent strips.

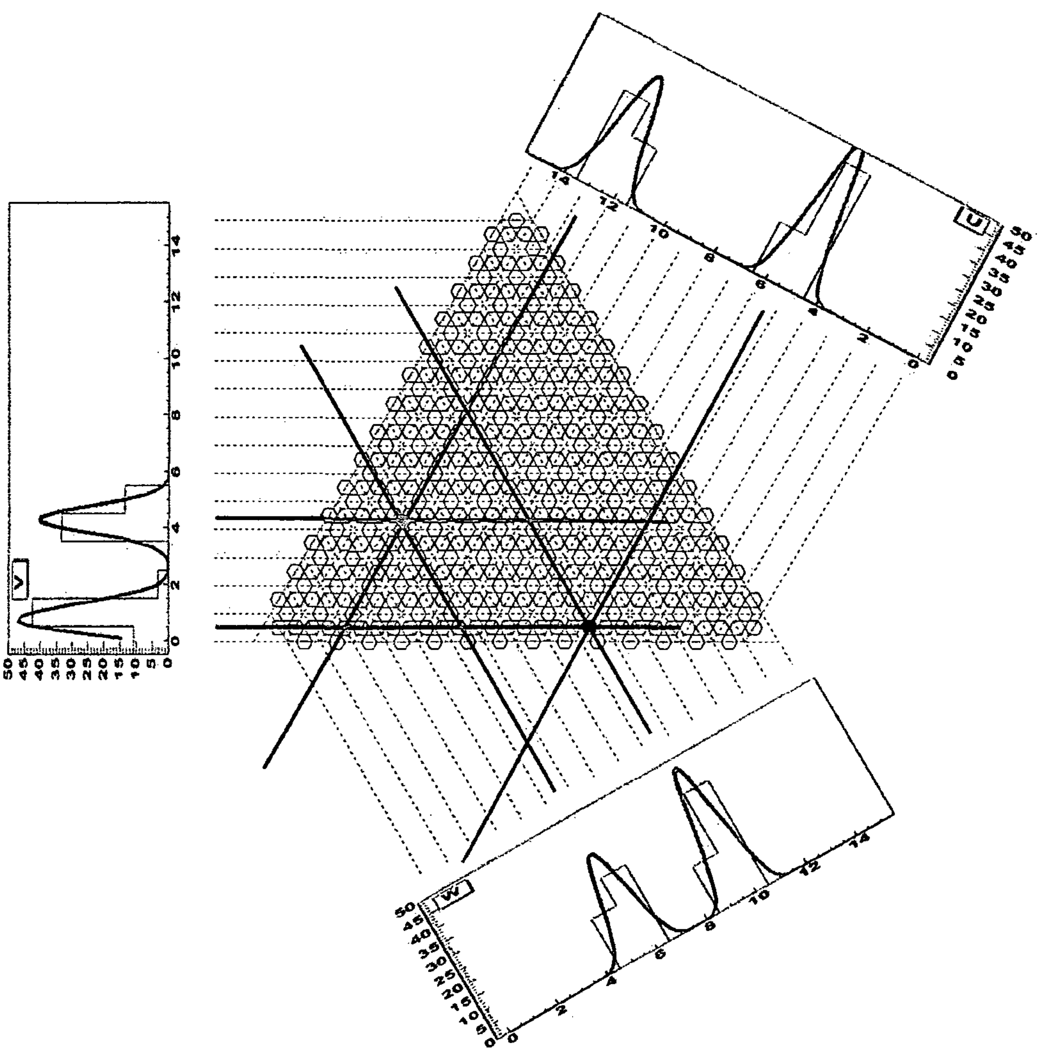

Fig. 5.31: Reconstruction of a clean double photon event.

Therefore it is possible to interpolate in the calculation of the coordinates. As can be seen in *Fig. 5.36* the cluster width has almost the same value in the three projections: ~260 μm rms. The corresponding single photon pulse height spectrum is shown in *Fig. 5.38.* This spectrum was obtained by applying a 3σ noise cut on the measured data and taking into account only single photon events. The effective gain was about 4 10^6.

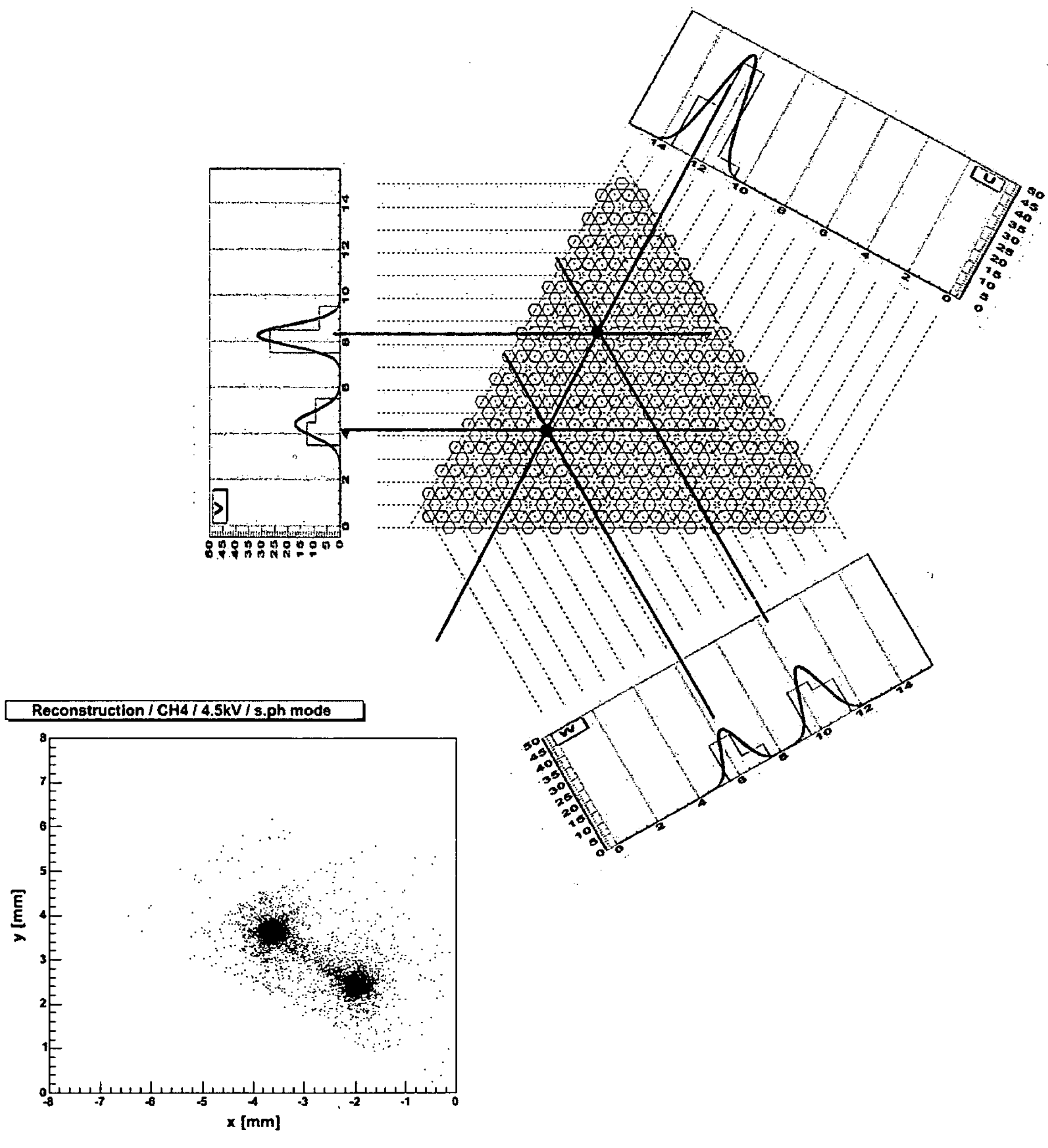

Fig. 5.32: Reconstruction of double-hit event. In one projection (u) two photons hit the same strip, which results in one cluster. On the other two projections two clusters were recognized. Due to the good charge sharing these hits are resolvable. Reconstructed hit map (image of the used mask) of the single photon events in the sensitive triangular area.

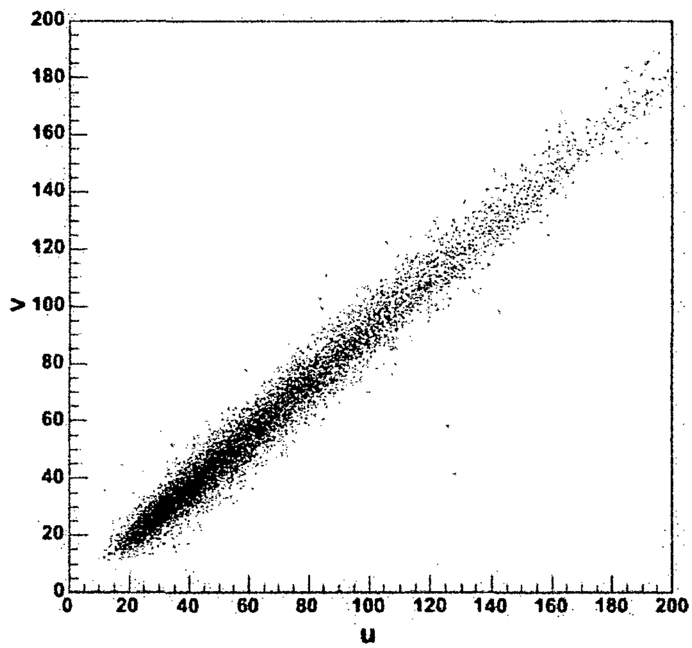

Fig. 5.33: Cluster charge correlation of the u and v projection for single and double photon events (22217 entries).

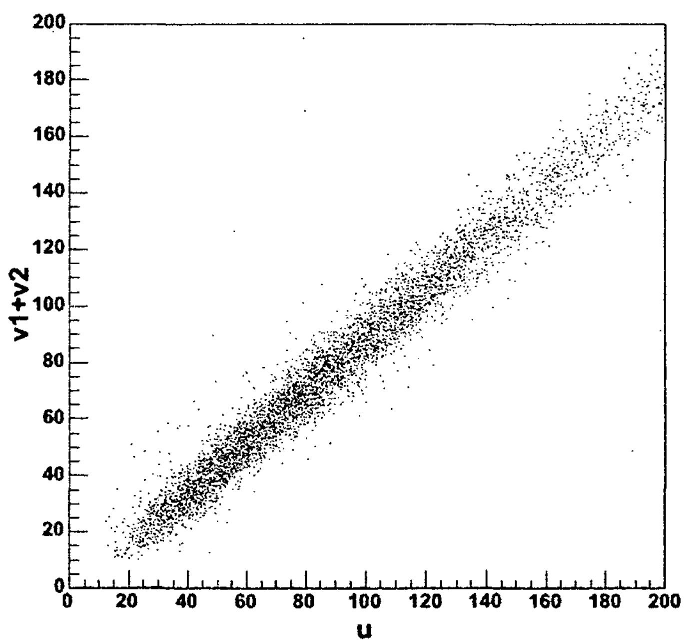

Fig. 5.34: Cluster charge correlation of u and v, when a two photon hit resulted in one charge cluster in the u projection and two clusters in the v projection (corresponding to Fig. 5.32) (5072 entries). The sum of the charge of the two clusters and the single cluster is in the same correlation as the total charge (Fig. 5.33) of the same projections for all events.

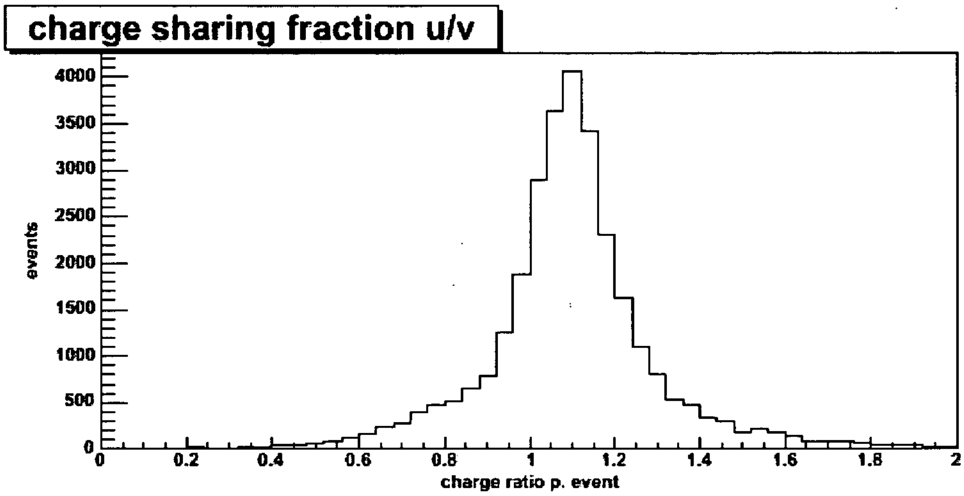

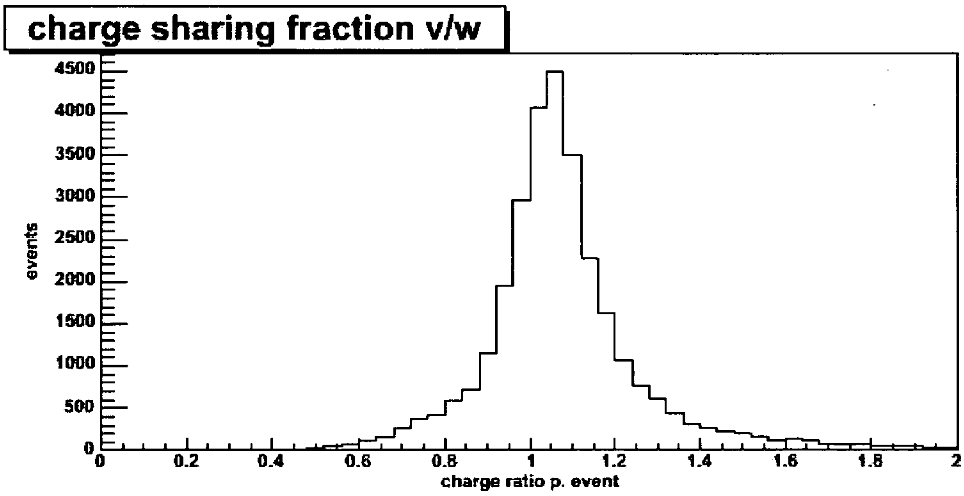

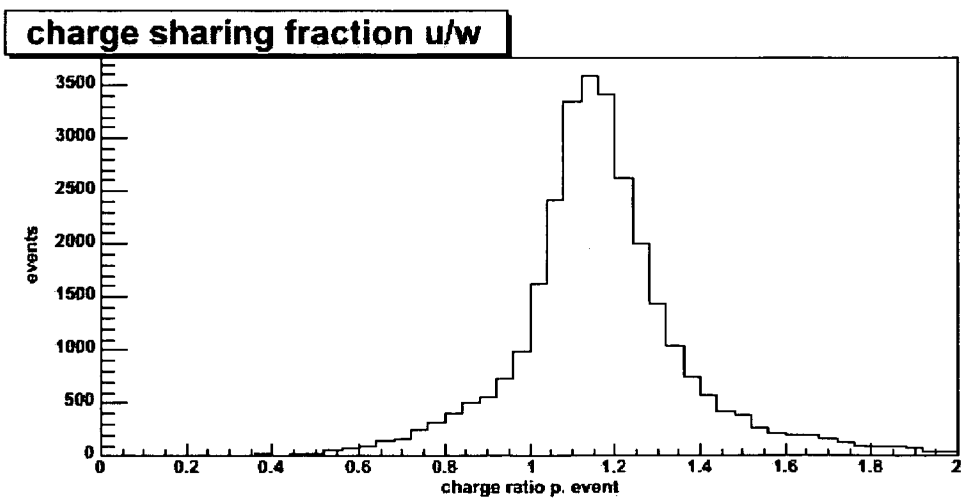

Fig. 5.35: Charge sharing fractions of respective two of the three projections. The ratios are about one.

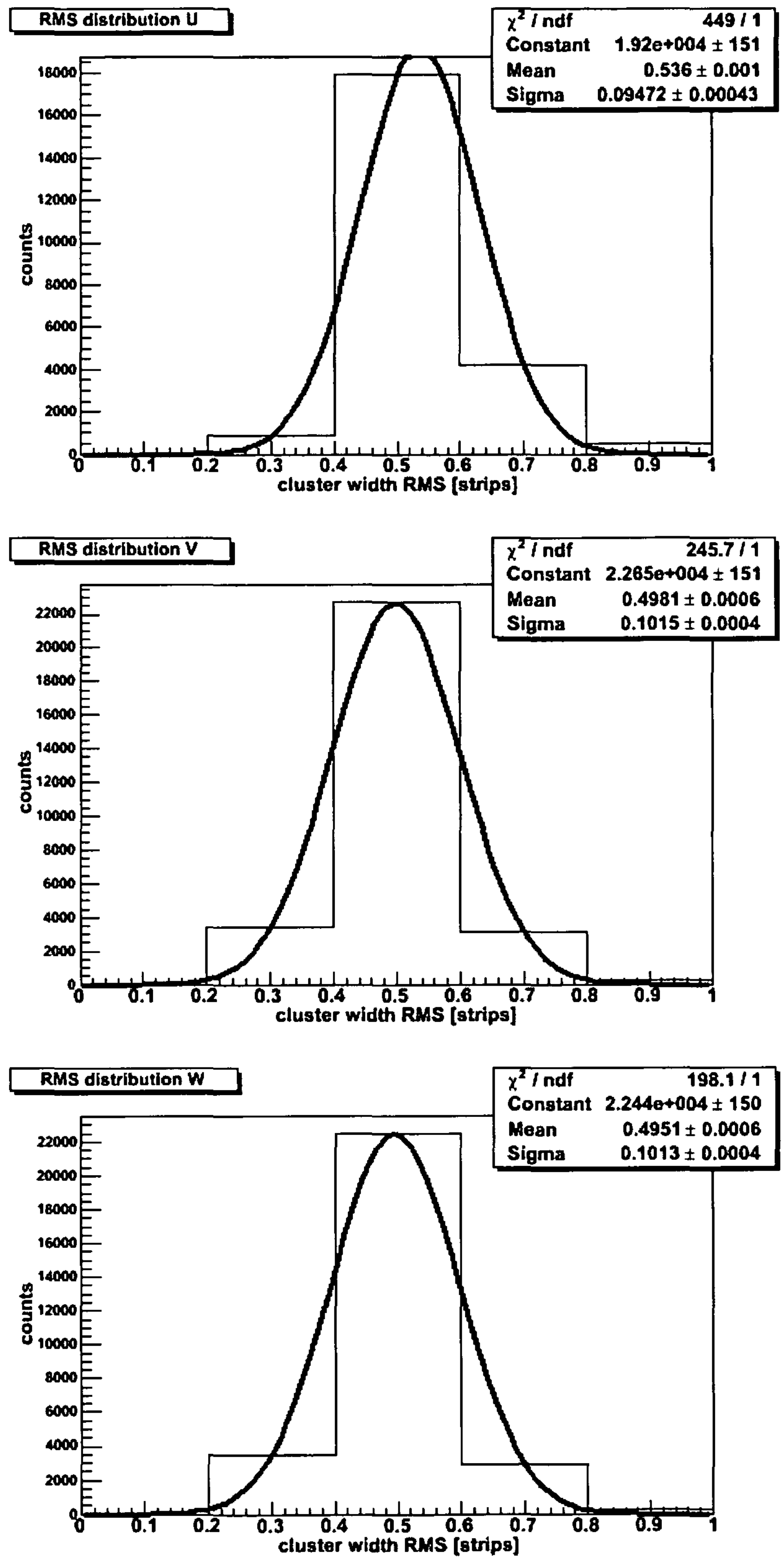

Fig. 5.36: RMS distributions of the cluster width for three projections (1 strip=0.5mm).

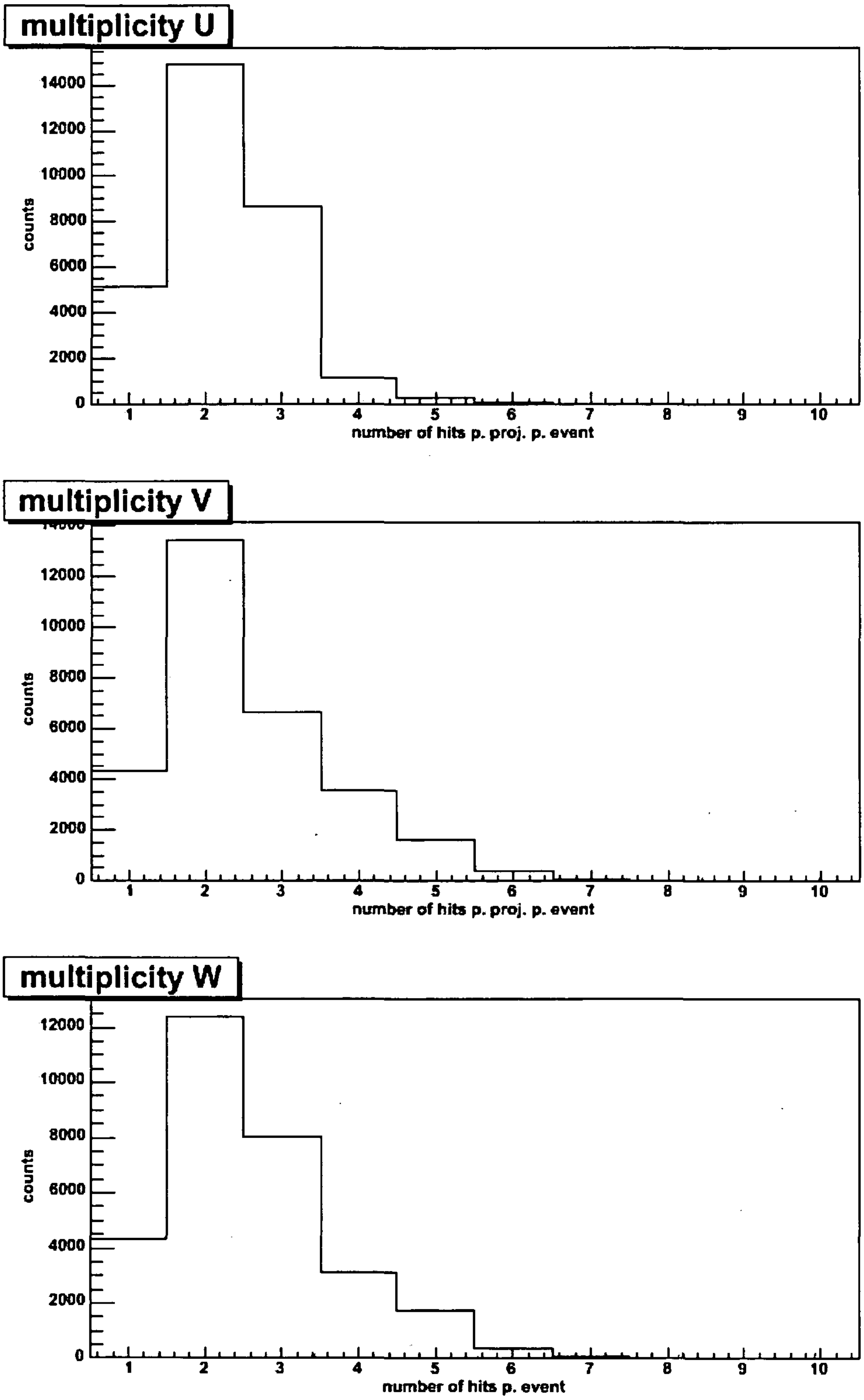

Fig. 5.37: Multiplicities of the three projections. This plot shows the distribution of then number of channels per event that recorded a signal. The cluster charge was typically shared between to strips.

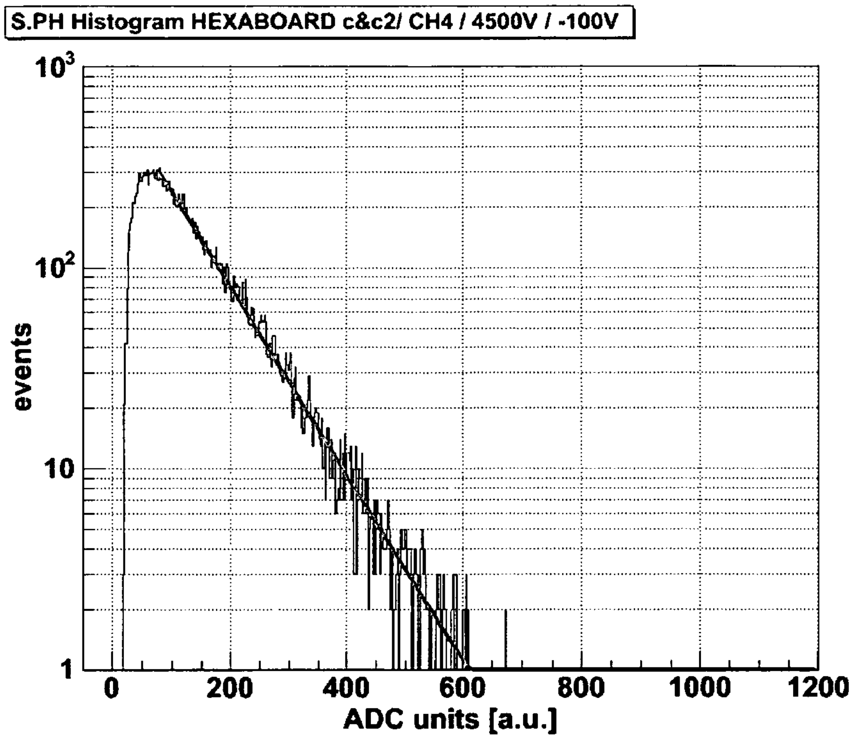

Fig. 5.38: Single photon pulse height spectrum, recorded with the ALTRO FEE (3σ noise cut, only single photon events).

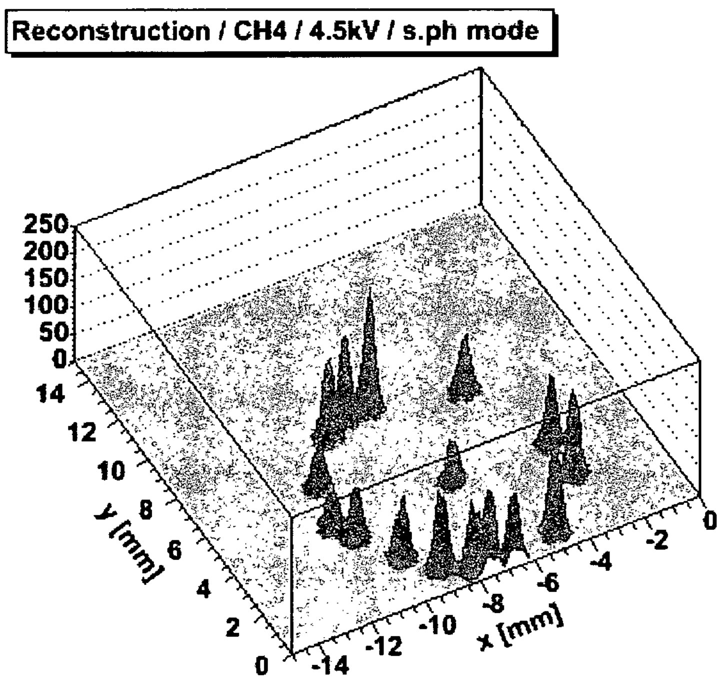

Fig. 5.39: Image of a ring mask to simulate a Cherenkov ring.

A reconstructed image of a Cherenkov-ring like mask, placed on the top of the quartz window above the increased sensitive area of the HEXABOARD (32 channels per projection) would look like *Fig. 5.39.* The single photon hit points have been simulated to show that the reconstruction programs developed for this purpose work.

Chapter 6

Conclusions and Outlook

The results presented in this work show that a new generation of RICH detectors based on the novel GEM-technology is feasible. A GEM-based photon detector allows the detection of single photons with a high efficiency and good spatial resolution (55 μm rms). Together with multi-hit capability given by the HEXABOARD an ambiguity-free reconstruction of multiple photon hits is provided. These novel readout boards are also producible in larger scales [55].

The intrinsic features of the GEM-technology lead to a suppression of the photon and ion feedback. The reduced photon feedback decreases the photon background and enhances the resolution power of RICH GEM-device.

As outlined in the last chapter, the flow of positive ions to the CsI-layer is one of the potential damaging factors that cause aging of the CsI-photocathode. Also in a GEM-based photon detector ions produced in the amplification stages can reach the CsI-layer. However, on the application of proper electrical fields the number of ions can be reduced. Therefore the damage to the layer due to ion bombardment can be minimized compared to the standard wire-based readouts, where ion avalanches triggered by photoelectrons and other ionizing particles hit the CsI-layer. In the case of a GEM-photon detector only avalanches induced by photoelectrons contribute to the current on the photocathode.

Due to the hygroscopicity of the photosensitive layer any amount of water in the detector has to be avoided. The main component of a GEM-foil is Kapton. In order to understand the influence of the out-gassing Kapton on the quantum efficiency of RICH GEM-detectors more R&D in this field is necessary.

Taking into account the general advantages of the GEM-technology a GEM-photon detector is well suited for fast RICH applications, even if large areas have to be covered and high gas amplification factors are needed under a high rate environment.

Chapter 7

Appendix

7.1 Photoelectric Absorption in Argon

A. ^{55}Fe X-Rays

The ^{55}Fe-source emits 5.9keV X-rays.

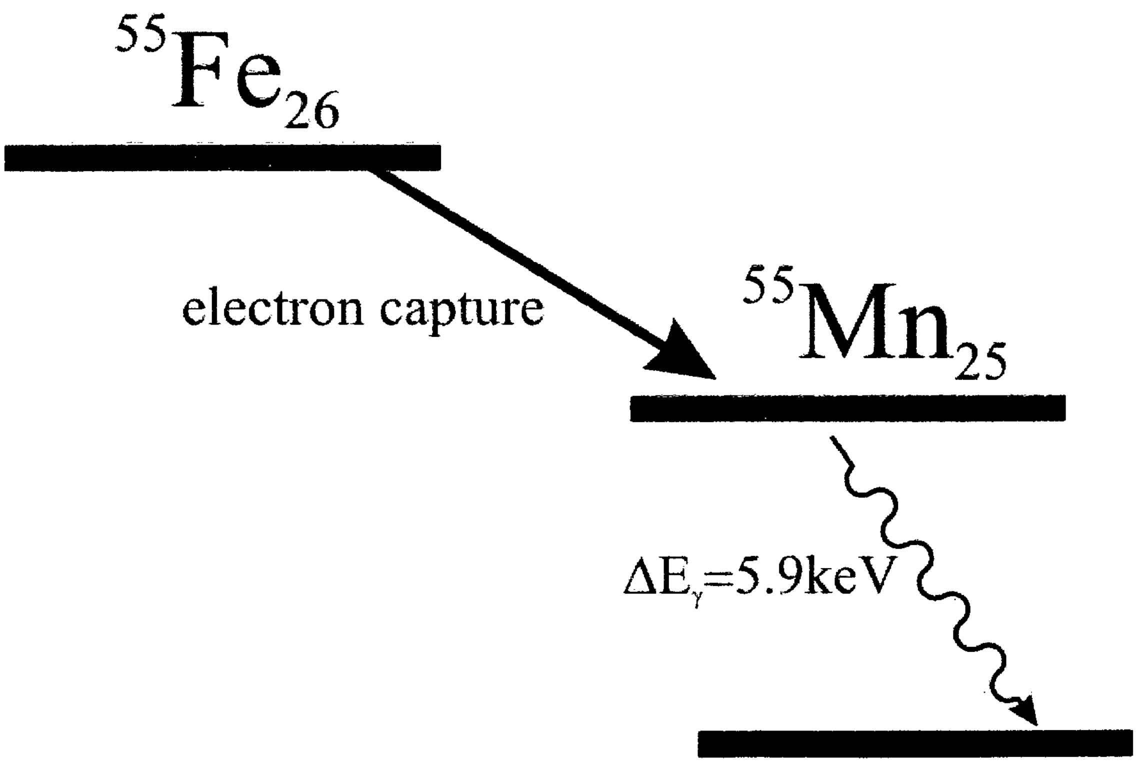

Fig. 7.1: Decay scheme of ^{55}Fe.

The main modes of the absorption process in Argon are:

- 80% K-absorption: γ(5.9keV) → electron (2.7keV) + Auger-electron (2.9keV) Photoelectron and Auger-electron are detected in the sensitive volume of the gas detector. The deposited energy ΔE = 5.9keV.

- 16% K-absorption: : $\gamma(5.9keV) \rightarrow$ electron (2.7keV) + γ_{LM} (0.3keV) + γ_{KL} (2.9keV)
  Photoelectron and the LM-fluorescence-photon are detected in the detector. The KL-fluorescence-photon has an escape length of 1cm in Ar and can escape the drift gap. Therefore, the deposited energy is $\Delta E = 3.0keV$.

- <4% L-absorption: $\gamma(5.9keV) \rightarrow$ electron (5.6keV) + γ_{LM} (0.3keV)
  Photoelectron and LM-fluorescence-photon are detected in the detector. The deposited energy is $\Delta E = 5.9keV$

The energy-spectrum shows a double-peak structure with one peak at 5.9keV and a smaller escape-peak at 3.0keV (*Argon-escape peak*).

B. X-Ray (9 keV)

The Cu X-ray-tube emits 9keV X-rays. The photoelectric absorption has the following main contributions:

- 80% K-absorption: $\gamma(9.0keV) \rightarrow$ electron (5.8keV) + Auger-electron (3.2keV)
  Photoelectron and Auger-electron are detected in the sensitive volume of the gas detector. The deposited energy $\Delta E = 9.0keV$.

- 16% K-absorption: : $\gamma(9.0keV) \rightarrow$ electron (5.8keV) + γ_{LM} (0.3keV) + γ_{KL} (2.9keV)
  Photoelectron and the LM-fluorescence-photon are detected in the detector. The KL-fluorescence-photon has an escape length of 1 cm in Ar and can escape the drift gap. Therefore, the deposited energy is $\Delta E = 6.1keV$.

- <4% L-absorption: $\gamma(9.0keV) \rightarrow$ electron (8.7keV) + γ_{LM} (0.3keV)
  Photoelectron and LM-fluorescence-photon are detected in the detector. The deposited energy is $\Delta E = 5.9keV$

The energy-spectrum shows a double-peak structure with one peak at 9.0keV and a smaller escape-peak at 3.1keV (*Argon-escape peak*).

7.2 Mapping of the FEE

real channel	ALTRO channel
1	27
2	50
3	55
4	63
5	58
6	62
7	57
8	52
9	20
10	22
11	26
12	23
13	25
14	21
15	24
16	60
17	59
18	53
19	48
20	54
21	49
22	56
23	61
24	51
25	13
26	35
27	7
28	11
29	6
30	2
31	8
32	1
33	42
34	40
35	43
36	34
37	41
38	33
39	4
40	32
41	9
42	3
43	10
44	15
45	0
46	14
47	12
48	5
P2: 49	91
50	114
51	119
52	127
53	122
54	126
55	121
56	116
57	84
58	86
59	90
60	87
61	89
62	85
63	88
64	124
65	123
66	117
67	112
68	118
69	113
70	120
71	125
72	115
73	77
74	99
75	71
76	75
77	70
78	66
79	72
80	65
81	106
82	104
83	107
84	98
85	105
86	97
87	68
88	96
89	73
90	67
91	74
92	79
93	64
94	78
95	76
96	69

Red: J1; blue: J2; green: J3, starting with P1.

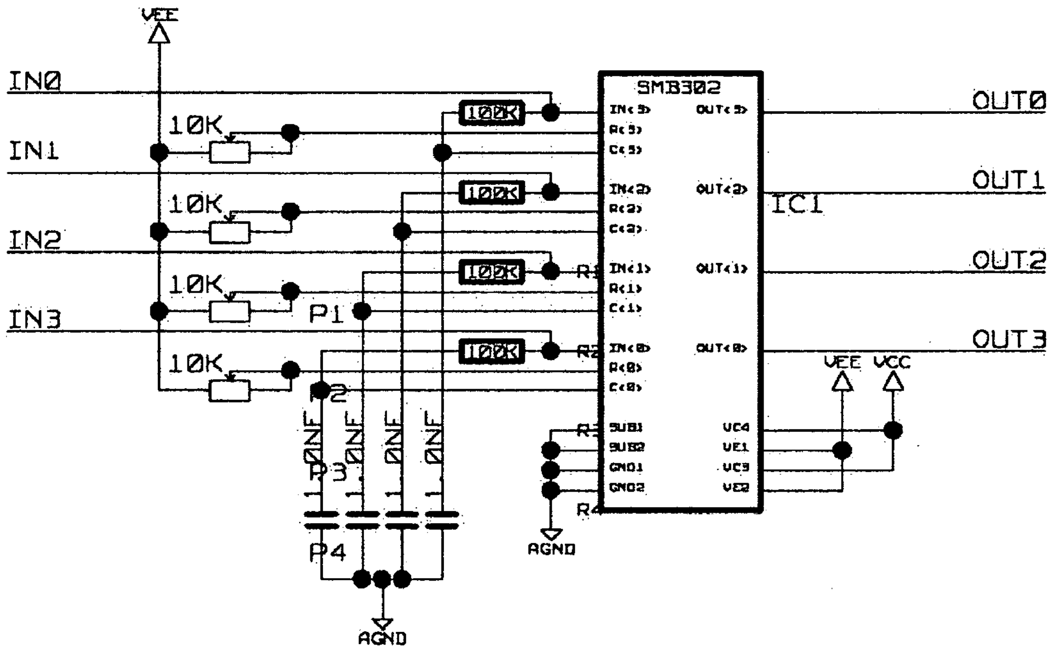

Fig. 7.2: Electrical scheme of the Legrand-chip.

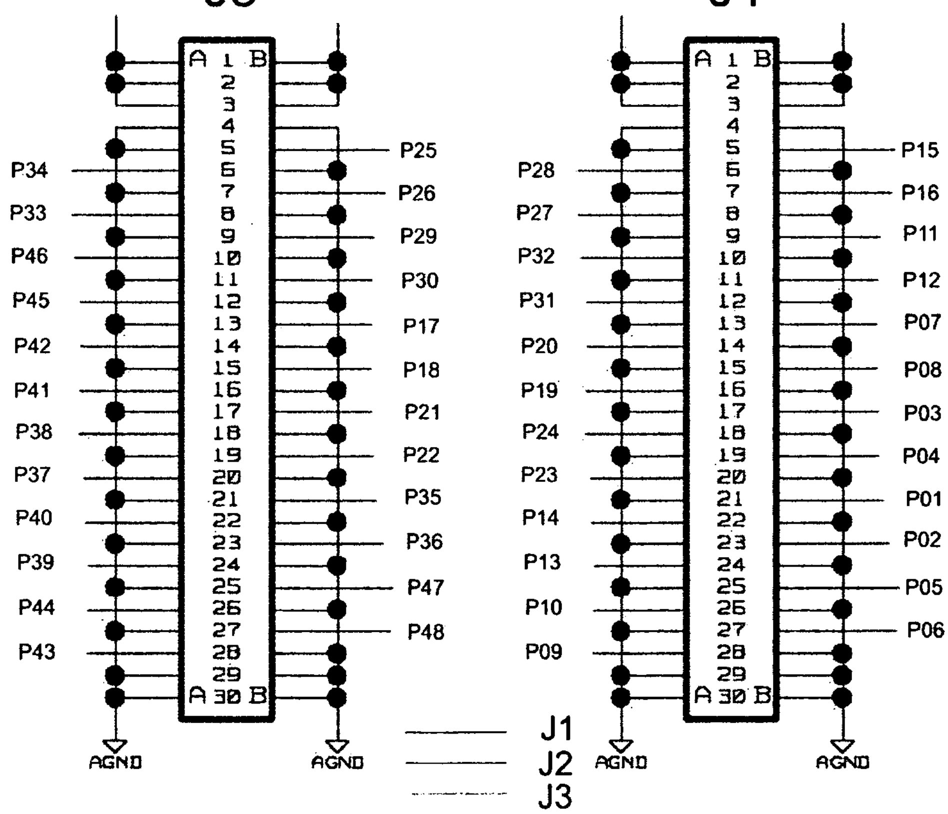

Fig. 7.3: Corresponding potentiometers on the preamplifier cards (P1 & P2) for changing the dynamic range of the respective channels (together with Table. 5.1).

7.3 Properties of used Gases and Gas Mixtures

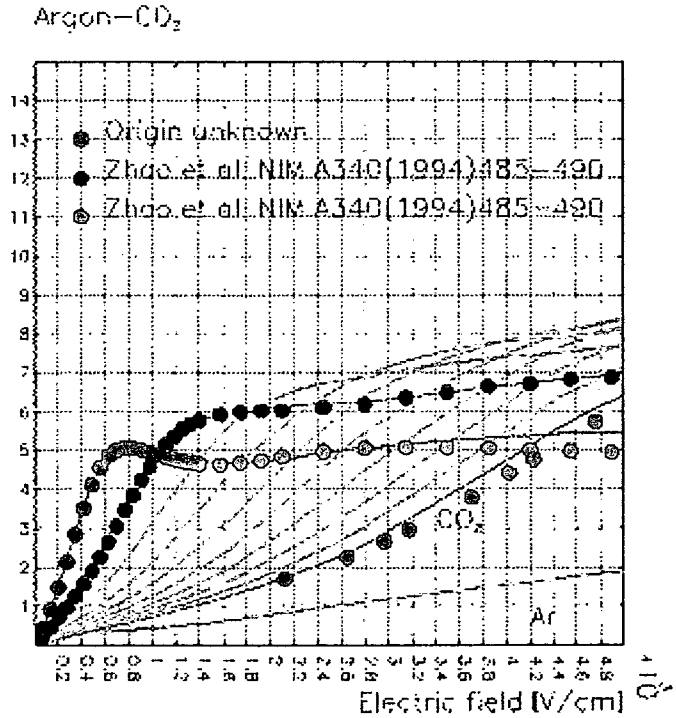

Fig. 7.4: Drift velocity of Argon-CO_2 based gas mixtures in cm/µs.

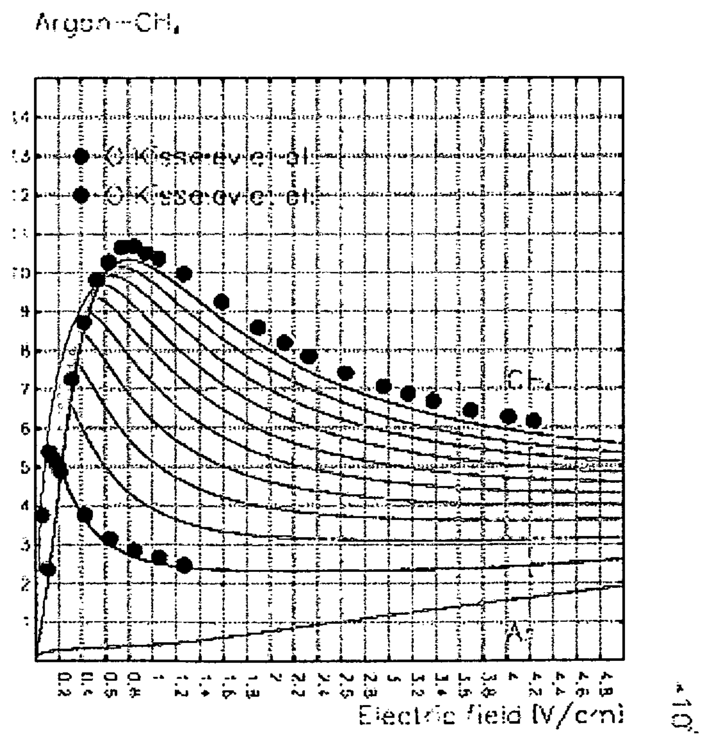

Fig. 7.5: Drift velocity of Argon-CH_4 based gas mixtures in cm/µs.

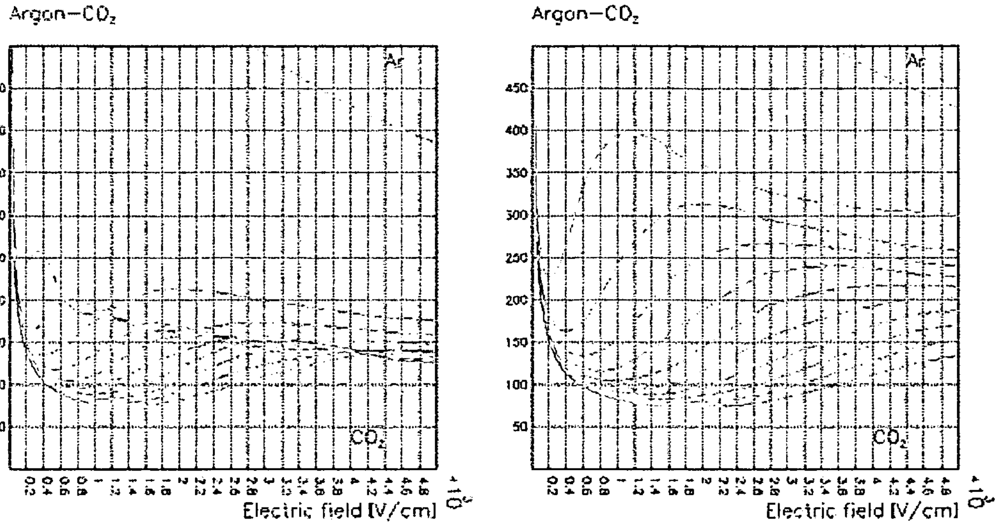

Fig. 7.6: Transversal (left) and longitudinal (right) diffusion after 1 cm of drift in μm.

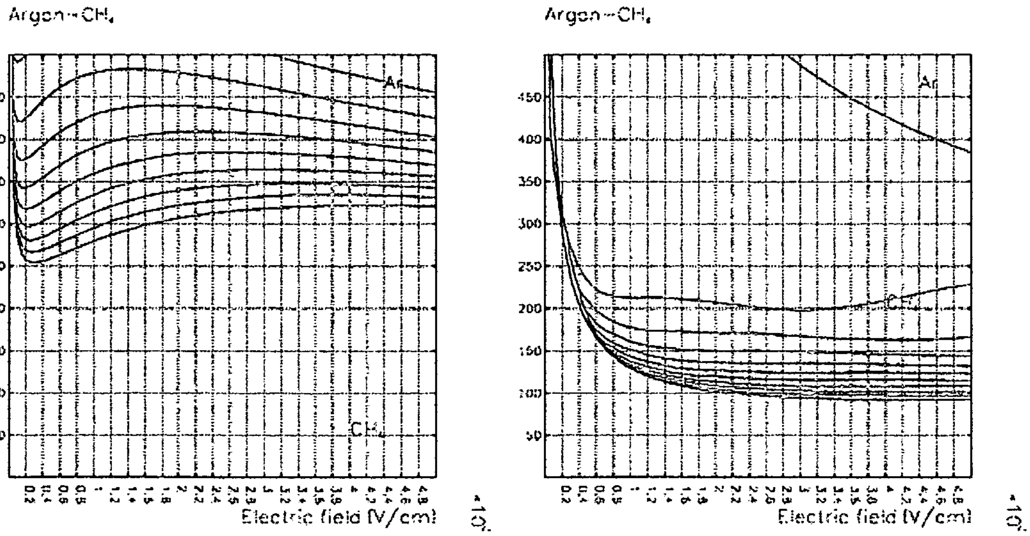

Fig. 7.7: Transversal (left) and longitudinal (right) diffusion after 1 cm of drift in μm.

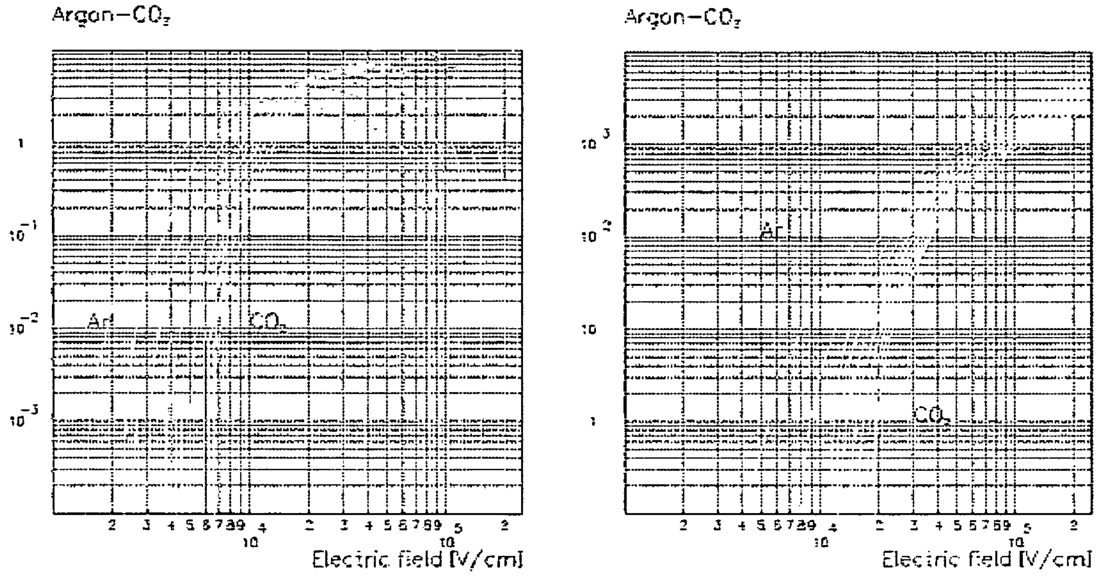

Fig. 7.8: Electron Capture and Townsend coefficients.

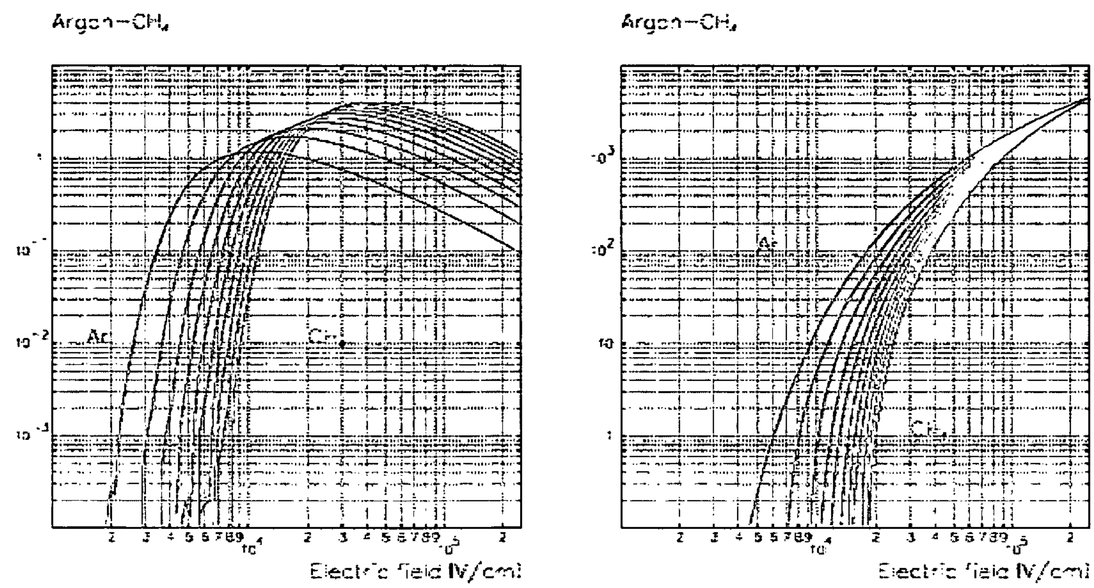

Fig. 7.9: Electron Capture and Townsend coefficients.

7.4 Bibliography

[1] P. W. Higgs: Broken Symmetries, Massless Particles and Gauge Fields Phys. Lett.12,132,133 1964

[2] D. Denegri: Standard Model physics at LHC (pp-collisions), published in [3], Vol I, 56-117 (1990)

[3] G. Jarlskog and D. Rein (editors): Proceeding of the Large Hadron Collider Workshop CERN/90-10 (1990)

[4] LEPC meeting, August 2000, CERN (2000)

[5] E. Accomando et al.., Physics Reports 299 (1998)

[6] ATLAS Collaboration, Tech. proposal for a general-purpose pp experiment at the Large Hadron Collider at CERN, CERN-LHCC-94-43, CERN, Geneva 1994

[7] ALICE Collaboration, Tech. proposal for a large ion collider experiment at CERN, CERN-LHCC-95-71, CERN, Geneva, 1995

[8] LHCb Collaboration, Tech. proposal, CERN-LHCC-98-004, CERN, Geneva, 1998

[9] CMS Collaboration, Tech. proposal, CERN-LHCC-94-38, CERN, Geneva, 1994

[10] P. Weilhammer, Overview: Silicon Vertex Detectors and Trackers, Nucl. Instr. and Meth. in Phys. Res. A453 (2000) 60.

[11] H. Dyjkstra, Overview of Silicon Detectors, Nucl. Instr. and Meth. in Phys. Res. A478 (2002) 37

[12] F. Sauli and A. Sharma, Micro-Pattern Gaseous Detectors Ann. Rev. Nucl. Part. Sci. 49 (1999) 341

[13] G. Charpak: Nucl. Instr. Meth. 62 (262) 1968

[14] A. Oed: Nucl. Instr. Meth. A263 (351) 1988

[15] A. Barr, S. Bachmann, B. Boimska, R. Bouclier, A. Braem, C. Camps, M. Capeans, V. Commichau, W. Dominik, G. Fluegge et al.: Nucl. Instr. and Meth. A403 (1998) 31

[16] R. Bouclier, M. Capeans, J. Evans, C. Garabatos, G. Manzin, G. Million, L. Ropelewski, F. Sauli, L. Shekthman, T. Temmel, G. Fischer: Nucl. Instr. Meth. 367:168 (1995)

[17] Bartol F. M. Bordessoule, G. Chaplier, M. Lemonnier, S. Megtert: J. Phys. III France 6:337 (1996)

[18] Giomataris Y., Ph. Rebourgeard, J.P. Robert, G. Charpak.: Nucl. Instr. and Meth. in Phys. Res.A376:29 (1996)

[19] Biagi SF, Jones TJ: Nucl. Instr. and Meth. in Phys. Res. A361:72 (1995)

[20] A. Sharma, A Comparison of Micro-pattern Gas Avalanche detectors Nucl. Physics B (Proc. Suppl.) 78 (1999) 540-545

[21] L. Shekhtman: Micro-pattern gaseous detectors Nucl. Instr. and Meth. in Phys. Res A 494 (2002) 128-141

[22] F. Sauli: Nucl. Instr. Meth. A386:531 (1997)

[23] C. Altunabas M. Capeans, K. Dehmelt, J. Ehlers, J. Friedrich I. Konorov, A. Gandi, S. Kappler, B. Ketzer R. de Oliveira et. al.: Construction, test and Commissioning of a triple GEM detector for COMPASS, Nucl. Instr. and Meth. A490 (2002) 177

[24] B. Ketzer et al.: Tripel GEM-Tracking Detectors for COMPASS, IEEE, Trans. Nucl. Sci., vol 49, pp. 2403-2410, 2002

[25] S. Bachmann: Performance of GEM detectors in high intensity particle beams, Nucl. Instr. Methods, A470:548 (2001)

[26] A. Bressan, M. Hoch, P. Pagano, L. Ropelewski, F. Sauli, S. Biagi, A. Buzulutskov, M. Gruewe, G. De Lentdecker, D. Moermann, A. Sharma.: Nucl. Instr. and Meth. A 424 (1999) 321

[27] G. Bencivienni, G. Felici, F. Murtas, P. Valente, W. Bonivento, A. Cardini, A. Lai, D. Pinci, B. Saitta, C. Bosio: Nucl. Instr. and Meth. A488(2002) 493

[28] http://pcwetans.home.cern.ch/pcwetans/

[29] F. Sauli; Principles of Operation of Multi Wire Proportional and Drift Chambers, CERN 77-09, Geneva 1977

[30] D.E. Groom and S.R. Klein: Passage of Praticles Through MatterParticle DATA Book, Review of Particle Physics (rev. 1999)

[31] Lohse and Witzeling, Instrumentation in High Energy Physics, World Scientific 1992

[32] G. F. Knoll: Radiation Detection and Measurement, 2nd Edition, Chapter 2

[33] Compton AH. Phys Rev 21:15, 1923a

[34] Compton AH Phys Rev 22:409, 1923b

[35] Dyson NA. X-rays in Atomic and Nuclear Physics,Cambridge University Press, Second Editon 1990

[36] W. Blum, L. Rolandi .: Particle Detection with Drift Chambers, Springer Verlag (1994)

[37] A. Peisert et al.: Drift and Diffusion of Electrons in Gases: A Compilation. CERN 84-08, July 1984

[38] Grupen, Claus: Particle Detectors, Cambridge University Press 1996

[39] F. Sauli: Gas filled detectors, IEEE November 2002

[40] V. Paladino, B. Sadoulet: Application of classical theory of electrons in gases to drift proportional chambers; Nucl. Instrum. Methods 128 (323) 1975

[41] O. Allkofer, Spark Chambers, Thiemig Muenchen, 1969

[42] B. Schmidt: Drift and Diffusion of Methane and Methane-like mixtures, thesis, Universitaet Heidelberg, unpublished (1986)

[43] Th. Lohse and W. Witzeling: The Time Projection Chamber, Instrumentation in High Energy Physics Vol. 9, F. Sauli ed., Word Scientific (1991)

[44] Cern Academic Lectures on Particle Physics 2005

[45] K. Kleinknecht: Detectors for Particle Radiation, Cambridge University Press 2nd Edition 1998

[46] R. Bouclier, M. Capeans, W. Dominik, M. Hoch, J.C.Labbe, G. Million, L. Ropelewski, F. Sauli, A. Sharma: The gas electron multiplier; CERN-PPE/96-177

[47] S. Bachmann et al.: Charge Amplification and Transfer Process in the Gas Electron Multiplier; CERN-EP/99-48

[48] M. Hoch, Development of Fast Tracking Detectors: Micro Strip Gas Chamber and GEM Gas Electron Multiplier, TU Wien, Dissertation

[49] Technology invented by R. De Oliveira and A. Gandi, CERN-EST-MT

[50] G. Jesse, CERN-EST-SM

[51] F. Sauli et al.: Electron Collection and Ion Feedback in GEM-Based Detectors IEEE Trans. Nucl. Sci NS-50 (2003) 803

[52] S. Bachmann et al.: Discharge studies and prevention in the Gas Electron Multiplier; CERN-EP 2000-151

[53] Ortec Amplifiers http://ortec-online.com

[54] A. Sharma: 3D Simulation of charge transfer in a Gas Electron Multiplier and comparison to the experiment, Nucl. Instr. Meth. A 454(2000) 267

[55] MICE, An International Muon Ionization Cooling Experiment, Proposal to the Rutherford Appleton Laboratory, 2003

[56] V. Avati et. al.: The TOTEM experiment, Eur. Phys J C., pp. 255-268, 1997

[57] M. Bozzo et. al.: Design and Construction of the Triple GEM Detector for TOTEM Proc. IEEE Nuclear Science Symposium (Rome, 2004)

[58] www.caen.it

[59] J. Seguinot, G. Charpak, Y. Giomataris, V. Peskov, J. Tischhauser, T.Ypsilantis: Nucl. Instrum. Methods A297 (1990) 133

[60] G. Charpak, P. Fonte, V. Peskov, F. Sauli, D. Scigocki, D. Stuart; Nucl. Instrum. Methods A307 (1991) 63

[61] HADES, Proposal for a High Acceptance Di-Electrons Spectrometer, GSI Darmstadt, 1993

[62] ALICE Collaboration, Technical Proposal, CERN/LHCC 95-71

[63] COMPASS proposal, CERN/SPSLC/96-14

[64] ALICE, TDR HMPID 1998

[65] F. Piuz, CsI-cathode and RICH detectors, Nucl. Instrum. a Methods A 371 (1996) 96-115

[66] F. Piuz, Nucl. Instr. and Meth. A 433 (1999) 222.
A. Breskin, A. Buzulutskov, R. Chechik, D. Vartsky, G. Malamud, P. Mine: Nucl. Instrum. Meth. A 344 (1994) 537

[67] A. Di Mauro, Nucl. Instr. and Meth. A 371 (1996) 137

[68] J. Seginuot, Ecole J. Curie de Physique Nucleaire, Mabuisson, France, Sept. 1988

[69] F. Piuz, RICH systems based on gaseous photo detectors, trends and limits around particle accelerators, Nucl. Instr. and Meth. A 502 (2003) 76-90

[70] W. Adam, E. Albrecht, D. Allen, M.-L, Andrieux, G, van Appeldorn, Y. Arnoud et. al.: Nucl. Instr. and Meth. A360 (1995) 416

[71] E. Schyns, Nucl. Instr. and Meth. A 494 (2002) 441-446

[72] Y. Andres, et al., Nucl. Phys. A 698 (2002) 452c;

[73] A. Braem, et al.,Technology of Photo-cathode production, Nucl. Instr. and Methods A, 502 (2003) 205-210

[74] Breyer, 1973, #1444

[75] To be published in RICH 2004 Proceedings, A. Braem et al.: Ageing of Large CsI Photocathodes Exposed to Ionizing Radiation in a Gaseous RICH Detector (NIM A)

[76] S. Sgobba et al.; CERN-EST/SM/MB 98-07-13

[77] E. Albrecht et al.; Nucl. Instr. And Meth. In Phys. Res. A 502 (2003) 112

[78] http://www.rfid.caen.it/nuclear/syproduct.php?mod=A422#

[79] A. Bressan et. al.: Nucl. Instr. and Meth. A425 (1999) 254

[80] A. Buzulutskov et. al.: Nucl. Instr. and Meth. A433 (1999) 471

[81] S. Bachmann et. al.: Nucl. Instr. and Meth. A478 (2002) 104

[82] C. Altunabas et. al.: Nucl. Instr. and Meth. A490 (2002) 177

[83] S. Bachmann, A. Bressan, L. Ropelewski, F. Sauli A, Sharma, D. Moermann: Nucl. Instr. and Meth. A438 (1999) 376

[84] D. Moermann, A. Breskin, R. Chechik, D. Block: Nucl. Instr. and Meth. A516 (2004) 315

[85] R. Bosch et al.: IEEE Transactions Nuclear Science, Vol. 50, No 6, December 2003

[86] ALICE TDR HMPID, 1998

Curriculum vitae

Personal Data:

Name last, first:	Meinschad, Thomas Kurt
Title:	DI
Birthplace:	Wels
Birthday:	12th October 1976
Nationality:	Austrian
Marital Status:	Single
Postal Address:	CERN PH-DT2-ST, CH-1211 Geneva 23, Switzerland in Austria: 4600 Wels, Konrad Meindl Strasse 2
Telephone:	Home: ++33 (0)4/5020 1895, France ++43 (0)724266992, Austria CERN: ++41 22 /7676003 (office) ++41 76487 3492 (sunrise)

e-mail: thomas.meinschad@cern.ch

Education:

4 classes elementary school in Wels/center
4 classes lower school at a Grammar school in Wels
4 classes upper school at a Grammar school in Wels
(Grammar school with a special consideration of computer science)
A – Level in 1995 (with good success)

Military Service from Octobre 1995 to May 1996
in the Tank Batallion No. 10

Study of Technical Physics, at the Vienna University of Technology from 1996 to 2002; passed with distinction

Till summer 2005, PHD in Experimental Particle Physics at the European Organisation for Nuclear Research (CERN) in the Gas Detector Group of F. Sauli.

Relevant Knowledge:

Solving problems	
Languages:	German (native), English (fluent in spoken and written), Italian and French (basics), Latin
Programming:	Turbo Pascal, Basics, Labview, C++
Data Analysis:	Excel, Origin, ROOT
Engineering Drawing:	AutoSketch
Physics:	Vacuum physics, surface physics (TXRF, ESCA, SEM), detector physics, radiation physics, trace element analysis

List of Publications:

Construction of a windowless Si-anode X-ray tube for a more efficient excitation of low Z elements on Si-wafer surfaces in total reflection analysis;
Spectrochimica Acta Part B: Atomic Spectroscopy, Volume 58, Issue 12, 15 December 2003, Pages 2069-2077
Th. Meinschad, C. Streli, P. Wobrauschek and Ch. Eisenmenger-Sittner

GEM-based photon detector for RICH applications
Nuclear Instruments and Methods in Physics Research Section A: Accelerators, Spectrometers, Detectors and Associated Equipment, Volume 535, Issues 1-2, 11 December 2004, Pages 324-329
Thomas Meinschad, Leszek Ropelewski and Fabio Sauli

Photon Detection and Localization with GEM
Fabio Sauli, Thomas Meinschad, L. Musa, Leszek Ropelewski
Rome, IEEE 2004

Detection of primary and field-enhanced scintillation in xenon with a CsI-coated GEM detector
T. Meinschad, L. Ropelewski, F. Sauli
NIM A accepted March (2005) uncorrected proof